

MODIFICATION AND DESIGN OF A TWIN RUBY,  
Q-SWITCHED LASER FOR PLASMA PRODUCTION

By

WILLIAM GRANT ROBINSON

Bachelor of Science

Central State College

Edmond, Oklahoma

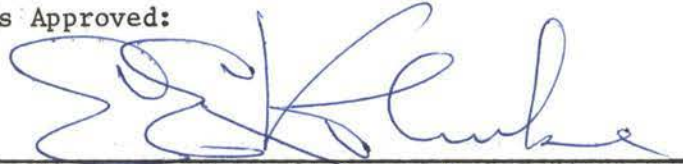
1966

Submitted to the Faculty of the Graduate College  
of the Oklahoma State University  
in partial fulfillment of the requirements  
for the Degree of  
MASTER OF SCIENCE  
July, 1970

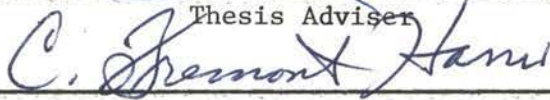
OKLAHOMA  
STATE UNIVERSITY  
LIBRARY  
OCT 28 1970

MODIFICATION AND DESIGN OF A TWIN RUBY,  
Q-SWITCHED LASER FOR PLASMA PRODUCTION

Thesis Approved:



Thesis Adviser



Dean of the Graduate College

763652

## PREFACE

The work presented in this thesis was carried out at the suggestion of this student's major advisor and project supervisor, Dr. F. C. Todd. This undertaking would have been impossible to complete without Dr. Todd's unwavering interest and expert guidance. The purpose of this work was to modify an existing twin ruby laser for Q-switched operation and then use the Q-switched, twin ruby laser for the study of transient, dense aluminum plasmas.

The author would like to thank L. J. Peery for the work he did on the original design and construction of the twin ruby laser and for our many discussions concerning the plasma experiments performed with the laser facility. Thanks go to V. D. Brown for the many discussions we had concerning the theoretical and experimental aspects of the author's work. Also the author would like to thank H. W. Willis for his help in carrying out a joint experiment using the quadrupole mass filter which he constructed. A deep appreciation is also expressed for Janet Sallee who typed the final draft.

Last but not least, the author wishes to thank his wife, Christa, for her help in preparing this manuscript and for her moral support during this period.

The work was carried out under NASA contract number NASr-7 and NA8-21391 administered through the Research Foundation, Oklahoma State University.

## TABLE OF CONTENTS

Chapter	Page
I. INTRODUCTION. . . . .	1
II. THEORETICAL DESCRIPTION . . . . .	3
General Theory . . . . .	3
Q-Switching. . . . .	15
Twin Ruby Laser. . . . .	18
Laser Beam and Surface Interaction . . . . .	23
III. MODIFICATION IN LASER DESIGN. . . . .	45
Optical. . . . .	45
Electrical . . . . .	72
Vacuum . . . . .	87
IV. LASER ENERGY AND POWER. . . . .	93
Energy Measurement . . . . .	93
Power Measurement, . . . . .	101
Laser Beam Divergence. . . . .	106
Energy and Power Densities . . . . .	113
V. TARGET DEFORMATION IN Q-SWITCHED MODE . . . . .	114
VI. PLASMA PRODUCTION . . . . .	130
Introduction . . . . .	130
Kinetic Theory Concepts. . . . .	131
Probe Measurements . . . . .	132
Strongly Negative Probe. . . . .	132
Energy Distribution and Electron Temperature . . . . .	135
Wall Potential . . . . .	137
Space or Plasma Potential. . . . .	138
The Positive Probe . . . . .	139
Laser Induced Plasma . . . . .	142
Probe Experiment . . . . .	153
Light Emission From the Plasma . . . . .	172
VII. CONCLUSION. . . . .	180
SELECTED BIBLIOGRAPHY . . . . .	185

LIST OF TABLES

Table	Page
I. Photon Gain for Rods A and B With Non-Active Q-Switch. . .	30
II. Photon Output for Rods A and B With Non-Active Q-Switch. . .	30
III. Photon Gain for Rods A and B With Active Q-Switch. . . . .	31
IV. Photon Output for Rods A and B With Active Q-Switch. . . . .	31
V. Reported Ion Energies and Velocities From Probe Measurements. . . . .	36
VI. Possible Alignment Error of the Optical Components Relative to the 6328 Å Alignment Beam. . . . .	69
VII. Possible Alignment Error of the Optical Components Due to the Difference in Index of Refraction. . . . .	69
VIII. Maximum Possible Alignment Error of the Optical Components With Respect to the Geometric Axis of the Amplifier Rod. . . . .	69
IX. Calibration Factors for Calorimeter. . . . .	97
X. Energy to Target Versus Mass Removal. . . . .	116
XI. Parameters Involved With Mass Removal. . . . .	119
XII. Experimental Values of Mass Removal Parameters for $R = .02$	123
XIII. Experimental Values of Mass Removal Parameters for $R = .03$	123
XIV. Experimental Values of Mass Removal Parameters for $R = .04$	124
XV. Experimental Values of Mass Removal Parameters for $R = .05$	124
XVI. Experimental Values of Mass Removal Parameters for $R = .06$	125
XVII. Experimental Values of Mass Removal Parameters for $R = .07$	125
XVIII. Experimental Values of Mass Removal Parameters for $R = .08$	126
XIX. Experimental Values of Mass Removal Parameters for $R = .09$	126
XX. Experimental Values of Mass Removal Parameters for $R = .10$	127

LIST OF TABLES (Continued)

Table	Page
XXI. Tabulation of Probe Data. . . . .	169
XXII. Average Maximum Velocity for Different Probes . . . . .	171

## LIST OF FIGURES

Figure	Page
1. Resonant Energy Transfer . . . . .	5
2. Photon Absorption . . . . .	6
3. Radiative Transfer to Lower State . . . . .	8
4. Energy-Level Diagram for Chromium Ion in Ruby . . . . .	14
5. Schematic of Twin Ruby Laser. . . . .	20
6. Model of Twin Ruby Laser. . . . .	22
7. Pass Diagram for Rod A With Non-Active Q-Switch . . . . .	24
8. Pass Diagram for Rod B With Non-Active Q-Switch . . . . .	25
9. Photon Gain and Output for Rods A and B With Non-Active Q-Switch. . . . .	26
10. Q-Switch Mode . . . . .	27
11. Pass Diagram for Rod A With Active Q-Switch . . . . .	28
12. Pass Diagram for Rod B With Active Q-Switch . . . . .	29
13. Photon Gain and Photon Output for Rods A and B With Active Q-Switch. . . . .	33
14. Particle Emission 0-5 nsec After Laser Beam Impact. . . . .	38
15. Particle Emission 5-10 nsec After Laser Beam Impact . . . . .	39
16. Particle Emission 10-50 nsec After Laser Beam Impact. . . . .	41
17. Particle Emission 50-100 nsec After Laser Beam Impact . . . . .	42
18. Particle Emission 100-400 nsec After Laser Beam Impact. . . . .	44
19. Schematic of Twin Ruby Laser. . . . .	47
20. Photograph of Laser Cavities. . . . .	48
21. Peery's Ruby Mount. . . . .	49

LIST OF FIGURES (Continued)

Figure	Page
22. Modified Ruby Mount. . . . .	50
23. Q-Cell Mount . . . . .	52
24. External Reflector . . . . .	53
25. Horizontal and Vertical Adjustment of Generator. . . . .	55
26. Schematic of Peery's Alignment Optics. . . . .	56
27. Alignment Optics . . . . .	57
28. Alignment Beam Splitter. . . . .	59
29. Optical Paths Alignment Beam and Ruby Laser Beam . . . . .	64
30. Angular Relationships of Brewster's Angle. . . . .	65
31. Approximate Horizontal Displacement of Ruby Laser Beam Relative to Alignment Beam . . . . .	67
32. Transmission Curve for Cryptocyanine in Methyl Alcohol . . . . .	71
33. Schematic of Laser Electrical System . . . . .	73
34. Flashtube Mounted in Pumping Cavity. . . . .	74
35. Delrin Insulation on Modified Pumping Cavity . . . . .	75
36. Schematic of Original Trigger Circuit. . . . .	77
37. Modified Trigger Circuit . . . . .	78
38. High Voltage Trigger Waveform. . . . .	79
39. Original Charging Circuit. . . . .	80
40. Charging Curve With Constant Charging Resistor . . . . .	82
41. Modified Charging Circuit. . . . .	83
42. Charging Curve With Variable Charging Resistor . . . . .	85
43. Capacitor Bank Bleeder Circuit . . . . .	86
44. Original Discharge Inductor. . . . .	88
45. Modified Discharge Inductor. . . . .	89



LIST OF FIGURES (Continued)

Figure	Page
46. Metal Vacuum Chamber. . . . .	90
47. Glass Vacuum Chamber. . . . .	92
48. Calorimeter Head. . . . .	95
49. Calorimeter Circuit. . . . .	96
50. Energy in Rat's Nest Versus Galvanometer Deflection . . . . .	98
51. Capacitor Voltage Squared Versus $\alpha$ . . . . .	99
52. Energy Levels in Optical Train. . . . .	100
53. Laser Output Versus Galvanometer Deflection . . . . .	102
54. Energy to Target Versus Galvanometer Deflection . . . . .	103
55. Photomultiplier Circuit . . . . .	104
56. Experimental Waveform Measurement . . . . .	105
57. Transmission Curve for 6943 Å Filter. . . . .	107
58. Typical Q-Switched Pulse Shape From Twin Ruby Laser . . . . .	108
59. Measurements for Beam Divergence. . . . .	109
60. Beam Divergence Apparatus . . . . .	111
61. Laser Beam Spot Size. . . . .	112
62. Mass Removal Versus Energy to Target. . . . .	117
63. Energy of Vaporization Versus Mass Vaporized. . . . .	120
64. Percent of Incident Energy Required to Cause Target Vaporization. . . . .	121
65. Heat of Vaporization Versus Incident Energy . . . . .	128
66. Photographs of Target Deformation . . . . .	129
67. Schematic of Gaseous Discharge Apparatus. . . . .	133
68. Characteristic Plots for $\log I_p$ Relative to $V_p$ After Druyvesteyn . . . . .	141
69. Intensity Versus Time of Arrival of $Al^{+3}$ Ions, After Willis	144

LIST OF FIGURES (Continued)

Figure		Page
70.	Plasma Separation. . . . .	146
71.	Photograph of Laser Induced Plasma Plume . . . . .	152
72.	Experimental Plasma Probe. . . . .	155
73.	Experimental Probe Array . . . . .	156
74.	Schematic Diagram of Probe Experiment. . . . .	157
75.	Probe No. 2, $V_p = 0.0$ VDC. . . . .	158
76.	Probe No. 2, $V_p = +5.0$ VDC . . . . .	158
77.	Probe No. 2, $V_p = +10.0$ VDC. . . . .	159
78.	Probe No. 2, $V_p = -5.0$ VDC . . . . .	159
79.	Probe No. 2, $V_p = -10.0$ VDC. . . . .	160
80.	Probe No. 3, $V_p = +5.0$ VDC . . . . .	160
81.	Probe No. 3, $V_p = +10.0$ VDC. . . . .	161
82.	Probe No. 3, $V_p = -5.0$ VDC . . . . .	161
83.	Probe No. 3, $V_p = -10.0$ VDC. . . . .	162
84.	Probe No. 1, $V_p = +5.0$ VDC . . . . .	162
85.	Probe No. 1, $V_p = -10.0$ VDC. . . . .	163
86.	Probe No. 1, $V_p = -5.0$ VDC . . . . .	163
87.	Probe No. 1, $V_p = -10.0$ VDC. . . . .	164
88.	Probe No. 4, $V_p = +5.0$ VDC . . . . .	164
89.	Probe No. 4, $V_p = +10.0$ VDC. . . . .	165
90.	Probe No. 4, $V_p = -5.0$ VDC . . . . .	165
91.	Probe No. 4, $V_p = -10.0$ VDC. . . . .	166
92.	Velocity Vectors for Second Peak . . . . .	173
93.	Velocity Vectors for Third Peak. . . . .	174
94.	Experimental Arrangement for Light Emission Measurement. . . . .	176

LIST OF FIGURES (Continued)

Figure	Page
95. Light Intensity in U.V. Versus Plasma Formation Time. . . . .	177
96. Vacuum Ultraviolet Spectrograph Experiment. . . . .	178
97. Oscillator Amplifier Laser System . . . . .	183

## CHAPTER I

### INTRODUCTION

One of the most interesting and least understood areas of plasma physics is the study of transient, dense plasmas. One method of producing a transient, dense plasma for laboratory study is by impacting a focused, Q-switched laser pulse onto the surface of a suitable target which is located in a vacuum. The following thesis describes the experimental work undertaken by the author to modify an existing twin ruby laser so as to produce a laser capable of reliable operation in the Q-switched mode and to measure certain parameters of the transient, dense plasmas produced by impacting the Q-switched laser pulse on to an aluminum target located in a vacuum chamber.

The first part of the thesis describes modifications made on the existing laser facility. The main areas of modification are in optical component mounting, flashtube triggering, optical alignment and Q-switching. The modified twin ruby laser is capable of producing 15 joules of energy in a 30 nsec pulse giving an average power of 500 megawatts. The techniques used to measure the various properties of the Q-switched laser output are described.

The last part of the thesis deals with the experiments performed on the laser induced plasma. These experiments were designed to furnish data which might be used to better understand the phenomena of transient, dense plasmas. The first data collection deals with target deformation

and mass removal as a result of laser beam impact. An experiment is then described in which electrical probes are used to measure various parameters of the laser induced aluminum plasma. Ultraviolet light from the plasma is studied and a quadrupole mass filter is used to determine the presence of various ion species in the plasma. The author then describes an experiment designed to obtain a vacuum ultraviolet spectra of the laser induced aluminum plasma.

## CHAPTER II

### THEORETICAL DESCRIPTION

The terms maser, optical maser and laser have been used interchangeably to describe the quantum electronic devices which generate coherent electromagnetic radiation in the microwave and optical regions. In the following work, the name laser will be used to describe the devices which operate in the visible region of the electromagnetic spectrum. Laser oscillation is characterized by a narrowing of the spectral and angular distribution of the spectral and angular distribution of the spontaneous emission radiation at a particular level of excitation, called the threshold. Although the phenomena of stimulated emission was advanced by Einstein as early as 1917, the first successful application was made in 1954 by Gordon, Zeiger, and Townes (1) who used the inversion transition of ammonia to obtain continuous maser oscillation at 24 Gigahertz. The first to observe spectral narrowing and a reduction in lifetime due to an inverted population in the optical region was Maiman (2) in 1960. Maiman excited a ruby rod having plane parallel ends coated with silver with intense pulses of light from a flashlamp.

#### General Theory

In considering the theory of the laser action, one of the first problems is to understand something of the nature of stimulated emission. Consider the interaction between an electromagnetic wave and a

collection of atoms. For this discussion there is no need to specify the kind of atoms in detail. The atoms may exist in a variety of energy states and, for convenience, they are contained in an enclosure. To further simplify the analysis, imagine that the atoms may exist only in a lower energy state  $E_1$  or a higher energy state  $E_2$ . Transitions between  $E_1$  and  $E_2$  may be caused by an incident electromagnetic wave whose frequency,  $\nu_0$ , is given by

$$h\nu_0 = E_2 - E_1 \quad (1)$$

where  $h$  is Planck's constant. This resonance condition is shown in Figure 1. Because of the Uncertainty Principle, the energy levels cannot be perfectly monochromatic. Only a very narrow band of frequencies satisfy the resonance condition.

If the system is in thermal equilibrium, the number of atoms in each energy state will be constant. The transition from the lower to the upper energy state can occur only by the absorption of a photon of energy from the radiation field. At resonance the number of atoms per second excited to the upper state is proportional to the number  $N_1$ , present in the lower state, to the radiation density  $\rho$  and to the probability  $B_{12}$  of an absorption per second. For the absorption process

$$N_A = N_1 B_{12} \rho \quad (2)$$

where  $N_A$  stands for the number of atoms absorbing per second. This process is shown in Figure 2. The absorption of a photon from the electromagnetic wave causes an upward transition from level  $E_1$ , to level  $E_2$  and increases the population of level  $E_2$  above its thermal equilibrium value. Atoms in level  $E_2$  are said to be in an excited state.

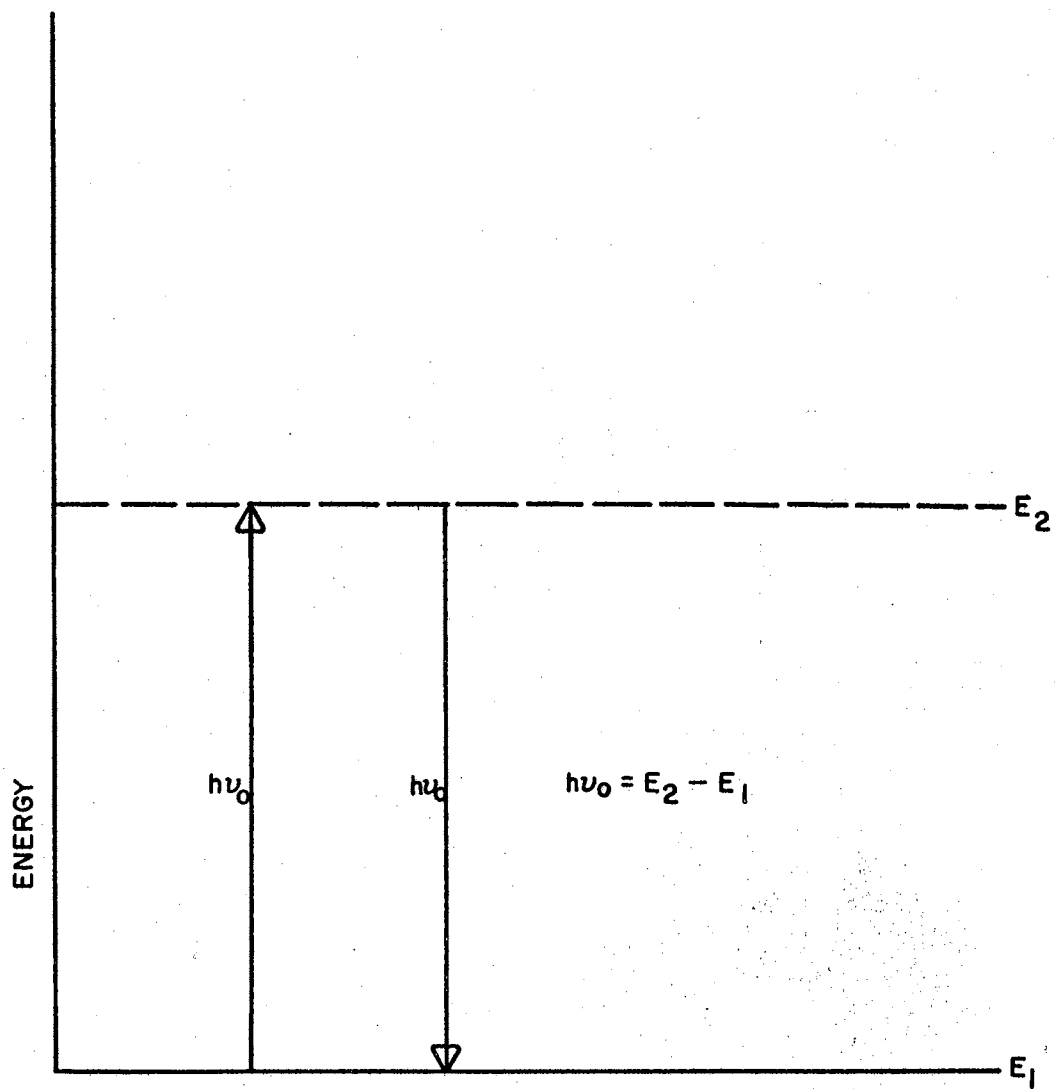


FIG. 1 RESONANT ENERGY TRANSFER



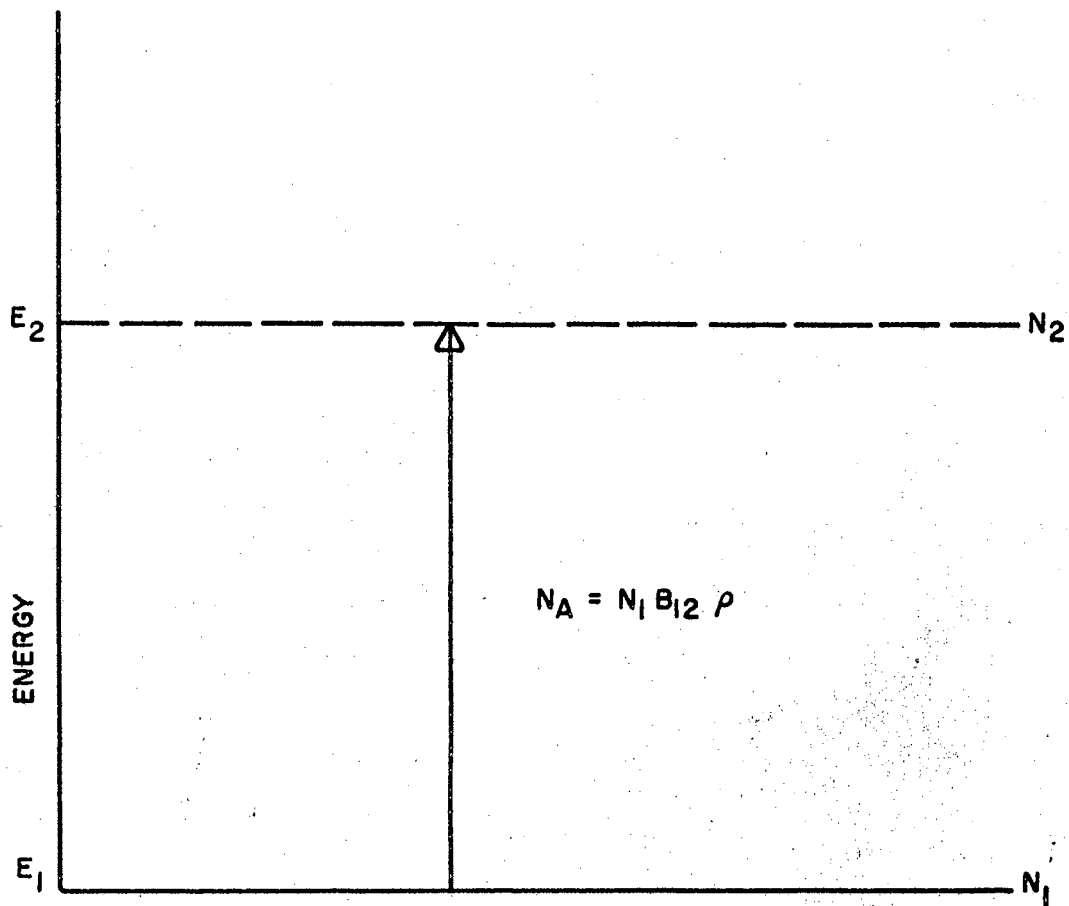


FIG. 2 PHOTON ABSORPTION

Atoms which are already in the upper energy state may make a radiative transition to the lower state by either one of the two processes that are shown in Figure 3.

One manner in which an atom in the upper or excited state may emit a photon and fall to the lower state is by spontaneous emission. In this process there is no phase relationship between the electron motion and the wave, therefore, the emission is incoherent. The probability that an atom in the upper state will emit spontaneously does not depend on the strength of the incident wave; therefore, the number of atoms,  $N_{\text{spont}}$ , undergoing a spontaneous emission per second is given by

$$N_{\text{spont}} = N_2 A \quad (3)$$

where  $A$  is the transition probability for spontaneous emission.

The other process by which an atom in the upper state can make a transition to the lower state is by stimulated emission. When an electromagnetic wave interacts with an atom in the upperstate, the motion of the bound electrons are influenced. If the phase of the incident wave is such as to oppose the electron motion, the atom will lose energy by emitting a photon. In a group of excited atoms, all those atoms which experience this phase relation will be affected in the same way, and so all of them will emit photons at the same time. When the frequency of the incident wave corresponds to the frequency of the transition from  $E_2$  to  $E_1$ , which is given in Equation (1), the photons produced by stimulated emission have the same frequency as the incident wave. In this case, amplification of the incident radiation occurs.

The number of atoms producing stimulated emission per second,  $N_{\text{stim}}$ , is given by

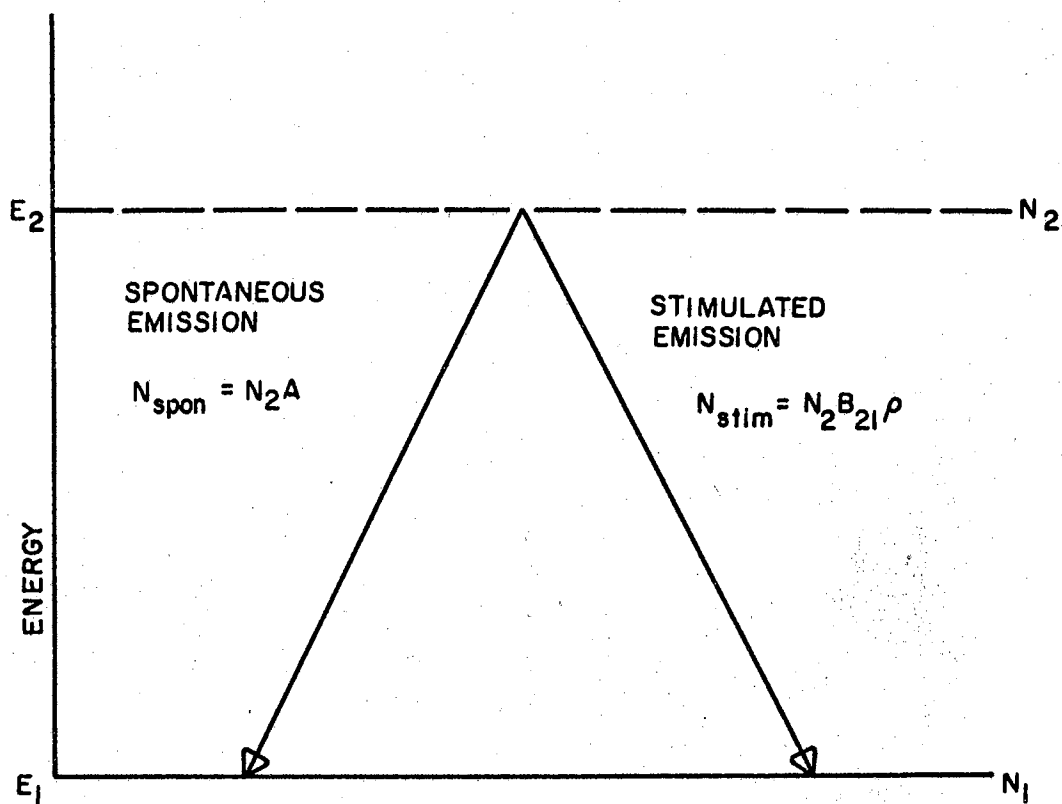


FIG. 3 RADIATIVE TRANSFER TO LOWER STATE

$$N_{\text{stim}} = N_2 B_{21} \rho \quad (4)$$

where  $N_2$  is the number of atoms in the upper energy state,  $B_{21}$  is the probability for a stimulated transition from the upper to the lower energy state and, as before,  $\rho$ , is the radiation density.

Since it is assumed that the group of atoms are enclosed and are in thermal equilibrium, it is further assumed that the number of atoms absorbing radiation is equal to the number of atoms emitting radiation; i.e.,

$$N_A = N_{\text{stim}} + N_{\text{spont}} \quad (5)$$

Substituting Equations (2), (3) and (4) into (5) gives

$$N_1 B_{12} \rho = N_2 B_{21} \rho + N_2 A \quad (6)$$

The transition probabilities  $B_{12}$  and  $B_{21}$  for upward and downward transitions have so far been considered different. Since the phase of the incident wave determines whether emission or absorption occurs and since each phase is equally probable, the transition probabilities are equal, or

$$B_{12} = B_{21} = B \quad (7)$$

The quantities A and B are known as the Einstein coefficients. The coefficients A and B may be related to each other either by comparison with the Planck radiation laws, or, more rigorously, by quantum mechanical analysis as shown by Singer (3). The ratio B/A is important because it represents the ratio of stimulated to spontaneous emission for the atomic system. Since the coherent, stimulated emission corresponds to

amplification at the signal frequency and the incoherent spontaneous emission represents noise, the ratio  $B/A$  gives a measure of the signal to noise ratio from the system. Combining Equations (6) and (7), an expression for the radiation density may be written in the following way,

$$N_1 B \rho = N_2 B \rho + N_2 A$$

$$\rho (N_1 - N_2) B = N_2 A$$

$$\rho = \frac{N_2}{N_1 - N_2} \frac{A}{B} \quad (8)$$

$$\rho = \frac{1}{\frac{N_1}{N_2} - 1} \frac{A}{B}$$

The Planck radiation law gives for the radiant energy density,  $\rho(\nu)$ , at a frequency  $\nu$ ,

$$\rho(\nu) = \frac{8\pi h}{\lambda^3} \frac{1}{\exp(h\nu/kT) - 1} \quad (9)$$

where the wave length  $\lambda$  is  $c/\nu$  and  $k$  is Boltzmann's constant. Assuming that the atomic system is in thermal equilibrium, the distribution of atoms between the upper and the lower energy states is governed by Maxwell-Boltzmann statistics. In thermal equilibrium at a temperature  $T$

$$\frac{N_2}{N_1} = \exp\left(-\frac{h\nu}{kT}\right) \quad (10)$$

Substituting Equation (10) into (8) gives,

$$\rho = \frac{1}{\frac{1}{\exp(-\frac{h\nu}{kT})} - 1} \frac{A}{B} \quad (11)$$

$$\rho = \frac{1}{\exp(\frac{h\nu}{kT}) - 1} \frac{A}{B}$$

Equating Equations (9) and (11) results in,

$$\frac{A}{B} = \frac{8\pi h}{\lambda^3} \quad (12)$$

This shows that in the microwave region, where  $\lambda \approx 1$  cm, spontaneous emission is almost negligible compared with stimulated emission. In the optical region where  $\lambda \approx 5 \times 10^{-5}$  cm, the noise contribution due to spontaneous emission is increased by a factor of  $10^{13}$ . From these considerations, it is in the microwave region that low noise amplification is achieved. In the optical region the chief interest is in obtaining intense coherent light beams.

In the preceding discussion, it was assumed that each energy level has only one state. In general there are more than one state in an energy level; so, a degeneracy term  $g$  must be introduced into Equation (7) which becomes

$$B_{12} g_1 = B_{21} g_2 = B \quad (13)$$

where  $g$  = states/energy level. Boltzmann's Equation (10) becomes,

$$\frac{N_2}{N_1} = \frac{g_2}{g_1} \exp(-\frac{h\nu}{kT}) \quad (14)$$

The Einstein B coefficients are given as,

$$B_{21} = \frac{2\pi |\mu_{21}|^2}{3h^2 g_2} = \frac{8\pi^3 |\mu_{21}|^2}{3h^2 g_2} \quad (15)$$

$$B_{12} = \frac{2\pi |\mu_{21}|^2}{3h^2 g_1} = \frac{8\pi^3 |\mu_{21}|^2}{3h^2 g_1} \quad (16)$$

where  $|\mu_{12}|^2 = |\mu_{21}|^2$  and  $\mu$  is the total, dipole moment matrix element. When a pair of levels are not in thermodynamic equilibrium, an effective temperature,  $T_e$ , may be defined in terms of the population  $N_1$  and  $N_2$ . This effective temperature is given by the following relationship,

$$\frac{N_2 g_1}{N_1 g_2} = \exp - \left( \frac{E_2 - E_1}{kT_e} \right) \quad (17)$$

where  $(E_2 - E_1)$  is positive. Solving Equation (17) for  $T_e$  gives,

$$T_e = \frac{-(E_2 - E_1)}{k \ln \left( \frac{N_2/g_2}{N_1/g_1} \right)} \quad (18)$$

If  $\frac{N_2}{g_2} > \frac{N_1}{g_1}$ , the effective temperature  $T_e$  is negative. This concept

of negative temperature is often used in discussing lasers.

The Einstein A coefficient is given as,

$$A = \frac{64\pi^4}{3h\nu^4} |\mu_{21}|^2 \quad (19)$$

Dividing Equation (19) by (15) gives,

$$\frac{A}{B_{21}} = \frac{8\pi h}{\lambda^3} \quad (20)$$

As shown in Equation (3), the spontaneous emission is a function of  $N_2$  (the number of atoms in the u-per energy level) and  $A$  (the transition probability for spontaneous emission). The transition probability  $A$  is constant for a particular atomic system.

Equation (4) shows that there are two ways to produce more stimulated emission. The first is to increase the radiation density of the electromagnetic wave acting on the system. This can be achieved by placing the collection of atoms in an optical resonator. The second method is to increase the value of  $N_2$ . This second method creates a more fundamental difficulty because, as Equation (17) shows,  $N_2$  is always less than  $N_1$  for a system in thermal equilibrium at any finite temperature. At equilibrium, the number of photons absorbed will always be greater than the number produced by stimulated emission. As a consequence of this effect, the laser will only operate when the normal population distribution across the signal levels is altered so as to make  $N_2$  greater than  $N_1$ . This process is called population inversion.

As stated earlier, one of the first solid materials for lasers was ruby,  $\text{Cr}^{3+}$  in  $\text{Al}_2\text{O}_3$ . The energy levels for ruby are shown in Figure 4.

The orbital levels shown in Figure 4 are determined by the ion,  $\text{Cr}^{3+}$ , and the lattice  $\text{Al}_2\text{O}_3$  in the absence of any magnetic field. In the optical spectra there is a broad band,  ${}^4\text{F}_2$ , about  $17,000 \text{ cm}^{-1}$  above the ground state. There is also a pair of sharp fluorescent lines,  ${}^2\text{E}$ , which is nearly  $15,000 \text{ cm}^{-1}$  above the ground state. The  ${}^4\text{F}_2$  band and the  ${}^2\text{E}$  levels are coupled, and phonon assisted transitions may occur be-



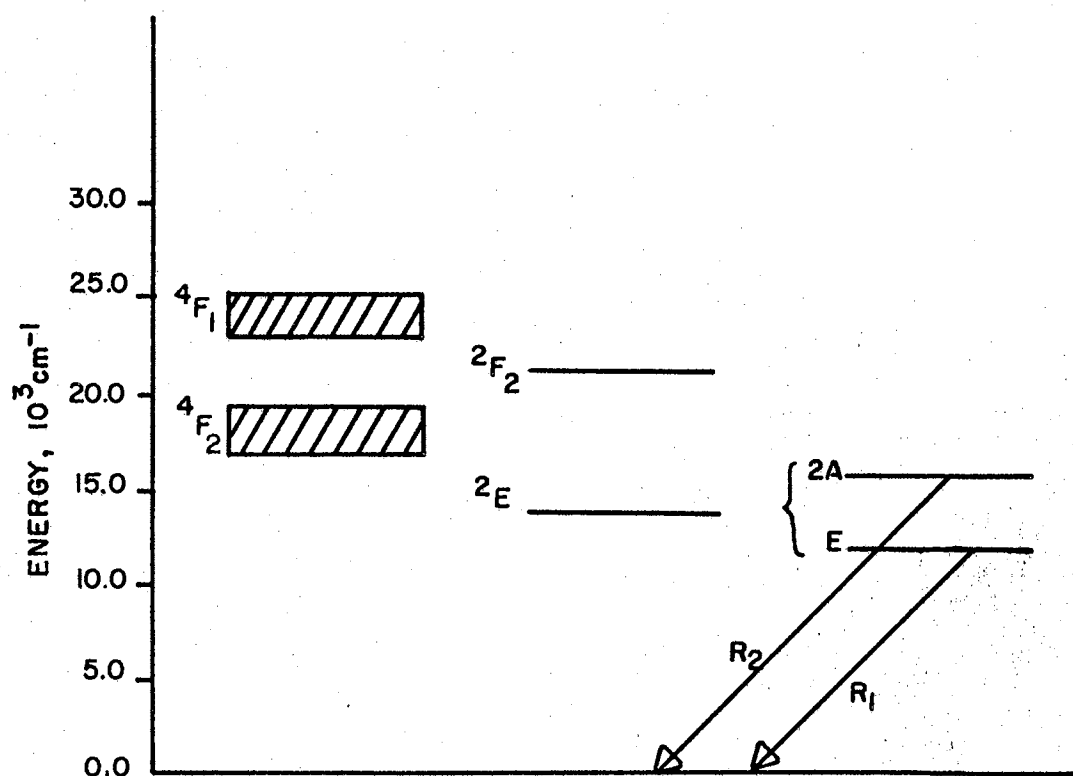


FIG. 4 ENERGY-LEVEL DIAGRAM FOR CHROMIUM ION IN RUBY

tween them so that any population change occurring in the  ${}^4F_2$  band is transferred as a corresponding change to the  ${}^2E$  levels, which have long lifetimes of about 3 msec. at room temperature. With these levels, laser operation is obtained by pumping the  ${}^4A_2 \rightarrow {}^4F_2$  transition with green light. This sets up an inverted population between the  ${}^2E$  and  ${}^4A_2$  levels, resulting in stimulated emission of radiation from the laser transitions between the  ${}^2E$  levels and the ground state. Ordinarily emission takes place from the lower fluorescent level, E, at a wavelength of  $6943 \overset{\circ}{\text{A}}$  called the  $R_1$  line. The fluorescent linewidth is about  $3\overset{\circ}{\text{A}}$ , but laser oscillation can be reduced to as little as about  $5 \times 10^{-4} \overset{\circ}{\text{A}}$  which corresponds to an extremely monochromatic, coherent light beam. The wavelength variation for ruby is given by Abella and Cummins (4) to be about

$$\lambda(T) = 6943.25 + .068 (T-20) \quad (21)$$

where T is temperature in degrees centigrade.

#### Q-Switching

The term, "Laser Q-switching," often designates methods of generating short laser pulses of high peak powers. This term is used because Q is a figure of performance for a resonator. It is defined as the ratio of the energy stored to the energy dissipated within the cavity in a time interval  $\frac{1}{2}\pi$  times the period of the optical oscillations. The latter Q is also referred to as the quality factor of the resonator.

It will be recalled that optical pumping enables ground-state laser atoms to make quantum transitions to a more energetic, longer lived metastable state. When the number of metastable atoms exceeds the num-

ber of ground-state atoms, i.e.,  $N_2 > N_1$ , the active atom population is said to be inverted and the lasing material exhibits gain. The ratio  $\Delta N/N_0$  is called the inversion or excitation level where

$$\Delta N = N_2 - N_1$$

$$N_0 = N_2 + N_1$$

In general, laser oscillation will occur when the optical gain per light transit equals or exceeds the transmission loss per transit in the resonant cavity. This defines the laser threshold condition as,

$$R \exp [L \alpha_0 (\Delta N/N_{ot})] \geq 1 \quad (22)$$

where  $R$  is the overall reflectivity,  $L$  is the cavity length, and  $\Delta N/N_{ot}$  is the threshold inversion level.

The quality factor,  $Q$ , which increases with  $R$  is given by,

$$Q = 2\pi L/\lambda(1-R) \quad (23)$$

where  $\lambda$  is the wavelength of the laser oscillations. In the absence of a Q-switch, the amplitude of the laser oscillations depends on the height at which the population inversion level can be maintained above its threshold value for a given amount of cavity loss. The height to which the inversion level may be raised depends on the speed at which active atoms are excited by optical pumping and the ability to dissipate heat before it damages the laser rod. With a Q-switch, lasing is momentarily prevented by inhibiting a laser's resonance until the laser has stored up a large amount of energy. Q-switching can convert a ten kilowatt laser in the normal mode into a gigawatt pulsed laser. Power en-

hancement is limited only by the degree of excitation of the laser medium, by the destructive threshold of the laser rod, by the optics and by the speed of the Q-switch.

The most rapid change in the Q of the cavity is achieved by inserting the Q-switch in the optical path of the cavity. Introduction of the Q-switch causes optical losses, which decreases the laser medium's Q factor, momentarily. After the laser medium is optically pumped to a high inversion level, the Q-switch is opened or becomes transparent thus restoring the normal Q of the cavity and releasing the stored energy all at once. An ideal Q-switch should, at the proper time in the pumping cycle, change instantaneously from low light transmission to perfect transparency. Because of the relative long excitation lifetime, the laser rod will store energy in the inversion level far beyond the threshold provided that the self-excitation effect of lasing is suppressed, or temporarily held off during the pumping phase. In a laser oscillator, oscillation delay and energy storage are achieved simply by removing end reflectance. The Q is thereby reduced to its zero - feedback value,  $2\pi L/\lambda$ , as in the case of an open cavity, and lasing is not possible. This is shown in Equations (22) and (23) for  $R = 0$ . There remains, however, the self-excitation effect from the laser's ability to amplify its own spontaneous emission. If the rod has an amplification path longer than about six inches, this effect can severely limit the inversion level attained by pumping.

There are, in general, two types of Q-switches - active and passive. The principal active Q-switches include the Kerr cell, the Pochel's cell and the rotating prism. The principal passive Q-switches are categorized according to their saturation mechanisms. The materials include thin

organic dye films, colored filter glasses, organic solutions and doped glass. The organic solutions and doped glass undergo reversible switching in that they are chemically and physically restored to their original state after saturation. The passive Q-switch is basically a saturatable absorption process in which the absorption of laser energy of sufficient intensity causes the absorption coefficient of the passive element to decrease and to approach a limiting value that may be nearly zero. Both active and passive Q-switching has advantages and disadvantages. The switching characteristics of a passive element changes with the degree of laser excitation. The laser's excitation level does not, however, effect the switching speed of active Q-switching systems. Switching efficiency of passive systems depends on the number of available laser photons per passive molecule per second. As a result, passive Q-switching is characteristically less efficient than active switching at low inversion levels. At high inversion levels, the performance of passive switching is competitive with, if not superior to, that of active switching. Passive Q-switching is simpler, more convenient and normally less expensive than active switching.

The Q-switch in the laser system that is described in this paper was of the passive type and will be described in detail later. A more rigorous approach to the theory of Q-switching is given by Damon (5), Mashkevich (6) and Birnbaum (7).

#### Twin Ruby Laser

The laser described in this paper is a twin ruby laser and, as the name implies, consists of two ruby rods. A theoretical discussion of the twin ruby laser will not be given here. Basically the theoretical con-

siderations are the same as for a single rod laser. The twin ruby laser is shown schematically in Figure 5. Each rod is 0.5 inches in diameter and 6 inches long. Rod A has a TIR (total internally reflecting) prism cut on one end and the other end is cut and polished at Brewster's angle. Rod B is finished with an optical flat on one end and Brewster's angle on the other end. All of the surfaces are polished to  $\lambda/10$ . The sides of both rods have a matte finish. The rods were grown and finished by the Linde Division of Union Carbide. The chromium dopant level is 0.05 percent by weight. The two rubies are arranged in the laser so that the optical axis are parallel and optically aligned. The Q-switch shown in Figure 5 was discussed in the previous section and will be discussed again in the next chapter. Without the Q-cell in place between the rubies, the twin ruby laser has the same operating characteristics as the single ruby laser. With the Q-cell in place, the twin ruby laser operates like a generator - amplifier. This is especially true when the Q-switch is active. The amplification in the different sections of the twin ruby laser is discussed below.

It is to be shown that rod A may be considered as the generator and rod B as the amplifier. The proof will be satisfied provided a photon that starts in rod A has a larger gain than a photon that starts in rod B when the photons both travel an equal distance in the stimulated media. It is also necessary to show that the part of the laser output which is contributed by the photon starting in rod A is greater than or equal to the contribution by a photon starting in rod B.

The basic assumptions that are to be made in the following proof are as follows:

1. Each time a photon has a collision with a stimulated atom, two

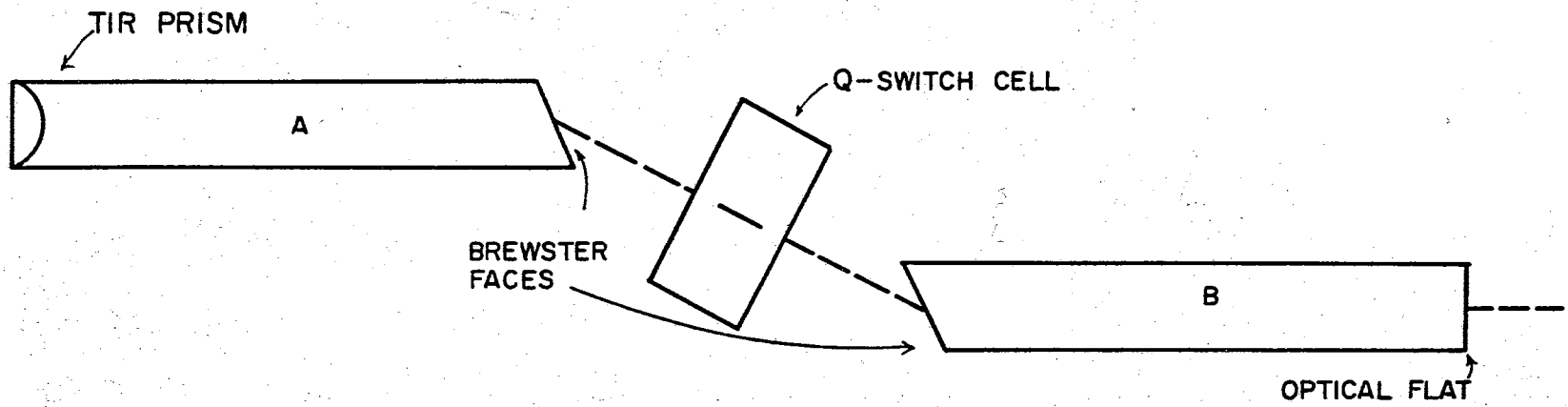


FIG. 5 SCHEMATIC OF TWIN RUBY LASER

photons are emitted.

2. All photons travel parallel to the optical axis of the rubies.
3. There are an infinite number of stimulated atoms.
4. There is a collision each time a photon travels one inch.
5. There is no loss from reflection at the Brewster angles.

The rate equation with the above assumptions is

$$N_d = N_o 2^{dE}$$

where  $N_d$  = number of photons after traveling a distance  $d$ .

$N_o$  = original number of photons.

$d$  = distance traveled in inches.

$E$  = number of collisions per inch = 1.0/inch.

As an example, one photon starting at one end of a six inch stimulated rod will produce the following photons at the other end. Let  $N_o = 1$ ,  $d = 6$  inches,  $E = 1/\text{inch}$

$$N_6 = N_o 2^{dE} = (1)(2)^6$$

$$N_6 = 64$$

Assume that the losses at the Brewster angles are negligible, the schematic drawing in Figure 5 may be further simplified as shown by Figure 6.

With Figure 6 as the basis, diagrams are drawn to show the photon gain and photon output which are produced by a single photon that starts in rod A or in rod B. These diagrams are shown in Figures 7 and 8 for the case where the Q-cell is in place but is not active. The diagrams



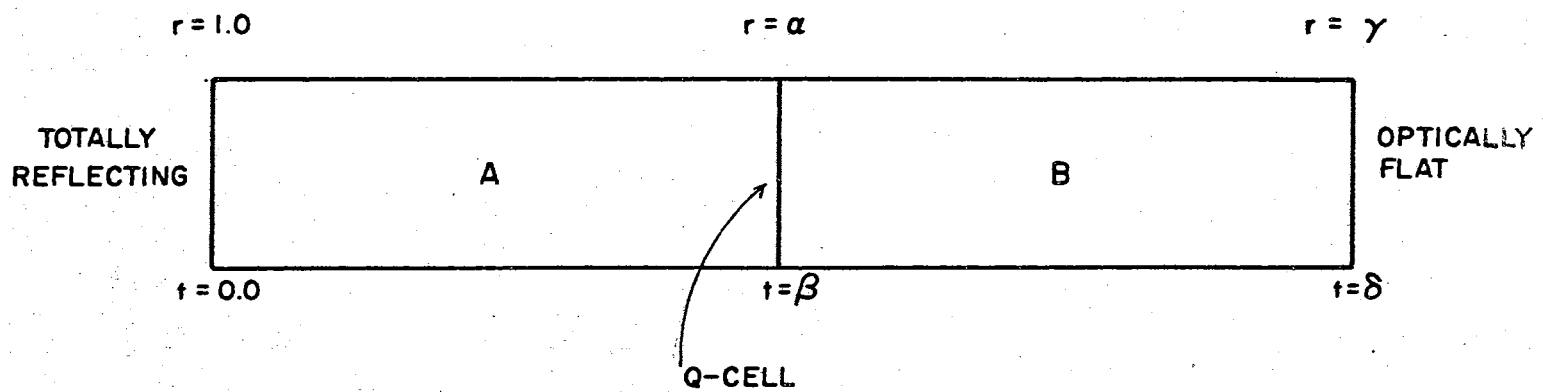


FIG. 6 MODEL OF TWIN RUBY LASER

are drawn for a distance equal to 60 inches of travel in the stimulated rod. Table I shows the photon gain after traveling a specific distance for a photon starting in rod A and a photon starting in rod B. Table II shows the photon output after traveling a specific distance for a photon starting in rod A and a photon starting in rod B. Here we have assumed that  $\alpha = .16$ ,  $\beta = .84$ ,  $\gamma = .04$  and  $\delta = .96$ . The results of Table I and Table II are plotted in graphic form in Figure 9. It is shown that both the gain and the photon output is greatest for photons starting in the generator part (rod A) of the laser.

The same procedure may be employed for the case where the Q-cell is in place between rods A and B and filled with the Q-switching solution. The same type of diagrams will again be used. The only difference in the theoretical approach will be the change in the reflectance and transmittance of the Q-cell as it switches from the no-pass mode to the pass mode. The difference is shown in Figure 10. The diagrams for the photon gain and for the photon output when a photon starts in rod A and in rod B are given in Figures 11 and 12. The results of these diagrams are shown in Table III and Table IV. In the calculations, it was assumed that  $\alpha_1 = .08$ ,  $\alpha_2 = .16$ ,  $\beta_1 = .00$ ,  $\beta_2 = .84$ ,  $\gamma = .04$ ,  $\delta = .96$ . The results from Table III and Table IV are presented graphically in Figure 13. These show that for a Q-switched twin ruby laser, as described previously, rod A may be considered the generator and rod B the amplifier.

#### Laser Beam and Surface Interaction

During the past several years, there have been numerous investigations, (Ehler, (8); Ready, (9); Gregg and Thomas, (10); Honig and

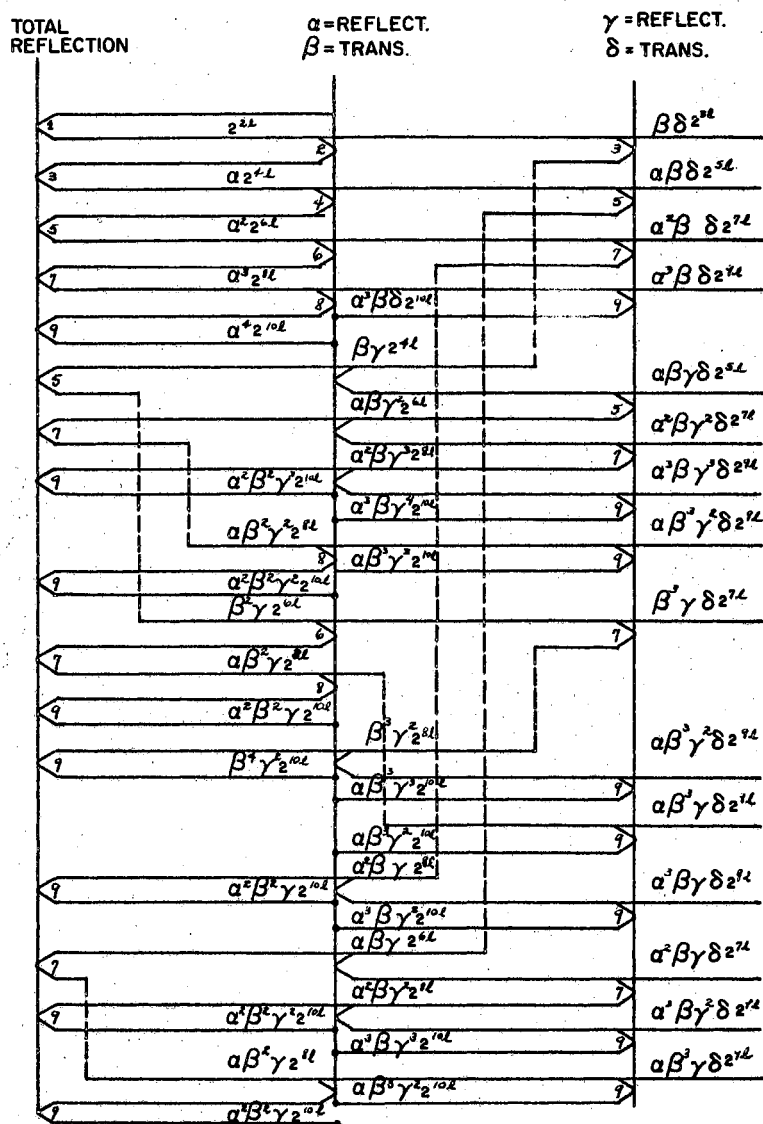


Figure 7. Pass Diagram for Rod A With Non-Active Q-Switch

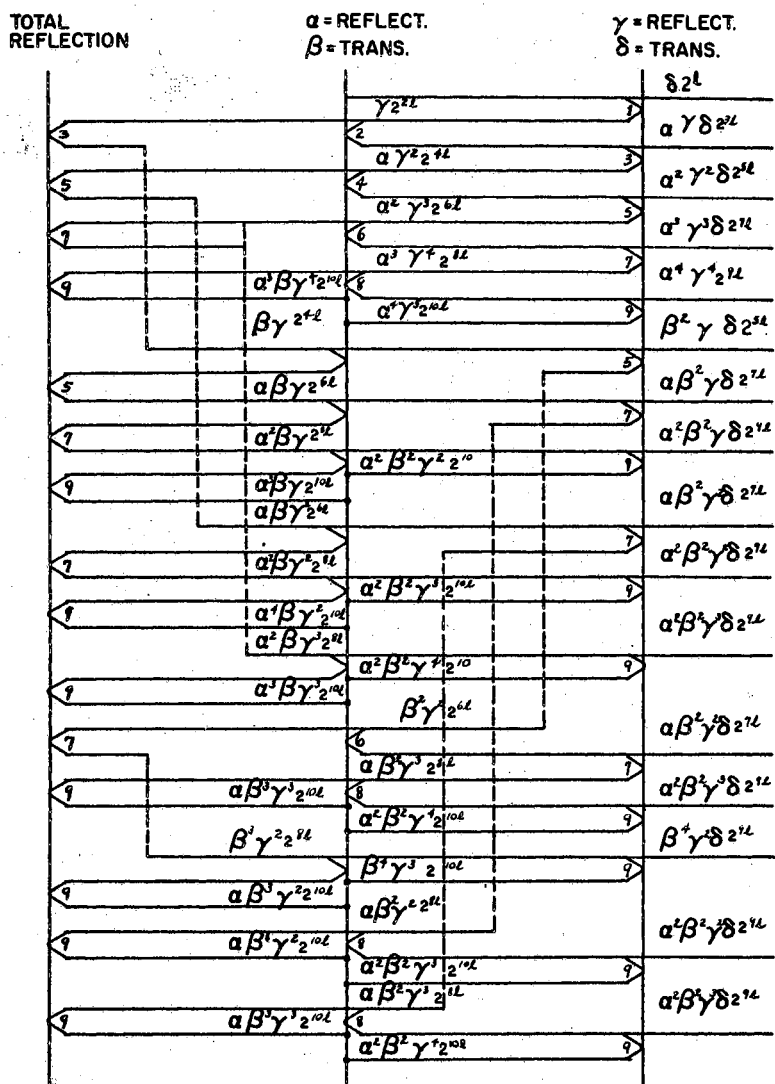


Figure 8. Pass Diagram for Rod B With Non-Active Q-Switch

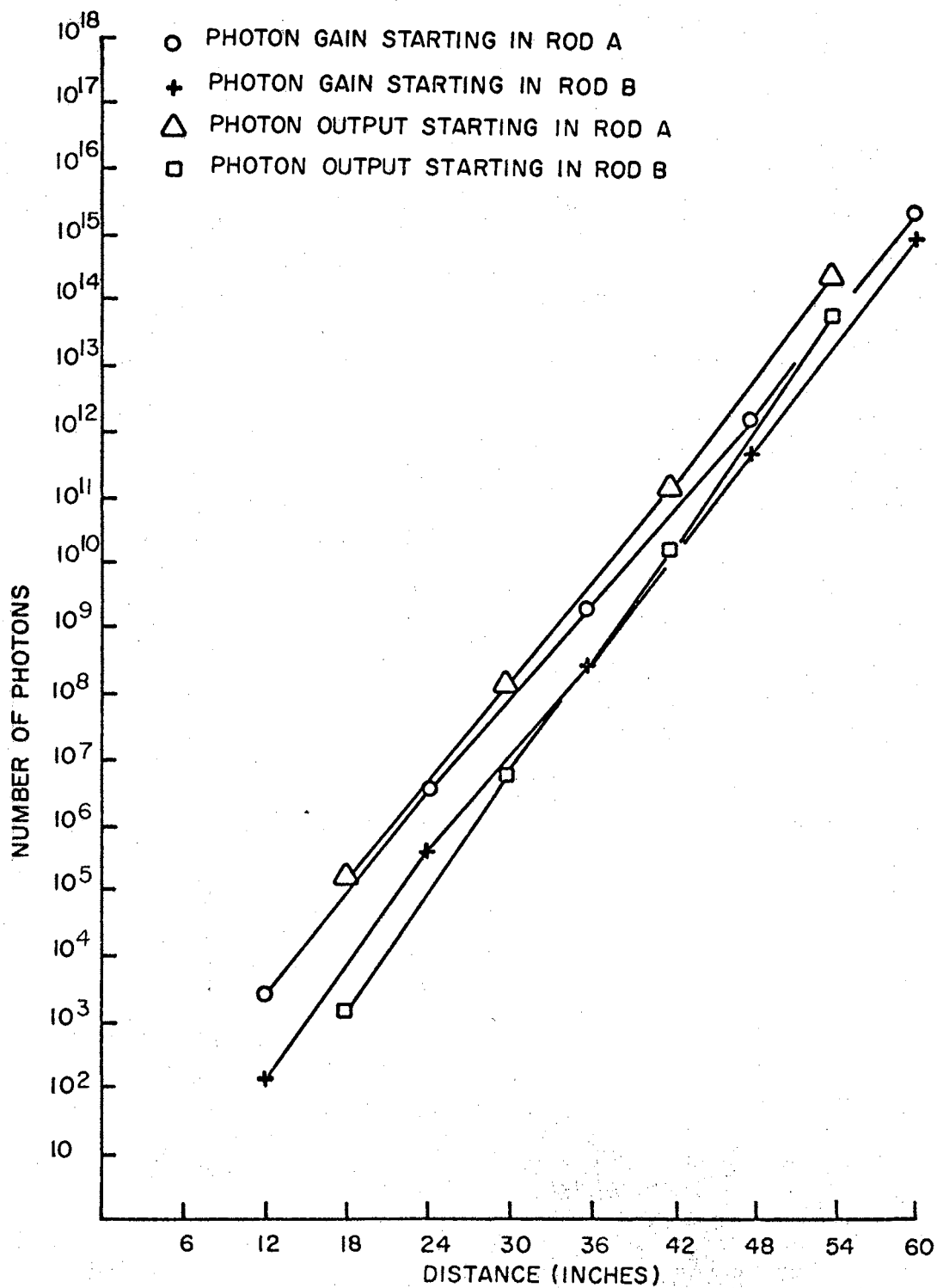


FIG. 9 PHOTON GAIN AND OUTPUT FOR RODS A AND B WITH NON-ACTIVE Q-SWITCH

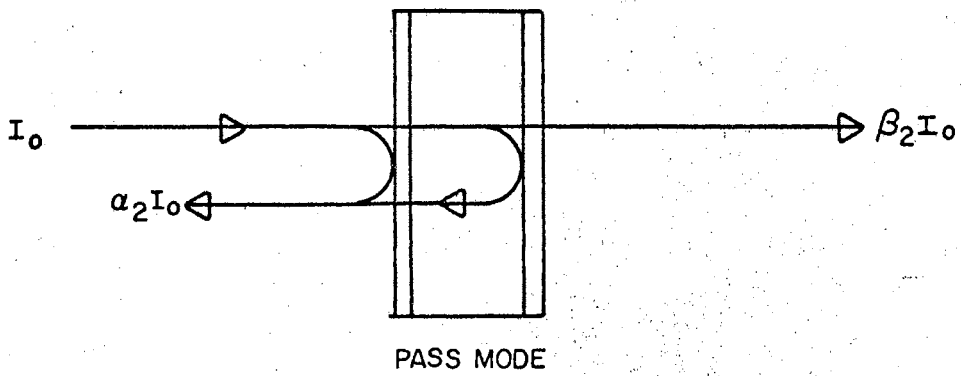
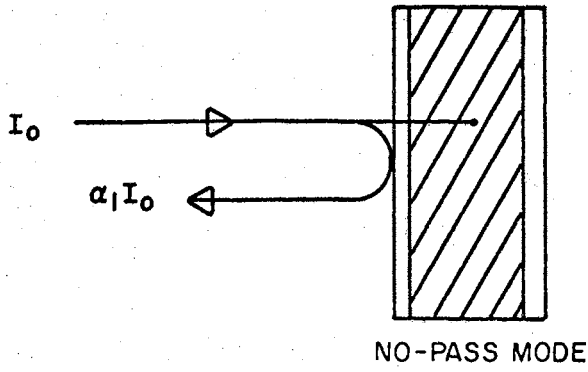


FIG. 10 Q-SWITCH MODE

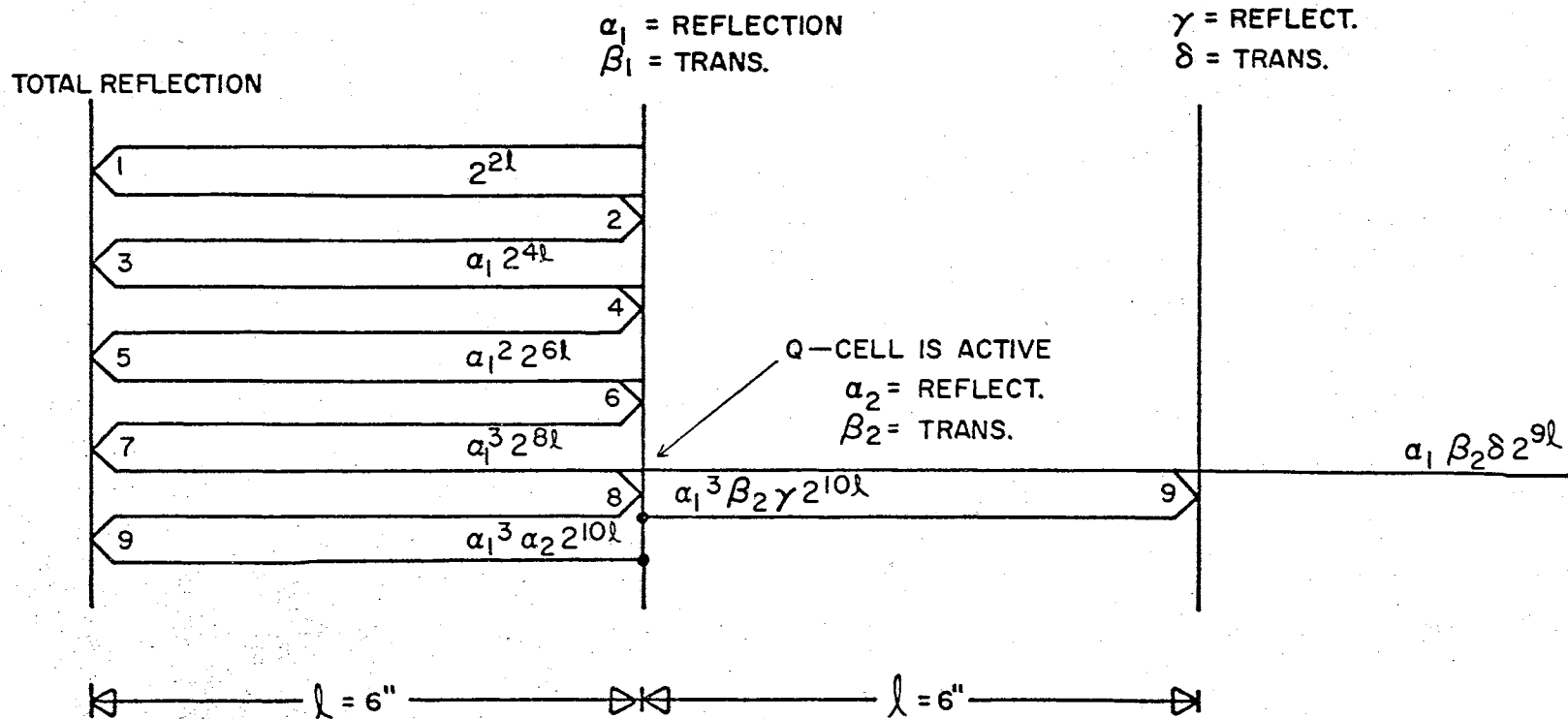


FIG. II PASS DIAGRAM FOR ROD A WITH ACTIVE Q-SWITCH

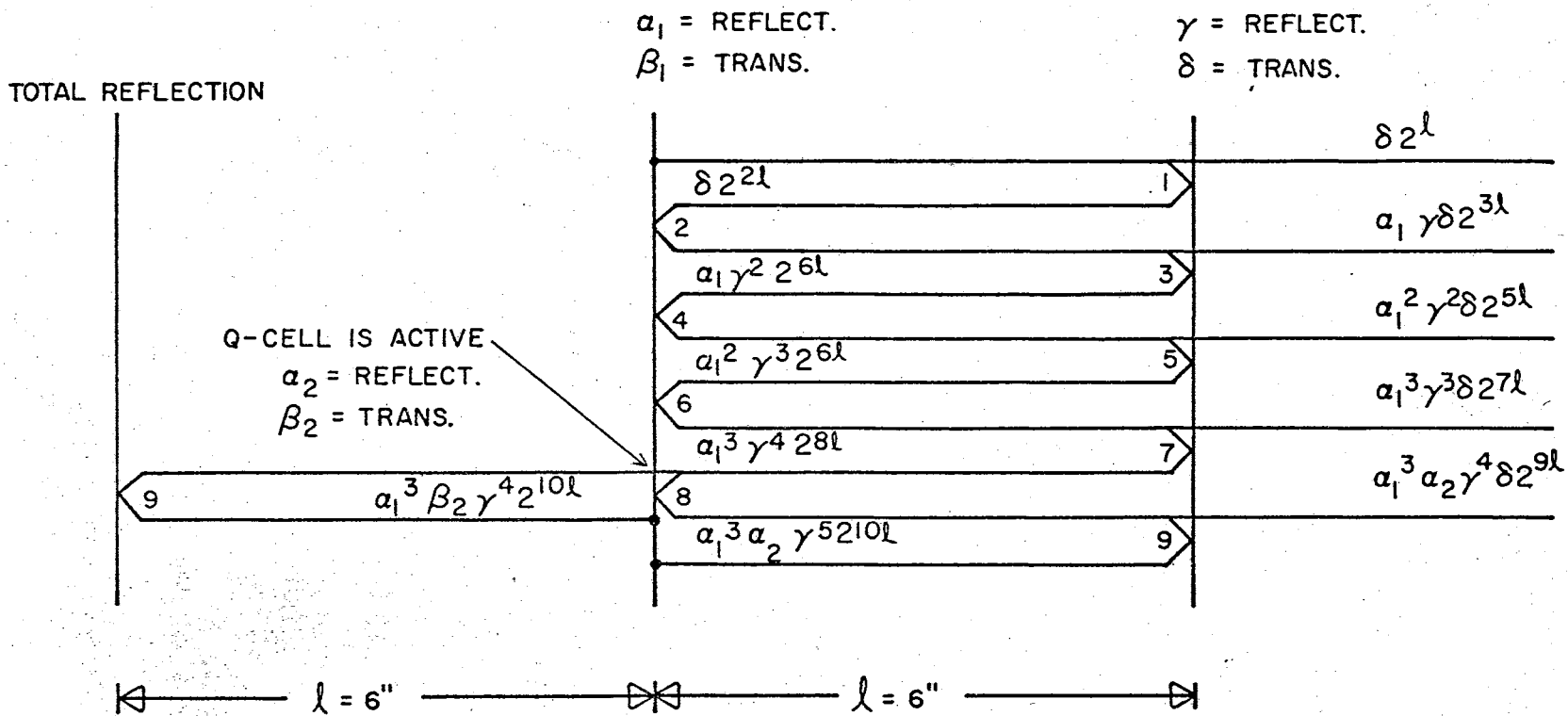


FIG. 12 PASS DIAGRAM FOR ROD B WITH ACTIVE Q-SWITCH



TABLE I

PHOTON GAIN FOR RODS A AND B WITH NON-ACTIVE Q-SWITCH

d (in.)	Starting in A	Starting in B
12	$4.1 \times 10^3$	$1.6 \times 10^2$
24	$4.9 \times 10^6$	$5.8 \times 10^5$
36	$2.4 \times 10^9$	$4.6 \times 10^8$
48	$1.7 \times 10^{12}$	$5.6 \times 10^{11}$
60	$2.4 \times 10^{15}$	$8.2 \times 10^{14}$

TABLE II

PHOTON OUTPUT FOR RODS A AND B WITH NON-ACTIVE Q-SWITCH

d (in.)	Starting in A	Starting in B
18	$2.1 \times 10^5$	$1.5 \times 10^3$
30	$1.4 \times 10^8$	$6.3 \times 10^6$
42	$1.9 \times 10^{11}$	$2.1 \times 10^{10}$
54	$6.1 \times 10^{14}$	$9.2 \times 10^{13}$

TABLE III  
PHOTON GAIN FOR RODS A AND B WITH ACTIVE Q-SWITCH

d (in.)	Starting in A	Starting in B
12	$4.1 \times 10^3$	$1.6 \times 10^2$
24	$1.4 \times 10^6$	$2.2 \times 10^3$
36	$4.4 \times 10^8$	$2.8 \times 10^4$
48	$1.4 \times 10^{11}$	$3.6 \times 10^5$
60	$1.6 \times 10^{14}$	$1.8 \times 10^9$

TABLE IV  
PHOTON OUTPUT FOR RODS A AND B WITH ACTIVE Q-SWITCH

d (in.)	Starting in A	Starting in B
18		$8.1 \times 10^2$
30		$1.1 \times 10^4$
42		$1.3 \times 10^5$
54	$5.7 \times 10^{12}$	$3.6 \times 10^6$

Woolston, (11), of the physical phenomena which occur as a result of the interaction of a focused laser beam with a solid target. The two physical results of laser beam and surface interactions which this paper discusses are mass removal and plasma production.

A literature search has found very little information concerning the amount of mass which is removed by lasers in the Q-switched mode. In contrast, there is a great deal of published information about mass removal with lasers that operate in the normal mode. The number of publications in the latter case is probably a consequence of the application of normal mode lasers for laser machining. Ehler (8) reported a mass removal of about  $.12 \times 10^{-6}$  grams from a tungsten target by a Q-switched ruby laser with an output pulse of .3 joules and a 40-nsec (FWHM) duration. Ehler (12) reported a mass removal of about  $.7 \times 10^{-6}$  grams from an aluminum target with a Q-switched ruby laser that has an output pulse of .2 joules and a 40-nsec (FWHM) duration. Ehler measured the heat transfer to the target by observing the temperature rise of a small mass target. A thermocouple was embedded in the target. He found that the energy to heat the target was about 5 percent of the laser pulse energy. The laser light that was reflected and scattered by the target and plasma was measured to be about 1 percent of the incident energy. About 3 percent of the laser energy was required to evaporate the  $.7 \times 10^{-6}$  grams of aluminum from the target. He thus estimates that over 90 percent of the laser pulse energy must be absorbed by the plasma which is formed about the impact area.

Similar calculations were made for the laser beam and surface interactions described in this paper. These calculations are presented in Chapter V with the data.

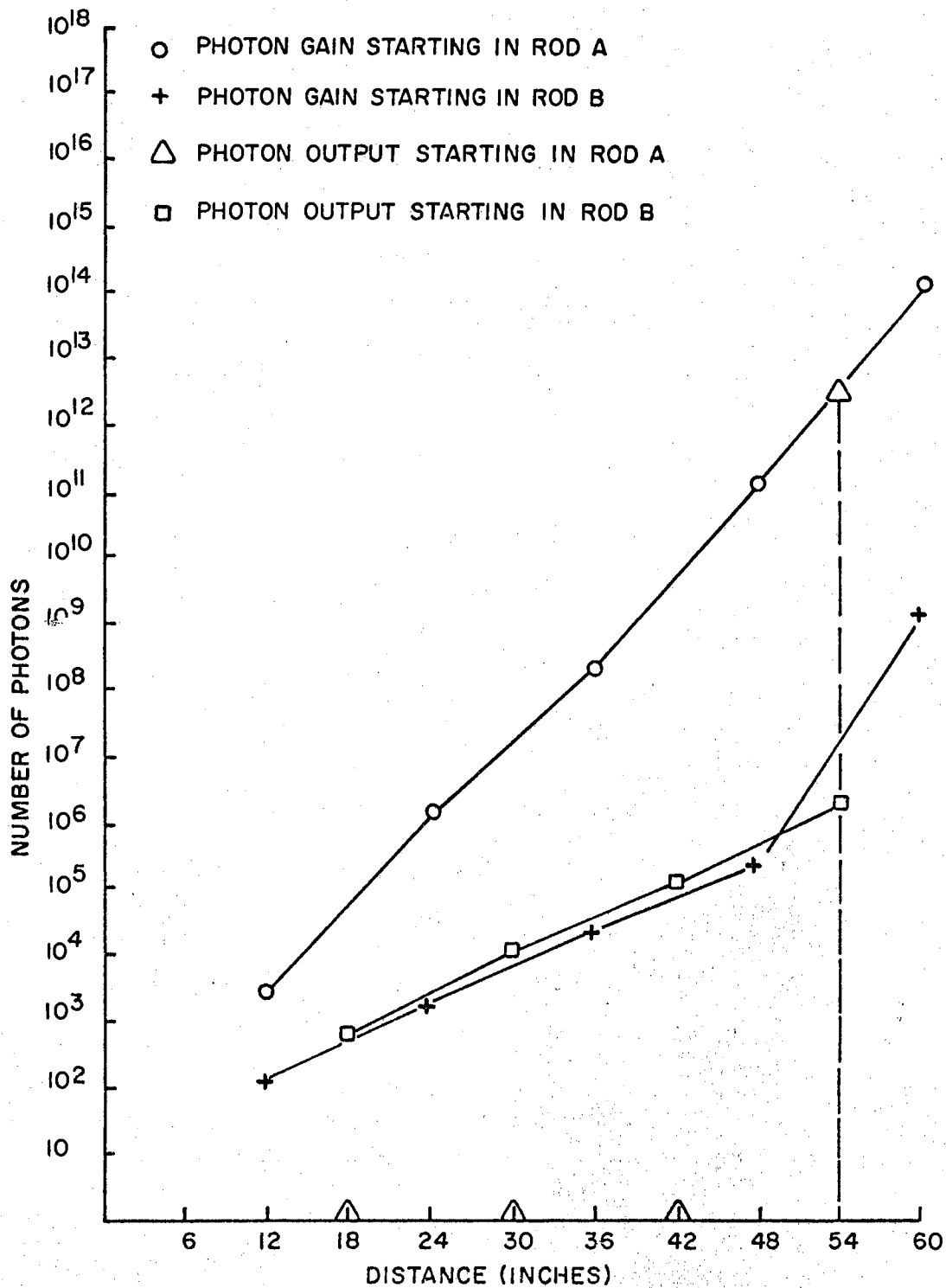


FIG. 13 PHOTON GAIN AND PHOTON OUTPUT FOR RODS A AND B WITH ACTIVE Q-SWITCH

Before describing the experimental work undertaken by the author, the present state of knowledge is presented of plasma production from the interaction of a focused, Q-switched laser beam with a solid target. Consider a solid target which is irradiated by a short duration, focused laser beam. If the target is metallic, the initial laser pulse is partially reflected and partially absorbed. The absorption of the laser radiation starts at the surface of the target and decreases exponentially with depth. Ready (13) obtained high speed photographs of the laser beam and target surface interaction. The photographs showed a bright spot of emission on a carbon target which started about 45 nanosecs after the start of the laser pulse. Ready (13), in an attempt to describe a model for the laser beam and target interaction, states that the surface of the metal rises to the vaporization temperature and begins to vaporize. The vaporized material recoils against the surface and produces a high pressure. He further states that this pressure pulse raises the boiling point of the underlying material which becomes superheated as more heat is conducted into the interior. Ehler (8) found that heating and evaporation of a tungsten target occurred at the beginning of the laser pulse. Ehler also showed, with the use of a probe, that electrons are ejected from the target during the time that the laser pulse was observed and that some time later ions reached the probe. This has also been reported by Basov et. al. (14), Opower and Burlefinger (15). Namba et al. (16) reported that two ion peaks occurred after interaction started between the laser beam and the surface. In the above references, the probes were within a distance of 3 cm from the impact area. Hirono and Iwamoto (17) found that a probe at a distance of 30 cm from the impact showed the electrons and ions arriving at the same time, indicating

a neutral plasma.

Several investigators have estimated the ion energies from the ion velocities that are found by probe measurements. These results are shown in Table V. Some investigators have also estimated the plasma temperatures by spectroscopic methods. Ehler and Weissler (19) used a 0.5 meter, normal incidence, vacuum spectrograph and a 2 meter, grazing incidence, vacuum spectrograph to observe the laser induced plasmas of platinum, tungsten, aluminum, beryllium and nickel. Spectra of the above targets showed that plasmas were produced with temperatures of around 10 ev. Gregg and Thomas (10) used a monochromator and photomultiplier to look at the laser produced plasmas of beryllium, lead and aluminum in the wavelength region of 4,000 to 10,500 angstroms. From this data they calculated the following peak blackbody temperatures;

Beryllium	-	$8 \times 10^5$
Lead	-	$3 \times 10^5$
Aluminum	-	$5 \times 10^5$

Ehler (8) found a plasma temperature of 30 eV for tungsten by the use of a grazing incidence, vacuum spectrograph. Fawcett et al. (20) used a 2 meter grazing incidence, vacuum spectrograph to record the spectra that is produced by laser beam impact on an iron target. Assuming an optically thin continuum, their spectra showed an electron temperature which approached 100 eV.

Possible, particle emission mechanisms are discussed which may exist when a laser beam and a surface interact. For convenience, these mechanisms are summarized in Figures 14, 15, 16, 17 and 18.

Probably, the first particles to be emitted from an irradiated

TABLE V  
 REPORTED ION ENERGIES AND VELOCITIES FROM PROBE MEASUREMENTS

Investigator	Target	Ion Velocity	Ion Energy
Ehler	Al.	$1.0 \times 10^7$	1300 eV
Ehler (8)	W	$3.2 \times 10^6$	900 eV
Namba et. al. (16)	Ta		100 eV
Namba et. al. (16)	Ta		1 eV
Basov et. al. (14)	Ca	$1.6 \times 10^7$	1600 eV
Opower and Burlefinger (15)	Ca	$1.3 \times 10^7$	1000 eV
Linlor (18)	Al.	$6.0 \times 10^6$	1000 eV

surface are electron. The electrons have a small mass and a short time is required for transition from a bound to an unbound state. According to Mott and Jones (21), light is absorbed in metals by internal photo effects which raise the electrons to higher energy states in the conduction band. In a good conductor, the mean free time between collisions for electrons is of the order of  $10^{-14}$  to  $10^{-13}$  sec. As a consequence, for times of the order of  $10^{-9}$  to  $10^{-8}$  sec, the electrons make many collisions among themselves and with lattice phonons. From the latter collisions, the energy of the electrons is distributed and passed to the lattice. The energy which is absorbed from the initial part of the laser beam pulse is regarded as having been converted almost instantaneously into heat. It appears to be reasonable for the heat of vaporization of the target material to be attained within the first few nanoseconds of the laser pulse. The rapid expansion of the vapor from the transformation from solid to vapor will result in some neutral vapor being formed above the impact area. As the neutral vapor above the target continues to absorb laser radiation, many of the neutral atoms will be excited to higher energy levels and some ionization occurs.

In materials which have high melting and boiling points and/or low work functions, the primary electron emission mechanism for laser beam and surface interactions is probably thermionic emission. The thermionic emission electron current density,  $J_{\text{therm}}$ , is given by Sproull (22) as,

$$J_{\text{therm}} = \frac{(4 \pi m e)}{h^3} (kt)^2 \exp \frac{(-3 W)}{kt} \frac{\text{amps}}{\text{m}^2} \quad (24)$$



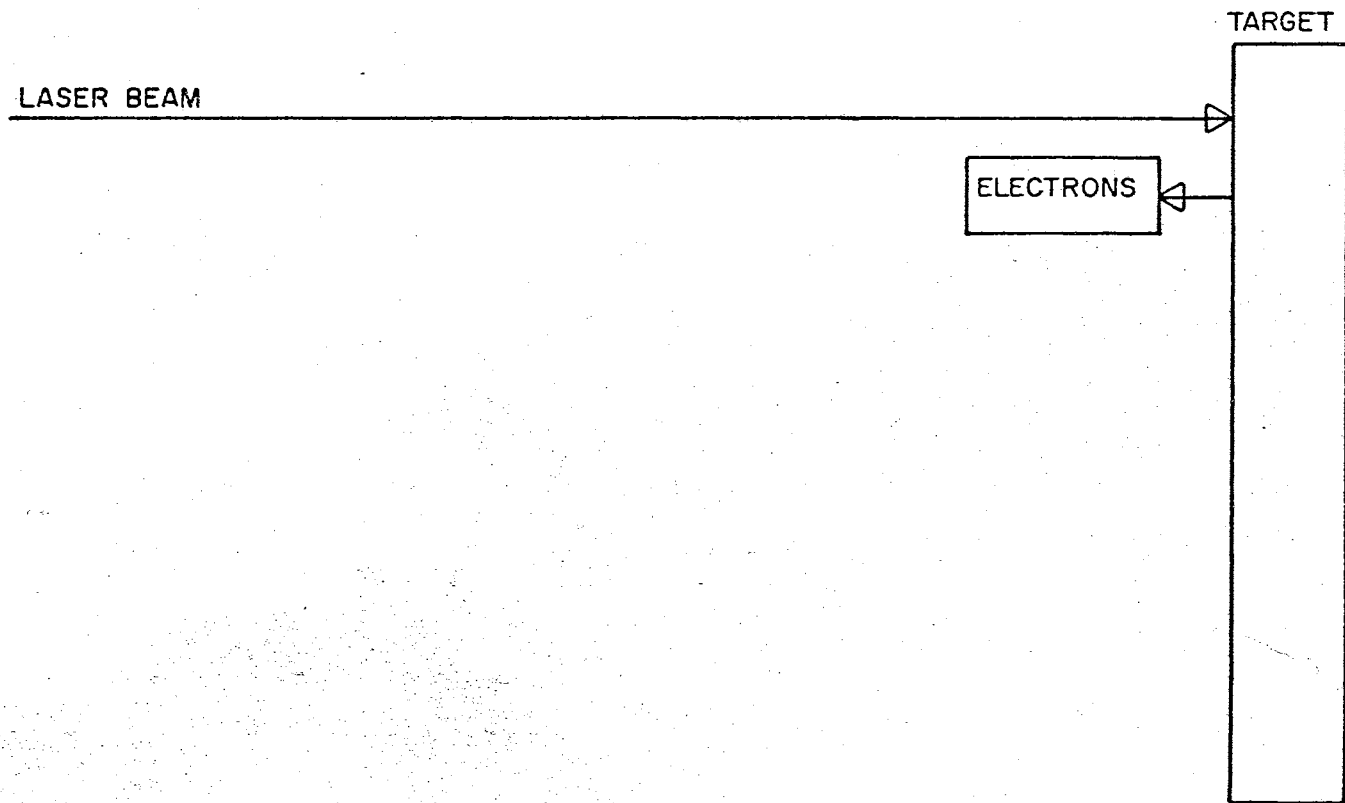


FIG.14 PARTICLE EMISSION 0-5 nsec AFTER LASER BEAM IMPACT

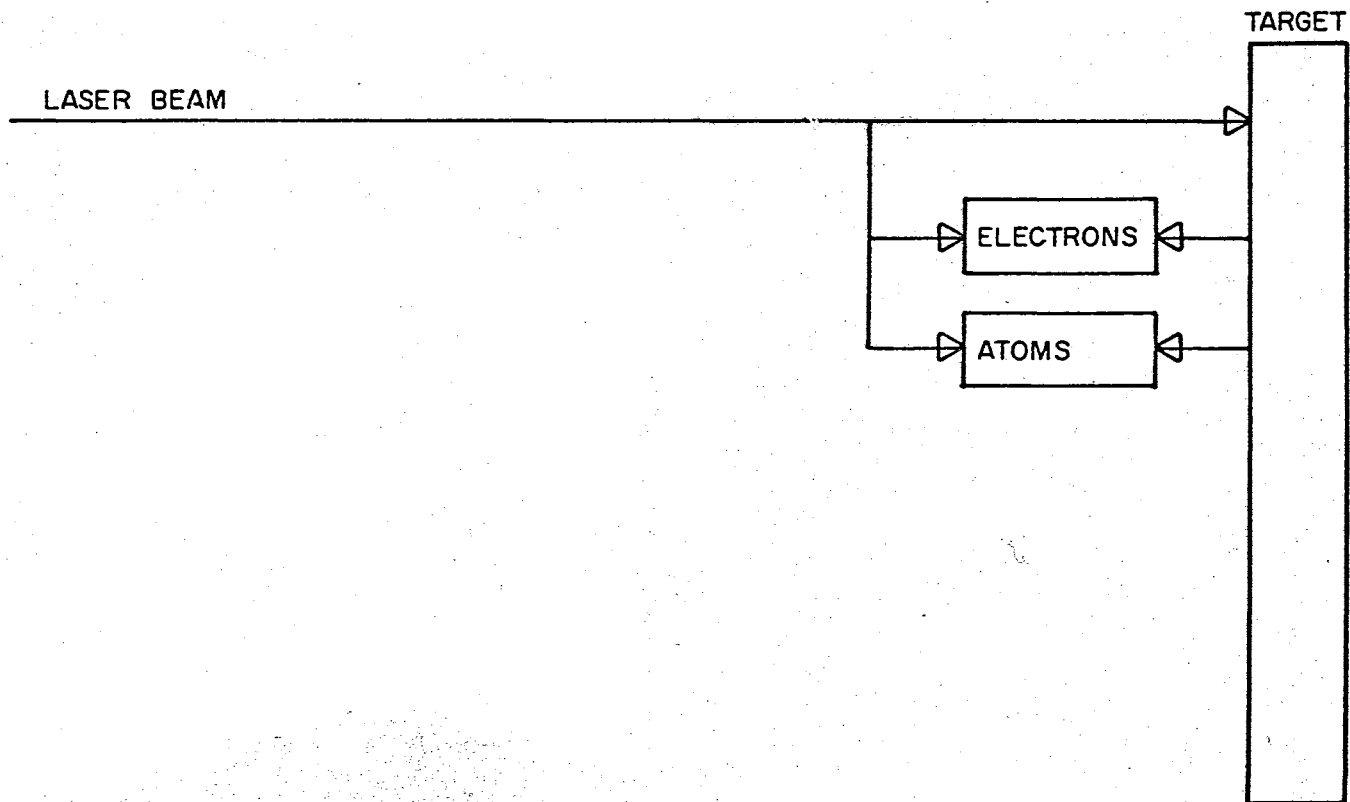


FIG. 15 PARTICLE EMISSION 5-10nsec AFTER LASER BEAM IMPACT

where  $m$  is the mass of the electron,  $e$  is the charge on the electron,  $h$  is Planck's constant,  $k$  is Boltzmann's constant,  $t$  is the surface temperature in degrees Kelvin, and  $W$  is the electron work function of the target. Equation (24) is derived on the assumption that only those electrons escape which have sufficient momentum normal to the surface to overcome the surface potential barrier.

Intense electron emission results from the bombardment of the emitting surface by excited atoms. This is the usual explanation of neutralization of ions at a surface. Electron emission is further increased by bombardment of the surface with electrons to give secondary electron emission. It has been estimated for ion neutralization by Oliphant (23) and Dorrestein (24) from experiments and Massey (25) and Cobas and Lamb (26) from theoretical calculations, that the yield probably lies between .1 and 1 electron per incident atom, provided the excitation energy of the excited atom exceeds the work function of the material.

Ion emission from the target surface is probably enhanced when atoms near the target surface are excited by electrons or photons emitted from the vapor above the impact area. It is also evident that since the electrons are accelerated away from the target more quickly than the ions, there must be a negative cloud of electrons which help to accelerate the ions away from the target surface. This ambipolar diffusion may explain why probe measurements taken close to the impact area show a distinct separation between electrons and ions. Whereas probe measurements taken at a large distance from the impact area show a fairly neutral plasma. Since thermal ions most probably have very low energies, ambipolar diffusion may also account for the relative high ener-

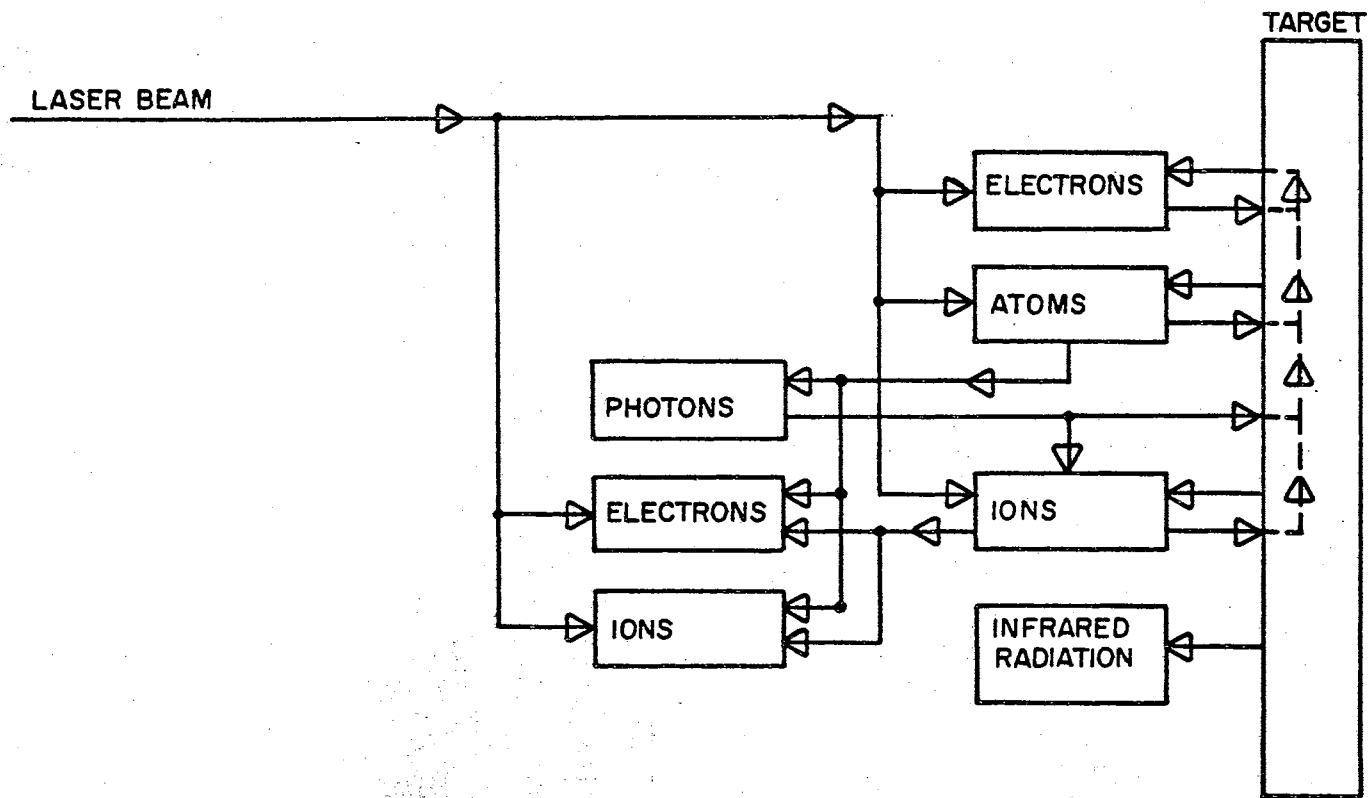


FIG.16 PARTICLE EMISSION 10-50nsec AFTER LASER BEAM IMPACT

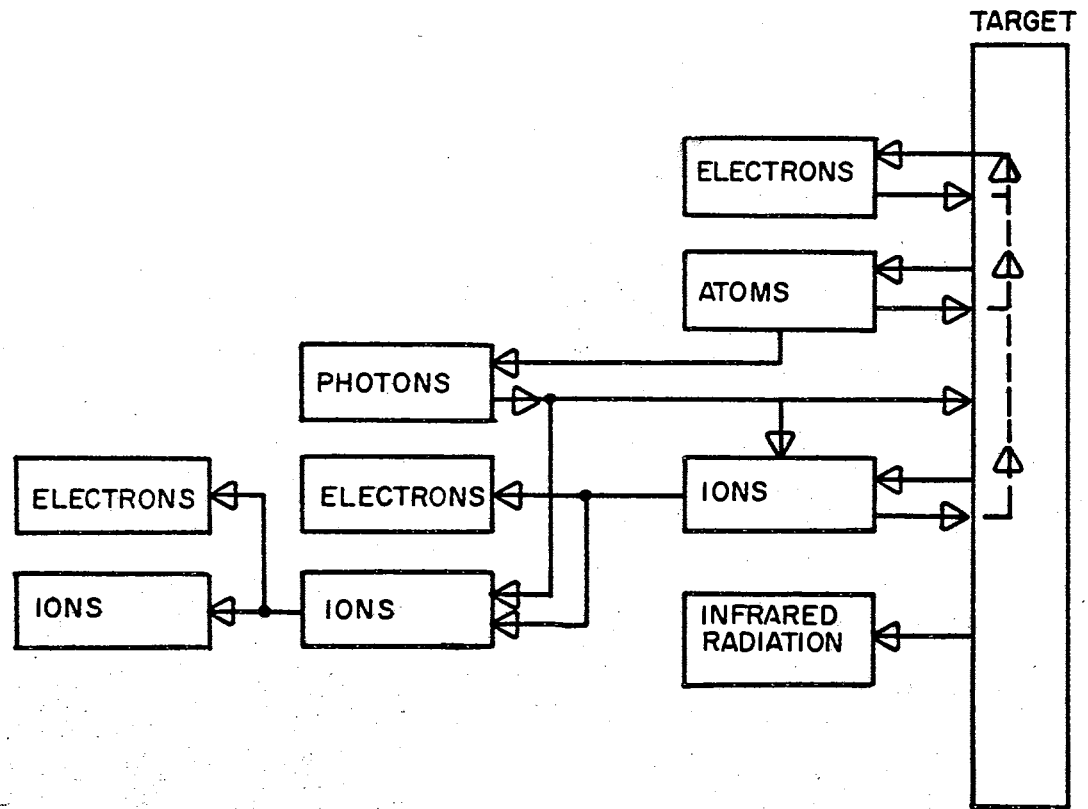


FIG. 17 PARTICLE EMISSION 50-100nsec AFTER LASER BEAM IMPACT

gies of the ions.

As some vapor, ions and electrons are formed above the surface of the target, absorption of the laser beam continues and more ions, electrons and excited atoms are produced.

Eventually, the particle density becomes high enough so that practically all of the laser beam is absorbed by the particles which had initially been emitted from the target surface.

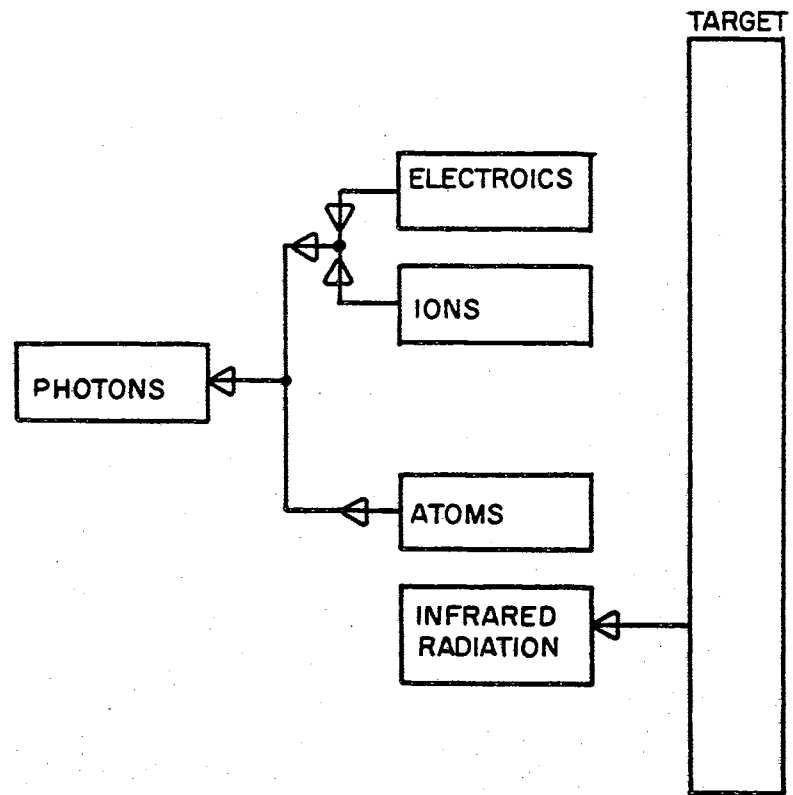


FIG. 18 PARTICLE EMISSION 100-400nsec AFTER LASER BEAM IMPACT

## CHAPTER III

### MODIFICATION IN LASER DESIGN

As stated in the introduction, the work presented in this paper is a continuation of the project started by L. J. Peery (27). Due to slight changes in experimental objectives and the lack of reliability which is inherent in prototype work of this magnitude, there was the need for certain modifications in the initial laser facility. This chapter will describe the modifications undertaken by the author to improve the reliability of the facility and the compatibility to the experiments undertaken.

#### Optical

This section is a discussion of the laser cavity, consisting of the rubies, Q-switch and external reflector. The laser cavity is shown schematically in Figure 19 and an actual photograph is shown in Figure 20.

The laser presented in this paper consists of two ruby rods as the active element. The generator rod is 6.0 inches long and 0.5 inches in diameter. One end of the generator rod was cut and polished in the shape of a TIR prism for 100 percent reflection. The other end was cut and polished at Brewster's angle ( $60^{\circ} 27'$ ). The amplifier rod is also 6.0 inches long and 0.5 inches in diameter. One end of the amplifier rod was cut and polished at Brewster's angle and the other end was cut



at a right angle to the optical axis of the ruby. All surfaces are polished to  $\lambda/10$  finish except the sides of the rubies which have a matte finish.

The rubies were originally mounted as shown in Figure 21. The ruby holder was redesigned as shown in Figure 22. The main problem involved in designing a mount for the ruby is that of thermal expansion. Light energy and heat absorption from the flashlamps cause thermal expansion of the rubies. Since the rods are held vertically, they must be held fairly rigid to insure alignment and yet they can not be held too rigid because of possible damage to the rubies during expansion. The final design shown in Figure 22 has worked well throughout the experimental work.

The glass sleeve surrounding the rubies served to protect the rubies in the event of flashtube failure and to absorb the ultraviolet radiation from the flashtubes which tends to cause a certain degree of "bleaching". The glass sleeve was attached to the brass holder with epoxy. Since all epoxies decompose under the influence of u.v. radiation, it was necessary to dismantle, clean and reapply epoxy to the glass sleeve and sleeve holder after ten or fifteen firings. The glass sleeves also had a tendency to crack as a result of the difference in thermal expansion of the glass and the brass holder.

Because of mechanical difficulties encountered during the alignment of the Q-switch cell, the adjustable mount which holds the Q-cell was redesigned. The redesigned Q-cell mount is shown in Figure 23. This type of mount allows angular adjustment of less than 1.0 mrad, as can be seen from the following calculations. The adjusting screws have 28 threads per inch. Thus, a turn of  $1/8$  revolution advances point A a

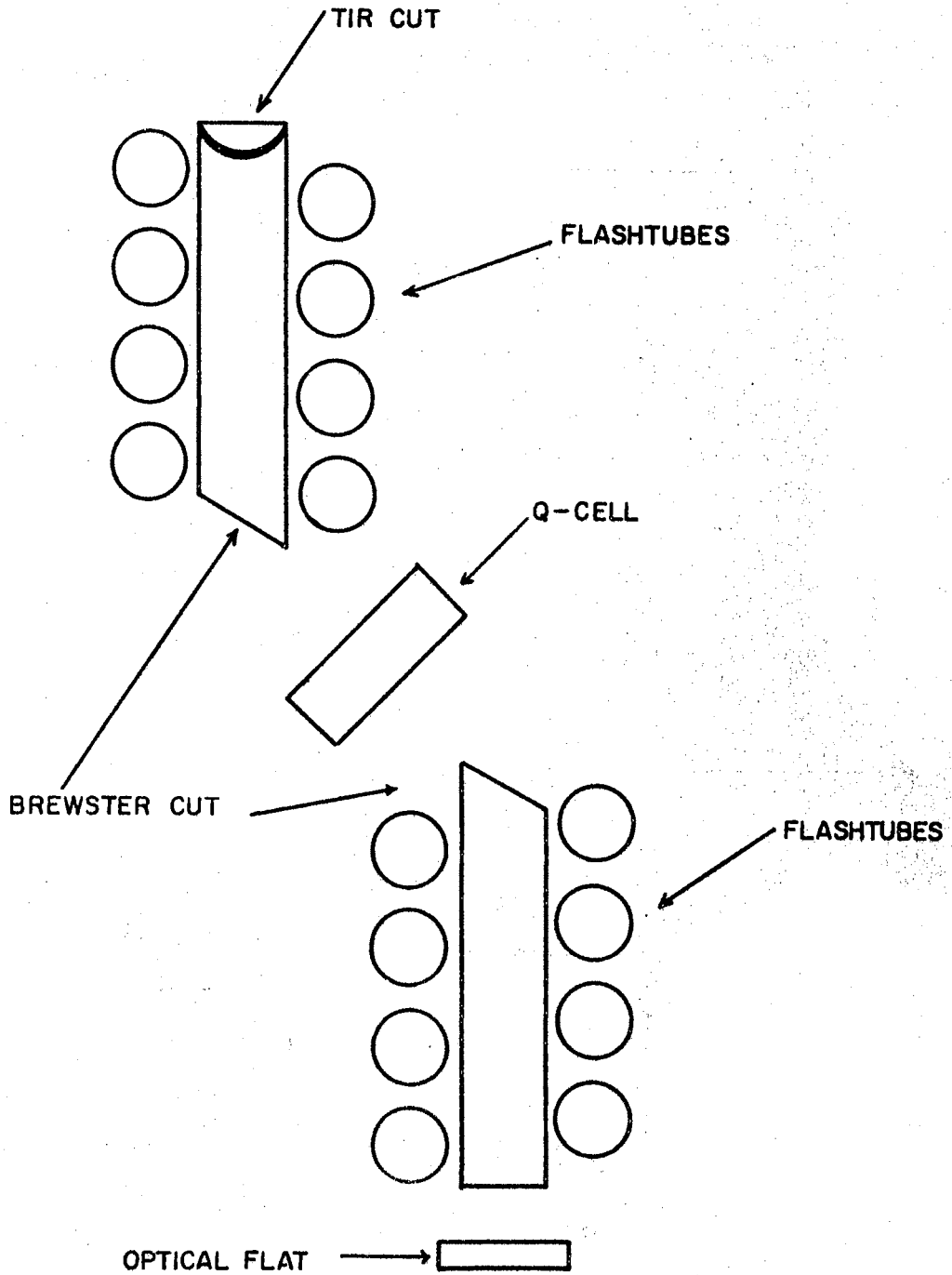


FIG. 19 SCHEMATIC OF TWIN RUBY LASER

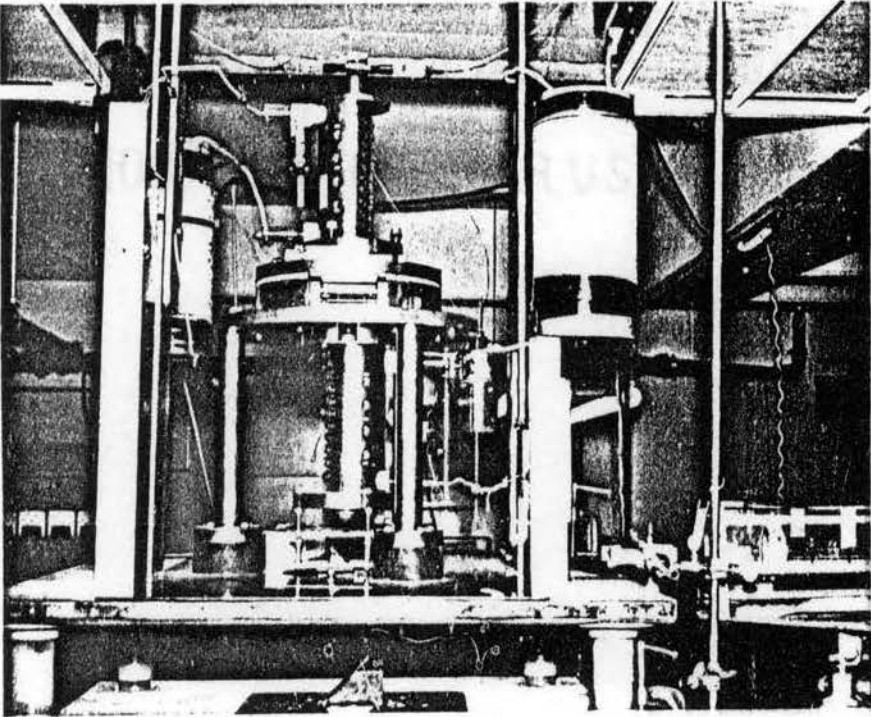


Figure 20. Photograph of Laser Cavities

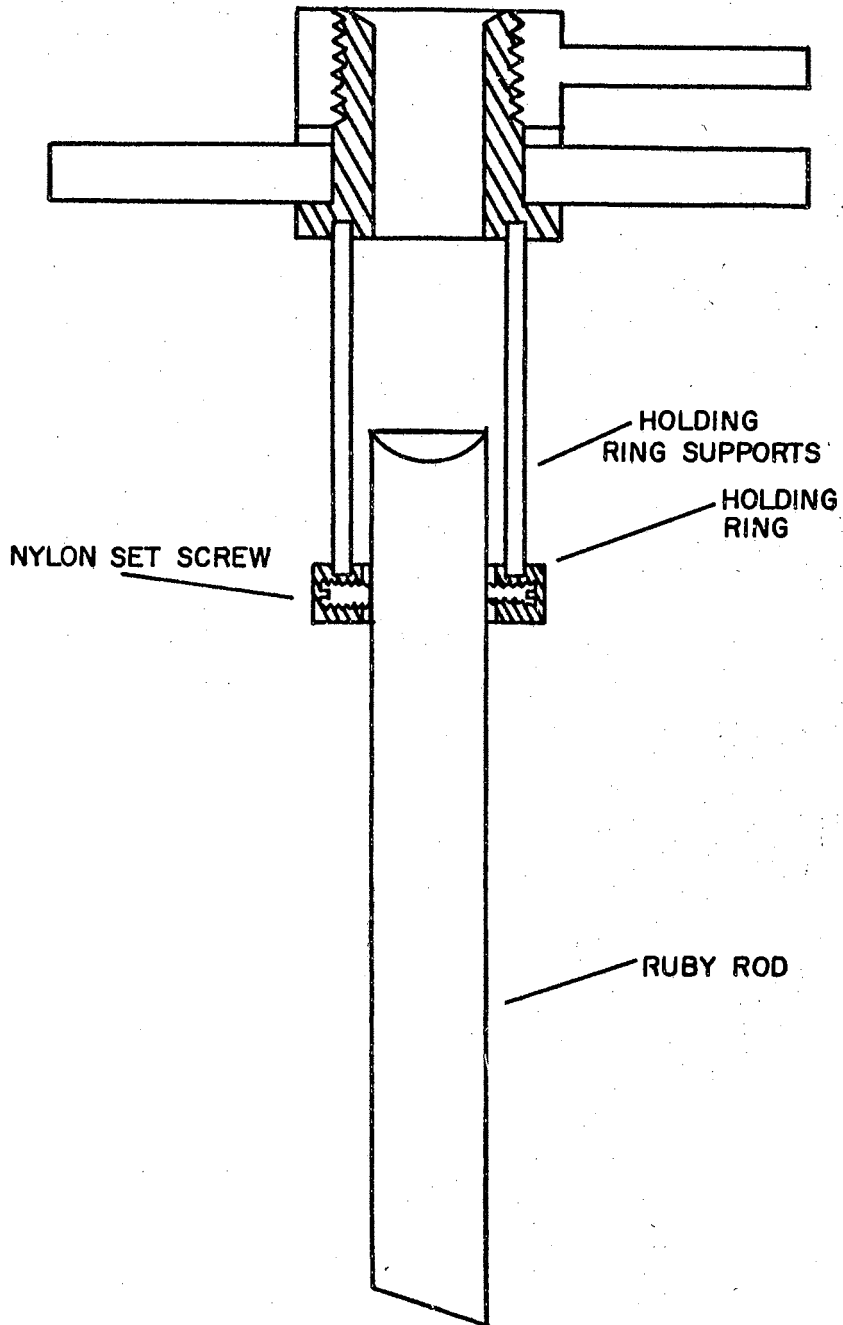


FIG. 21 PEERY'S RUBY MOUNT

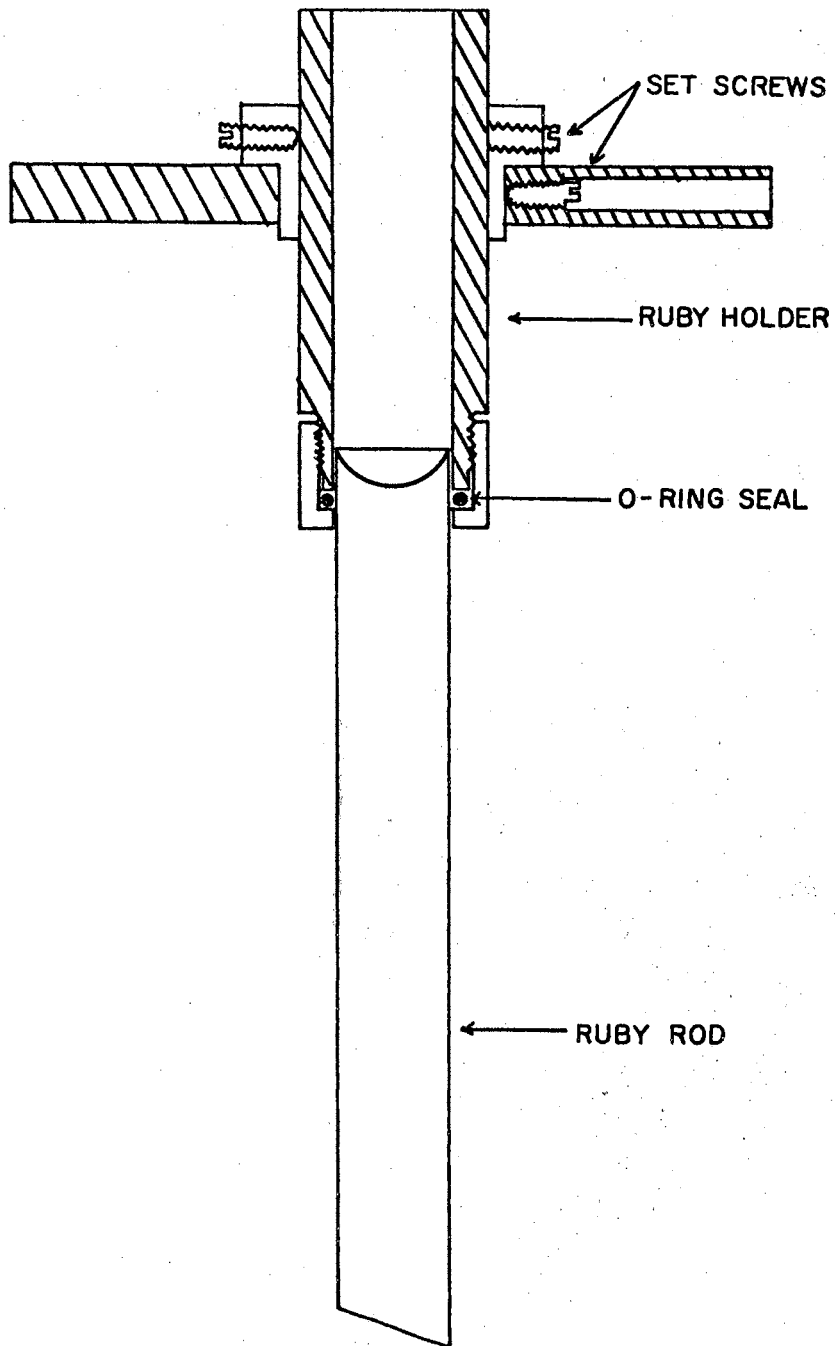


FIG. 22 MODIFIED RUBY MOUNT

distance of approximately .004 inches. Since the ratio of AB to CB is about 2:1, point C moves a distance of approximately .002 inches. The distance from D to C is 1.75 inches, thus, giving an angular adjustment of  $\theta = s/r$  where  $s$  is the distance point C moves and  $r$  is the distance from D to C. The angular adjustment is then given as,

$$\theta = \frac{s}{r} = \frac{.002''}{1.75} \quad (25)$$

$$\theta \cong 1.1 \text{ mrod.}$$

Thus, it is seen that an angular adjustment of 1.0 mrod is easily obtained.

To increase the gain of the optical cavity an external reflector was added to the output end of the amplifier rod. The reflector was in the form of an optical glass flat having three adjusting screws. The optical flat and mount are shown in Figure 24. The reflectance of the flat is approximately 8 percent at  $6943 \text{ \AA}$  as measured with a spectrophotometer. Each adjusting screw has 28 threads per inch. The distance between adjusting screws is five inches. An adjustment of 1/8 revolution moves one point of the reflector mount .0045 inches. Assuming the angular displacement of the reflector to be  $\theta = \frac{s}{r}$ , we have for  $\theta$

$$\theta = \frac{s}{r} = \frac{.0045''}{5.0''} = .0009 \text{ rod.} \quad (26)$$

$$\theta \cong 1 \text{ mrod.} \quad (27)$$

Thus, an angular adjustment of less than 1.0 mrod. is possible for the external reflector.

The differential screw adjustments used by Peery to position the

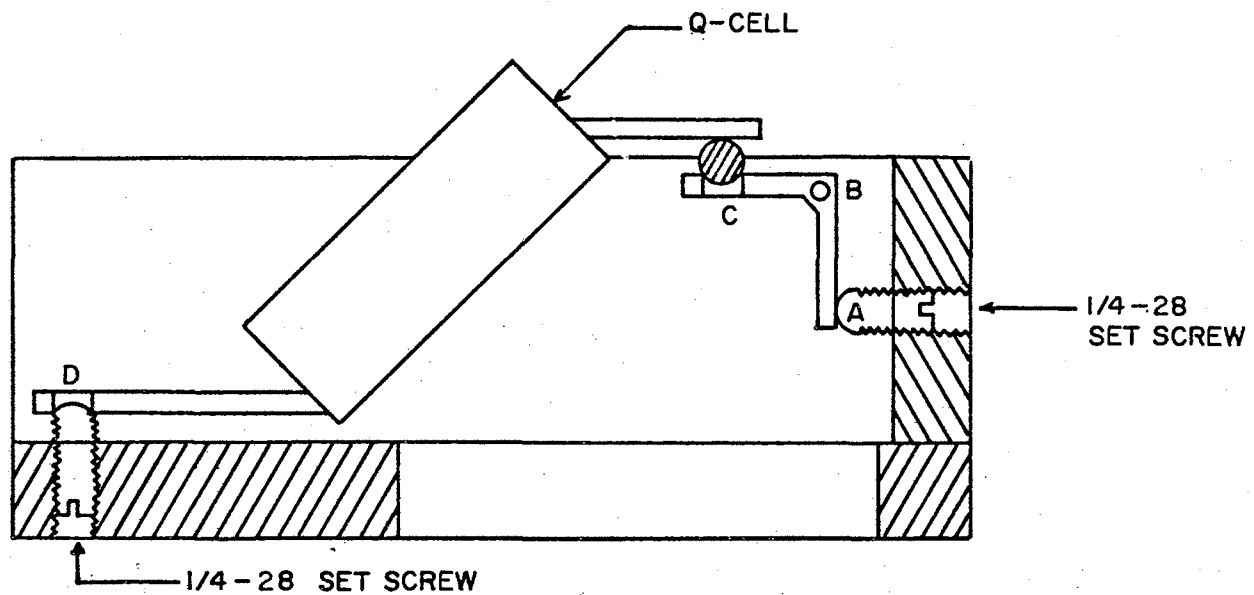


FIG. 23 Q-CELL MOUNT

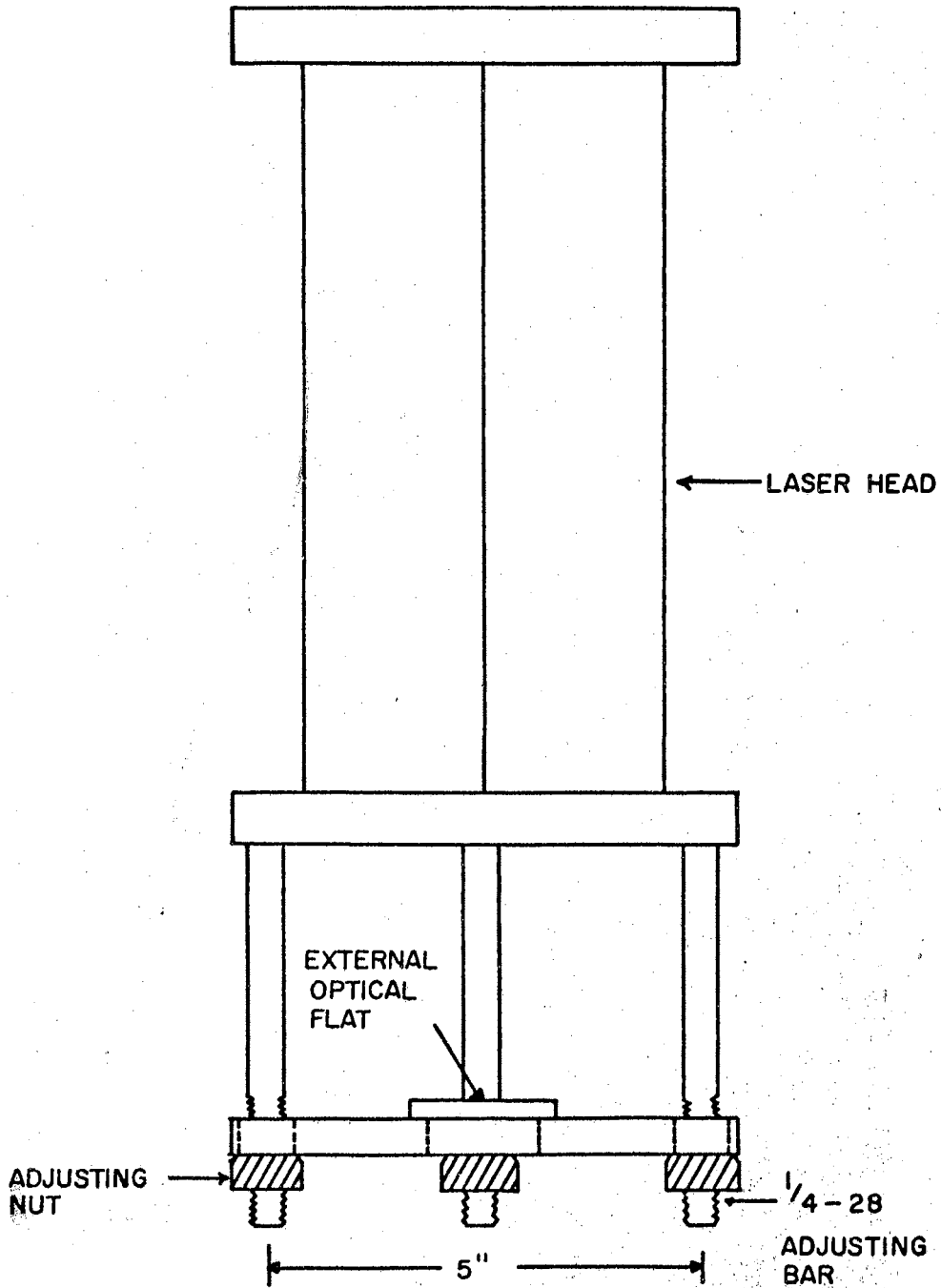


FIG. 24 EXTERNAL REFLECTOR



generator ruby served satisfactorily except for a small amount of play in the differential screws themselves. The play in the differential screws was taken out with stiff springs so that the screws were always under tension. The differential screw adjustment is shown in Figure 25.

The major optical problem encountered with the laser was that of optical component alignment. The following optical components must be properly aligned to insure maximum delivery of laser energy to the target surface,

1. Generator rod
2. Q-Switch
3. Amplifier rod
4. External reflector
5. Focusing lens

Originally, alignment was attempted by Peery using a point source, collimating lens and reticle. The alignment optics used by Peery are shown in Figure 26. Although this method of alignment worked fairly well, the alignment process became very tedious due to the low intensity of the light source and the light absorption of the rubies. The modified alignment method initiated by the author will be described in the following paragraphs.

The main component in the modified alignment system is a He-Ne gas laser purchased from Electro Optics Associates. The gas laser was operated at an output of approximately 1.4 milli-watts. The modified alignment system and optical components are shown schematically in Figure 27.

The alignment procedure used to obtain maximum laser output, in the sequence they are performed is given as:

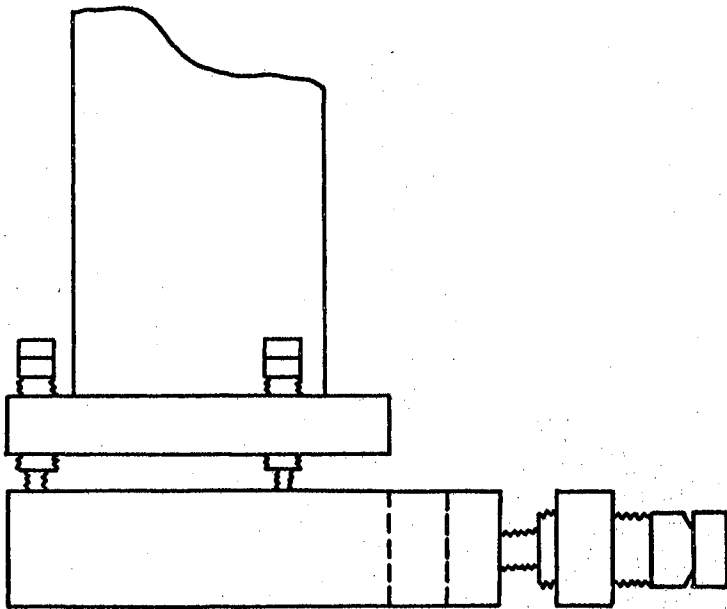
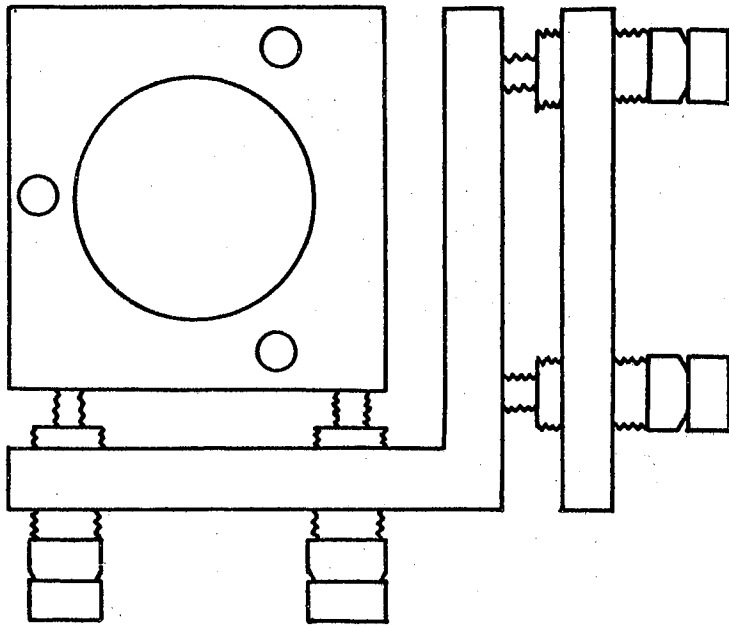


FIG. 25 HORIZONTAL AND VERTICAL ADJUSTMENT  
OF GENERATOR

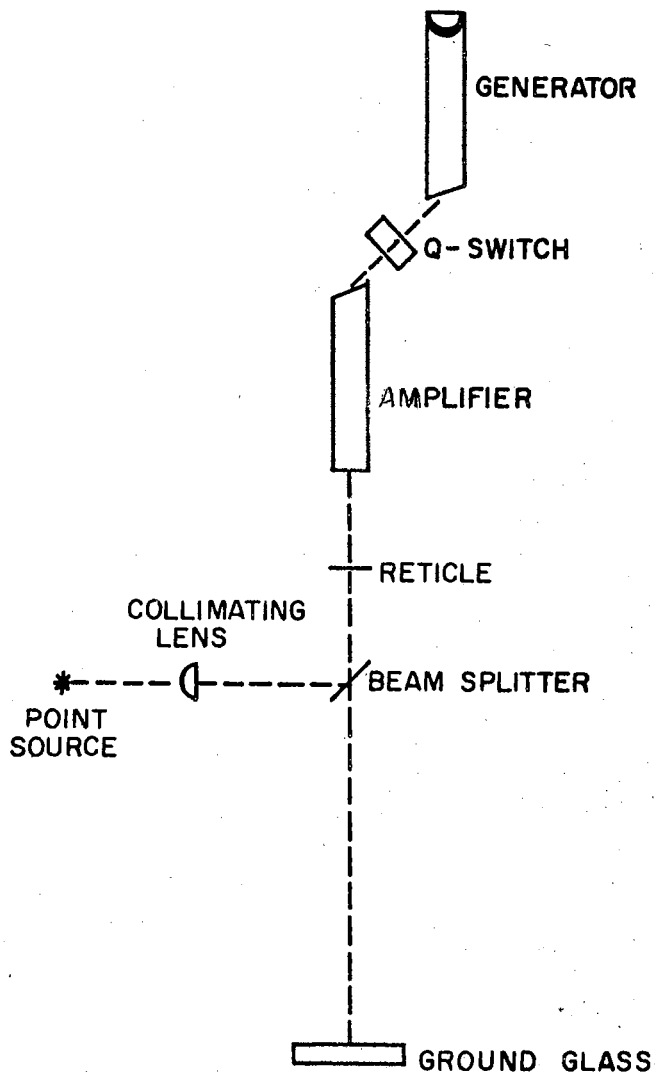


FIG. 26 SCHEMATIC OF PERRY'S ALIGNMENT OPTICS

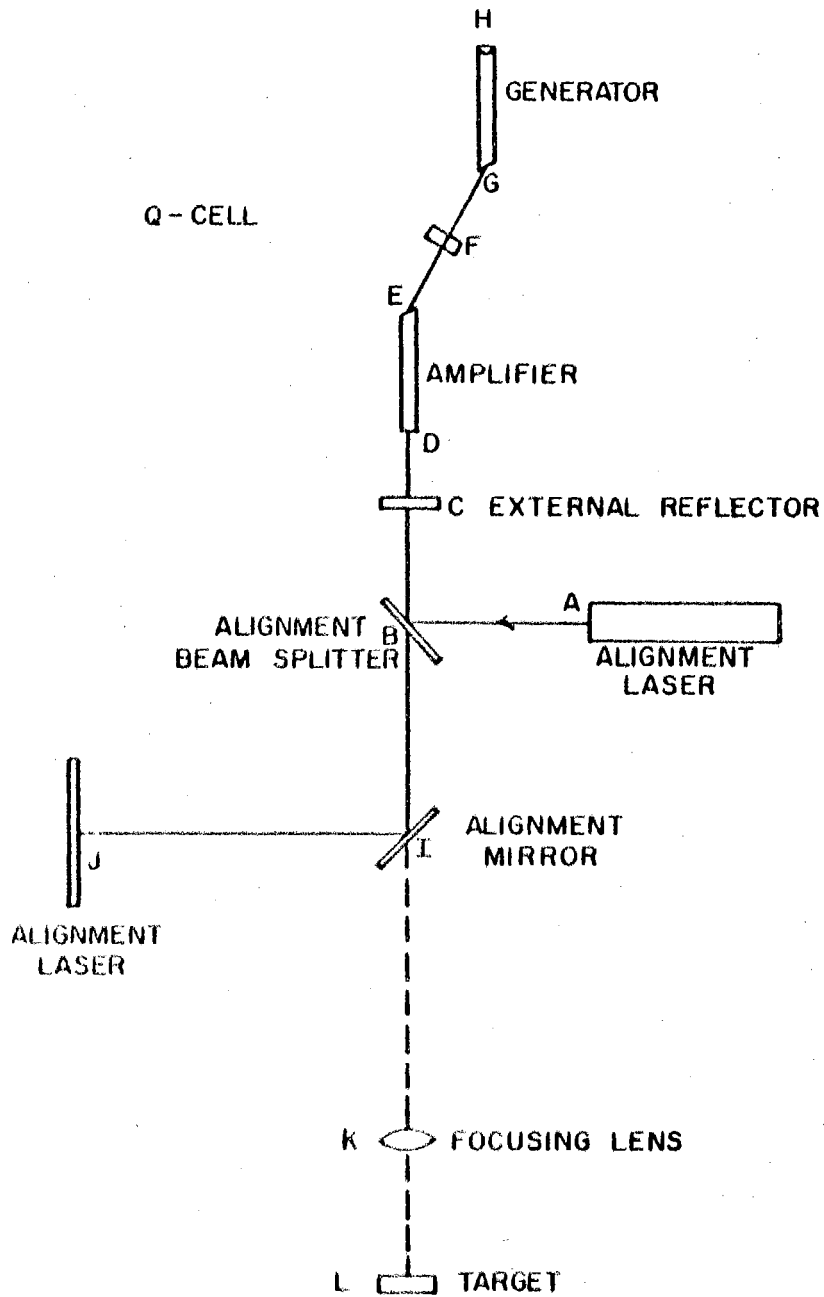


FIG. 27 ALIGNMENT OPTICS

1. With the Q-switch cell (F) and the external reflector (C) removed, the beam A-B-D is aligned perpendicular to and in the center of the bottom face of the amplifier rod. This is done by positioning the beam so that it is reflected back on itself. The adjustment is made with the alignment beam splitter (B) which has three degrees of linear motion and two degrees of angular motion. The alignment beam splitter is shown in Figure 28. Bringing the beam A-B-D back on itself guarantees that the beam is perpendicular to the ruby face at point D. Centering the beam guarantees that the beam will travel down the center axis of the cylindrical ruby rod. As a check, the beam emerging at point E should be centered on the Brewster face. Part of the reflected beam D-B-A will pass through the alignment beam splitter (B) and will be reflected by the alignment mirror (I) over to the ground glass screen (J). The dot on the screen is a result of the beam A-B-D-C-I-J and will be called the primary alignment point  $P_1$ .

2. The generator rod is positioned so that the beam A-B-D-E-G-H enters the Brewster face of the generator rod (G) in the center and is reflected at the center of the TIR prism (H). This beam when reflected at H will follow the path H-G-E-D-B-I-J and produce a dot  $P_2$ . The optical axis of both the generator rod and amplifier rod is aligned when  $P_1$  and  $P_2$  are coincident.

3. The Q-switch cell (F) is then placed into position between the generator and amplifier. A portion of the beam A-B-D-E-F is reflected by the Q-switch cell (F) and follows the path F-E-D-B-I-J producing a dot  $P_3$  on the ground glass screen. The Q-switch cell is then adjusted so that  $P_1$  and  $P_3$  are coincident. This insures that the face of the Q-switch cell is perpendicular to the optical axis of the laser rods.

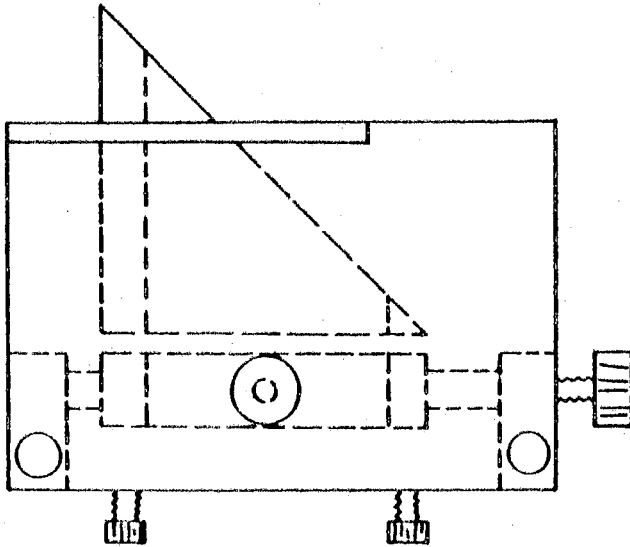
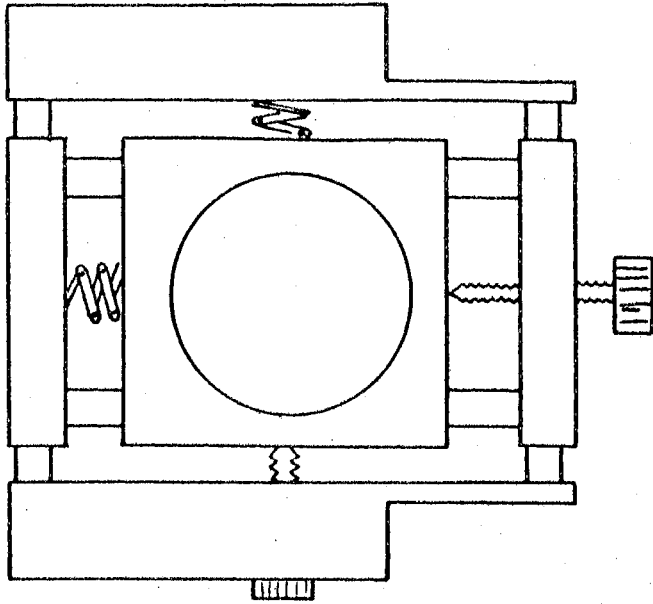


FIG. 28 ALIGNMENT BEAM SPLITTER

4. The external reflector (C) is placed into position and adjusted so that the beam A-B-C is partially reflected along the path C-B-I-J. At point J the reflected beam produces a dot  $P_4$ . The external reflector is perpendicular to optical axis of the laser when points  $P_1$  and  $P_4$  are coincident.

5. Alignment mirror (I) is removed and the beam A-B-C-D-C-B-I-I-L is focused with the focusing lens (K) on the target (L). After the above five steps are completed the laser optics are aligned. The precision achieved during alignment will now be discussed in the following paragraphs.

Since all of the optical components are aligned with respect to the amplifier rod, it is important to calculate first how well beam A-B-C-D can be aligned to the amplifier rod. The beam A-B-C-D and the reflected beam D-C-B-A can be made to coincide at point A to within .015". The length of the beam A-B-C-D is 23". The perpendicularity is then shown in Equation 28.

$$\begin{aligned}\theta(D) &= \frac{s}{r} = \frac{.015''}{23''} \\ \theta(D) &= .65 \text{ mrod.}\end{aligned}\tag{28}$$

The calculations for angular alignment of the generator rod to the amplifier rod is given below in Equation 29 assuming that  $P_1$  and  $P_2$  can be aligned to within .015" and that the distance of the path H-G-D-I-J is 270". This calculation is given as

$$\begin{aligned}\theta(H) &= \frac{s}{r} = \frac{.015''}{270''} \\ \theta(H) &= .055 \text{ mrod.}\end{aligned}\tag{29}$$

Assuming that  $P_1$  and  $P_3$  can be aligned to within  $.015''$  and that the distance of the path F-E-D-I-J is  $260'$ , the angular alignment of the Q-switch can be made to within the tolerance shown in the following calculation,

$$\theta(F) = \frac{s}{r} = \frac{.015''}{260''}$$

$$\theta(F) = .057 \text{ mrod.} \quad (30)$$

The optical alignment of the external reflector can be calculated in a similar manner assuming that  $P_1$  and  $P_4$  can be made to coincide to within  $.015''$  and that the path length C-I-J is given as  $248''$ . This calculation gives,

$$\theta(C) = \frac{s}{r} = \frac{.015''}{248''}$$

$$\theta(C) = .061 \text{ mrod.} \quad (31)$$

The only criteria for alignment of the focusing lens is that the target to lens distance be equal to the focal length of the lens, that the beam pass approximately through the center of the lens and that the lens to approximately perpendicular to the beam.

Although the generally excepted way to align ruby lasers and their optical components is through the use of a He-Ne gas laser, the author wishes to make a note of the error involved. The inherent error found in using a He-Ne gas laser for alignment purposes is due to the difference in index of refraction of the optical components for the  $6328 \text{ \AA}^{\circ}$  light emitted from the He-Ne laser and the  $6943 \text{ \AA}^{\circ}$  light emitted from the ruby laser. In the wavelength region between  $6943 \text{ \AA}^{\circ}$  and  $6328 \text{ \AA}^{\circ}$ , index for pink ruby is calculated from Levine (28) to be,



$$-\frac{\Delta n}{\Delta \lambda} \cong 3.7 \times 10^{-6}. \quad (32)$$

The change in index of refraction of quartz for this same region is given by Jenkins and White (29) to be,

$$-\frac{\Delta n}{\Delta \lambda} \cong 2.7 \times 10^{-6}. \quad (33)$$

Given the index of refraction of light at a wavelength of 6943 Å in ruby to be 1.7637, the index of refraction of light at a wavelength of 6328 Å can be calculated from Equation (32) in the following manner,

$$\begin{aligned} -\frac{\Delta n}{\Delta \lambda} &\cong 3.7 \times 10^{-6} \\ \Delta n &\cong -3.7 \times 10^{-6} (\Delta \lambda) \\ n_{6943} - n_{6328} &\cong -3.7 \times 10^{-6} (6943 - 6328) \\ 1.7640 - n_{6328} &\cong -3.7 \times 10^{-6} (615) \\ -n_{6328} &\cong -1.7637 - .0023 \\ n_{6328} &\cong 1.7660 \end{aligned} \quad (34)$$

Similarly, the index of refraction in quartz for light at a wavelength of 6943 Å is given as 1.4613. The index of refraction in quartz for light at a wavelength of 6328 Å is given by Equation (33) to be,

$$\begin{aligned} -\frac{\Delta n}{\Delta \lambda} &\cong 2.7 \times 10^{-6} \\ \Delta n &\cong -2.7 \times 10^{-6} (\Delta \lambda) \\ n_{6943} - n_{6328} &\cong -2.7 \times 10^{-6} (6943 - 6328) \end{aligned}$$

$$\begin{aligned}
 1.4613 - n_{6328} &\cong - 2.7 \times 10^{-6} \quad (615) \\
 - n_{6328} &\cong - 1.4613 - .0017 \\
 n_{6328} &\cong 1.4630 \quad (35)
 \end{aligned}$$

The optical components effected by the alignment error due to the difference in refractive index are the generator rod, Q-switch cell and the focusing lens. Figure 29 shows an exaggerated view of the 6943 Å light path and 6328 Å light path between the amplifier rod and generator rod.

In order to minimize transmission losses between the generator and amplifier rods the bottom end of the generator rod and the top end of the amplifier rod is cut at Brewster's angle. According to Brewster's law this angle is given as

$$\begin{aligned}
 \tan \alpha(2) &= n_{6943} \\
 \alpha(2) &= \arctan n_{6943} \\
 \alpha(2) &= \arctan (1.7640) \\
 \alpha(2) &= 60^{\circ} 27' \quad (36)
 \end{aligned}$$

where  $\alpha(2)$  is Brewster's angle and  $n_{6943}$  is the index of refraction of ruby for 6943 Å light. The angular relationships for the Brewster angle are shown in Figure 30.

Referring to Figure 29, it is seen that the alignment beam from the gas laser strikes point E (1) at an angle of  $29^{\circ} 33'$  from the normal. The angle of refraction for this beam is given by Snell's law as:

$$\begin{aligned}
 \sin \alpha(1) &= n_{6328} \sin \alpha(3) \\
 \sin \alpha(1) &= 1.7660 \sin 29^{\circ} 33'
 \end{aligned}$$

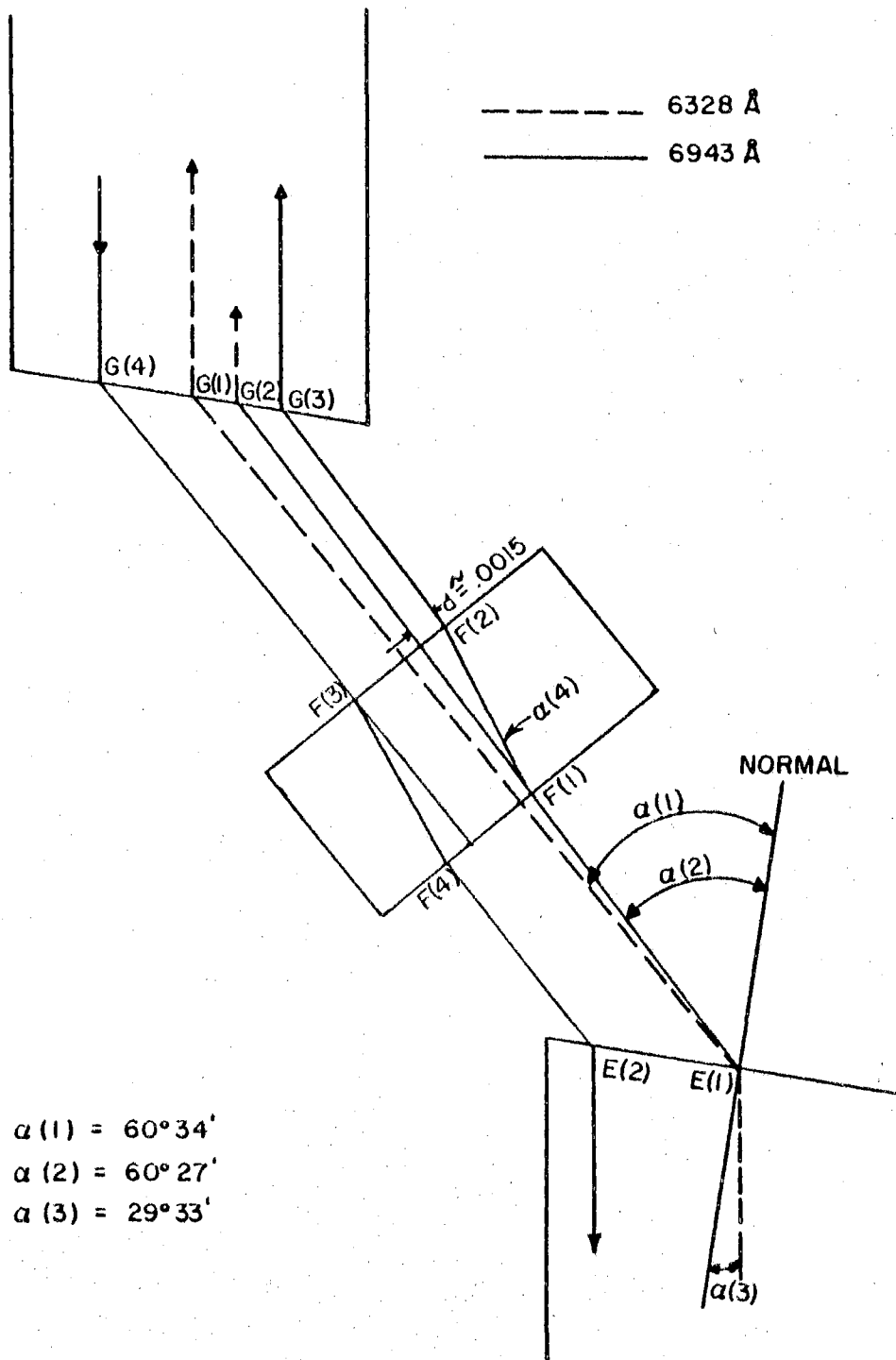


FIG. 29 OPTICAL PATHS ALIGNMENT BEAM AND RUBY LASER BEAM

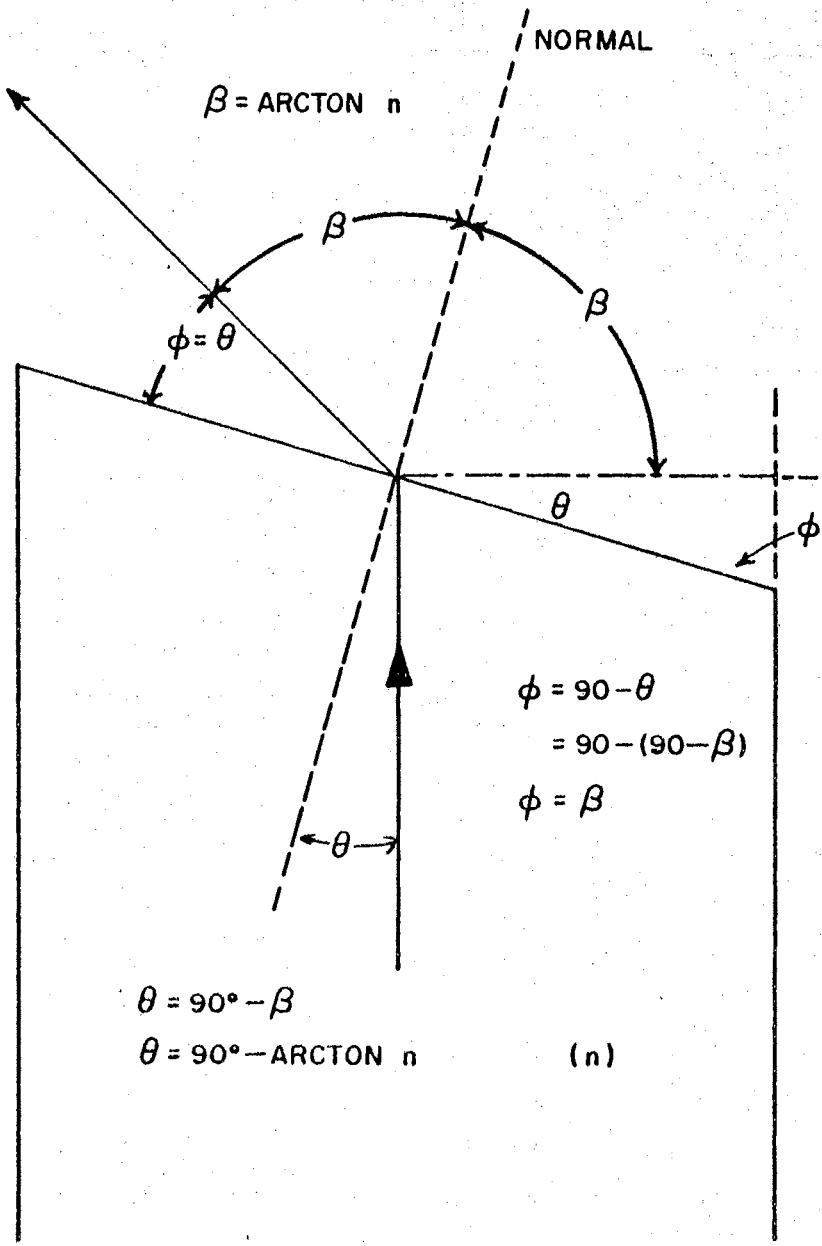


FIG. 30 ANGULAR RELATIONSHIPS OF BREWSTER'S ANGLE

$$\begin{aligned}
 \sin \alpha(1) &= 1.7660 (.4932) \\
 \sin \alpha(1) &= .8710 \\
 \alpha(1) &= 60^{\circ} 34' \quad (37)
 \end{aligned}$$

where  $\alpha(1)$  is the angle of refraction for the 6328 Å light and  $n_{6328}$  is the refractive index of ruby for this particular wavelength. By comparing Equation (36) and (37), the angular dispersion of the two beams is seen to be approximately 7 min. of arc. With the Q-switch cell not in the optical path, the arc length would be given as,

$$\begin{aligned}
 s &= r [\alpha(1) - \alpha(2)] \\
 s &= 4.0'' [2.1 \times 10^{-3} \text{ rad.}] \\
 s &= 8.4 \times 10^{-3} \text{ in.} \quad (38)
 \end{aligned}$$

where  $r$  is the center line distance between the ruby rods and  $[\alpha(1) - \alpha(2)]$  is the difference in the angle of refraction for the two light rays, given above in radians. Trigonometric relations exist so that the distance from point G(1) to point G(2) can be approximated as shown in Figure 31. This horizontal displacement is calculated to be approximately .017 inches. With the Q-switch cell in place, the beam from E(1) to G(2) is displaced along the path E(1) - F(1) - F(2) - G(3). This displacement is given by the following equation as,

$$\begin{aligned}
 d &= t \sin [\alpha(1) - \alpha(2)] \left\{ 1 - \frac{\cos [\alpha(1) - \alpha(2)]}{n_{6943} \alpha(4)} \right\} \\
 d &= .5 (.002) \left[ 1 - \frac{.002}{1.4640(1)} \right] \\
 d &= 1.0 \times 10^{-3} [1 - .0018] \\
 d &\approx .001 \text{ inches.} \quad (39)
 \end{aligned}$$

$$s \approx 8.4 \times 10^{-3} \text{ in.}$$

$$\theta = \alpha(3) = 29^\circ 33'$$

$$y \approx s / \sin \theta$$

$$y \approx .017 \text{ in.}$$

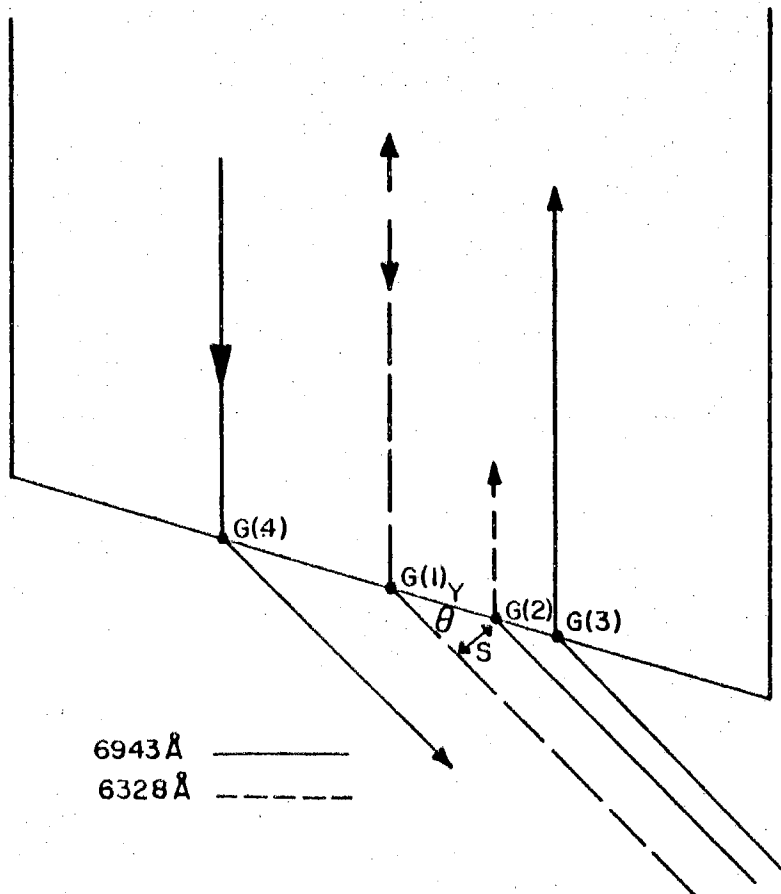


FIG. 31 APPROXIMATE HORIZONTAL DISPLACEMENT  
OF RUBY LASER BEAM RELATIVE TO  
ALIGNMENT BEAM

where  $d$  is the beam displacement,  $t$  is the thickness of the Q-switch cell,  $[\alpha(1) - \alpha(2)]$  is the angular dispersion of the two beams, and  $\alpha(4)$  is the internal angle of refraction of the  $6943 \text{ \AA}$  beam as it enters the Q-switch cell. The total displacement along the ruby face is approximately .018 inches from the center axis of the ruby. The  $6943 \text{ \AA}$  beam entering the top ruby is reflected by the TIR prism and emerges at point G(4), .018 inches on the opposite side of the ruby axis. The beam then continues on and enters the amplifier ruby at point E(2), .036 inches from the optical axis. Once the alignment error is calculated, the generator rod can be offset from the alignment beam so the maximum displacement of  $6943 \text{ \AA}$  beam in the amplifier rod is only .006 inches. This error is considered small compared to the radius of the rods. In a similar manner the Q-switch cell can be offset so that the angular alignment is within .1 mrad. of the optical axis of the laser. For plasma production, the effect of the difference in focal point of the lens due to the difference in wavelength is negligible. Table VI shows the possible alignment error of the optical components relative to the  $6328 \text{ \AA}$  alignment beam. Table VII shows the possible alignment error of the optical components due to the difference in index of refraction. Table VIII shows the maximum possible alignment error of the optical components with respect to the geometrical axis of the amplifier. In concluding this section, the author wishes to state that the modified alignment procedure has worked very well and is a relatively simple way to achieve laser alignment.

As stated earlier, a passive saturatable liquid Q-switch is used during Q-switched operation of the twin ruby laser. The Q-switching liquid originally used by Peery was a solution of nitrobenzene dissolved

TABLE VI

POSSIBLE ALIGNMENT ERROR OF THE OPTICAL COMPONENTS  
RELATIVE TO THE 6328 Å ALIGNMENT BEAM

Component	Max. Angular Error (mrad)	Max. Linear Error (in.)
Amplifier rod	.65	.015
Generator rod	.055	.015
Q-switch	.057	----
External reflector	.061	----

TABLE VII

POSSIBLE ALIGNMENT ERROR OF THE OPTICAL COMPONENTS  
DUE TO THE DIFFERENCE IN INDEX OF REFRACTION

Component	Max. Angular Error (mrad)	Max. Linear Error (in.)
Amplifier rod	----	----
Generator rod	----	----
Q-switch	.100*	----
External reflector	----	----

\* After correction.

TABLE VIII

MAXIMUM POSSIBLE ALIGNMENT ERROR OF THE OPTICAL COMPONENTS  
WITH RESPECT TO THE GEOMETRIC AXIS OF THE AMPLIFIER ROD

Component	Max. Angular Error (mrad)	Max. Linear Error (in.)
Amplifier rod	----	----
Generator rod	.71	.036
Q-switch	.81	----
External reflector	.71	----



in methyl alcohol. Due to the poisonous nature of nitrobenzene the Q-switching liquid was changed to a solution of cryptocyanine in methyl alcohol. The bleaching process in the cryptocyanine solution is reversed after each giant pulse, thus allowing the solution to be used for many shots. The absorption cross section of cryptocyanine for ruby laser radiation at  $6943 \text{ \AA}$  is  $8.1 \times 10^{-16} \text{ cm}^2$  per molecule. The solution absorbs radiation in a narrow band approximately  $370 \text{ \AA}$  (FWHM) with the peak absorption at  $7040 \text{ \AA}$ . A transmission curve for cryptocyanine in methyl alcohol is shown in Figure 32.

Since the speed of the Q-switch depends on the percent absorption of the Q-switch, it is important to obtain the proper concentration of cryptocyanine. In order to obtain the proper concentration of cryptocyanine, a 50 percent absorbing solution was placed in the Q-cell. The laser was then fired and the output monitored. The absorption of the cell was increased slightly by increasing the concentration of cryptocyanine. The laser was fired again and the output monitored. This process was continued until the shortest Q-switching time was obtained. The cell was then placed on a spectrophotometer and the percent absorption of the Q-switch liquid was measured. The shortest Q-switching time occurred when the concentration of cryptocyanine produced an absorption of 71 percent in the no-pass mode. It was interesting to note that when the Q-cell was filled only with methyl alcohol there was multiple spiking similar to operation of the laser in the normal mode. As the concentration of cryptocyanine was increased the number of spikes decrease, the pulse amplitudes increased and the pulse durations decreased. At about 65 percent absorption the output was observed to consist of a single pulse with a pulse width of about 150 nsec. At 71 percent absorp-

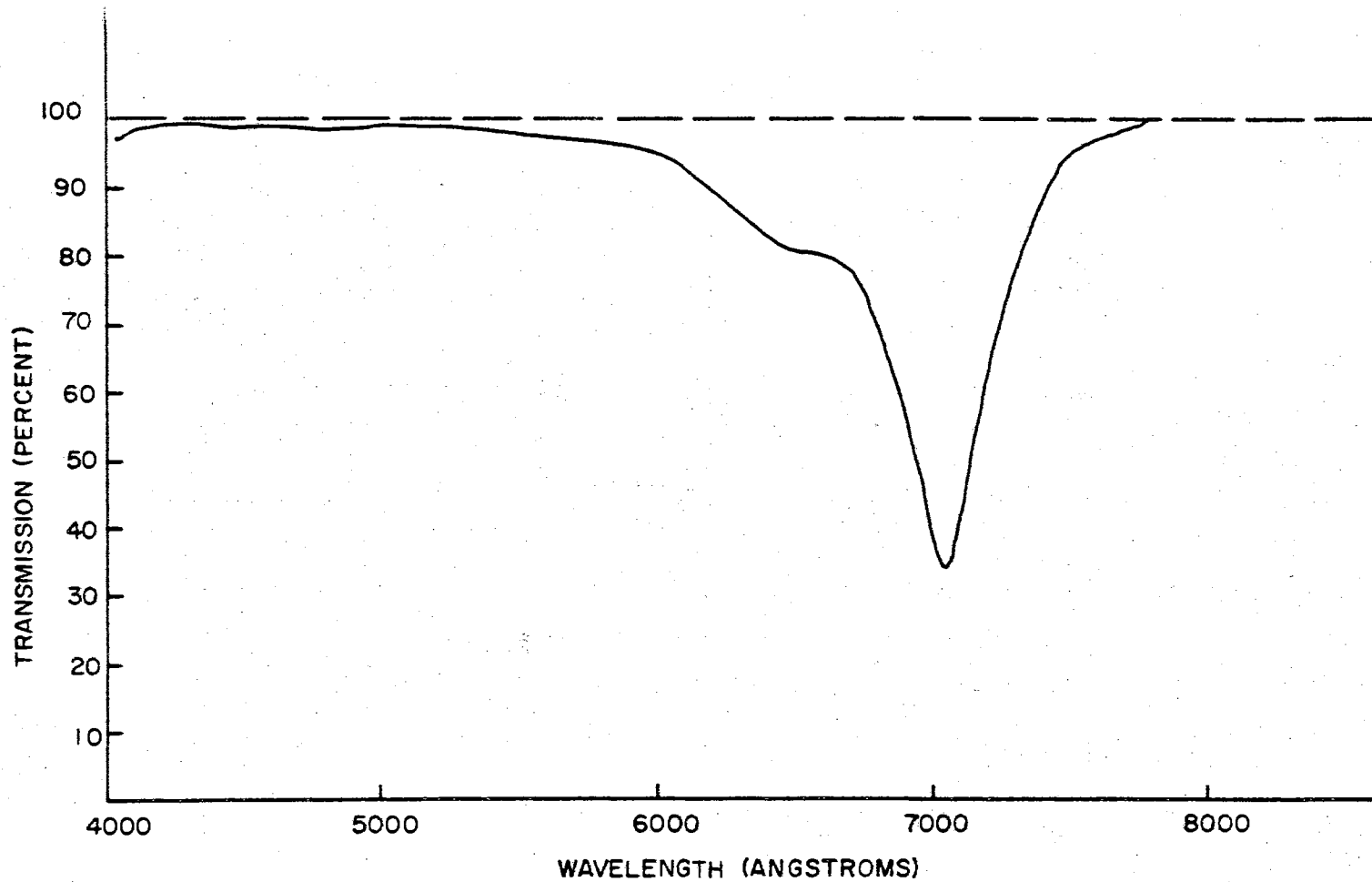


FIG. 32 TRANSMISSION CURVE FOR CRYPTOCYANINE IN METHYL ALCOHOL

tion the pulse width decreased to approximately 30 nsec. Although pulse widths of 10 nsec. have been reported for single rod lasers using a cryptocyanine solution, the author believes that the 30 nsec. pulse obtained from the twin ruby laser described in this work was due to self excitation in the long cavity. The only problem encountered with the cryptocyanine-methyl alcohol solution was that of evaporation changing the concentration of the Q-switch solution. Time permitting, this problem could have been overcome with a redesigned Q-cell.

### Electrical

This section will deal with electrical modifications and mechanical modification that were made as a result of electrical problems. A general schematic of the entire system is shown in Figure 33.

One of the first modifications made by the author was to redesign the flashtube mounting. The flashtubes used on the twin ruby laser for optical pumping of the rubies were helical Xenon flashtubes built by Kemlite. The original mounting is shown in Figure 34. With the flashtubes mounted as shown in Figure 34, the flashtubes would spontaneously fire at around 7 K.V., whereas the self fire level reported by the manufacturer was between 12 K.V. and 15 K.V. After extensive testing it was found that at 7 K.V. the flashtubes were breaking down between the anode and the metal reflector. This problem was eliminated by enlarging the flashtube feedthrough holes in the reflector and inserting a cylinder of insulation as shown in Figure 35. Teflon was originally used for the insulation. It was quickly found, however, that the teflon decomposed due to the radiation from the flashtubes. Delrin was then used for insulation and it worked very well with no visual deterioration.

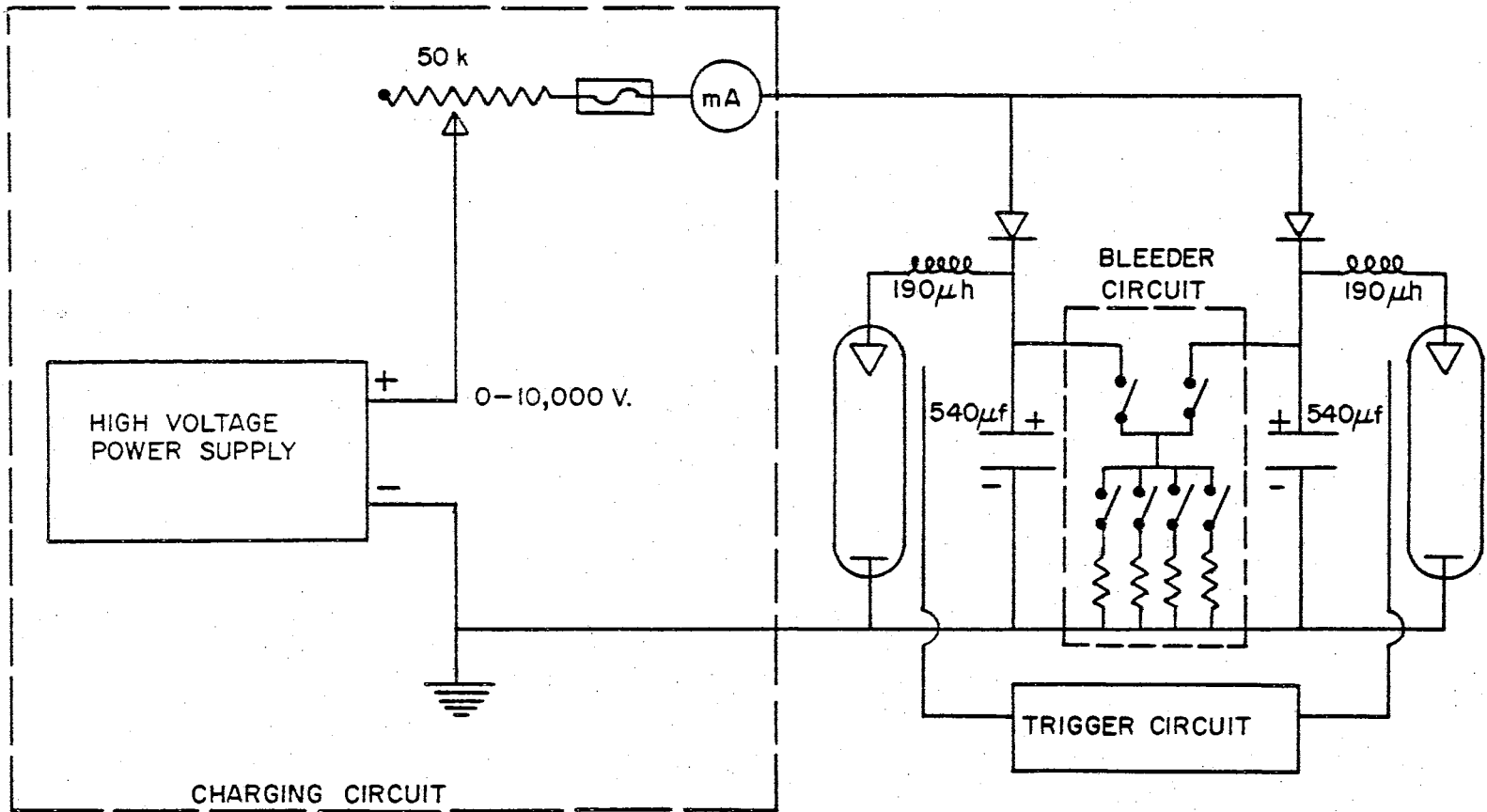


FIG. 33 SCHEMATIC OF LASER ELECTRICAL SYSTEM

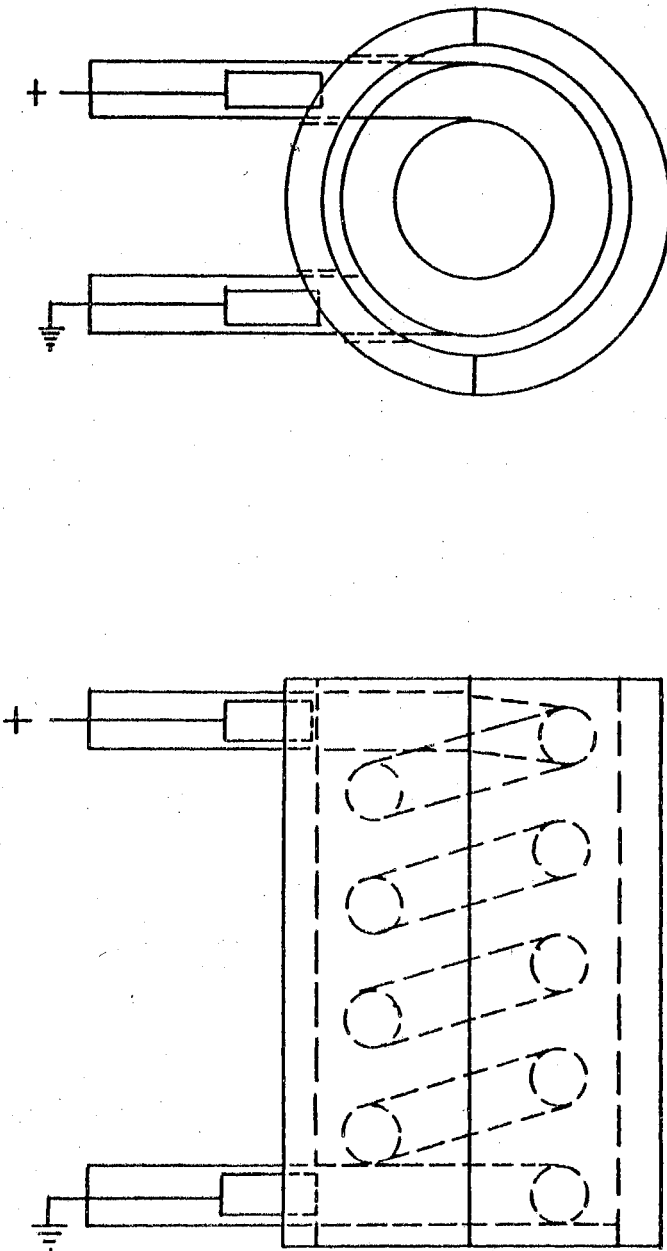


FIG. 34 FLASHTUBE MOUNTED IN PUMPING CAVITY

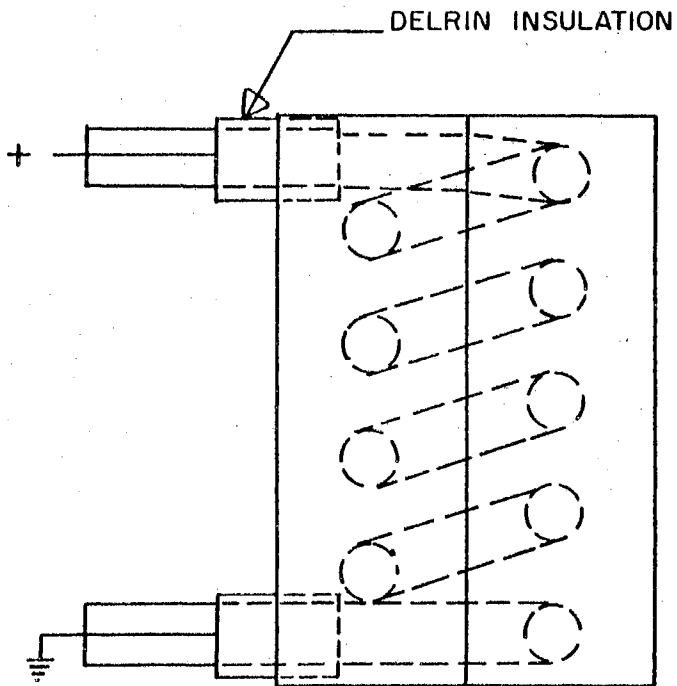
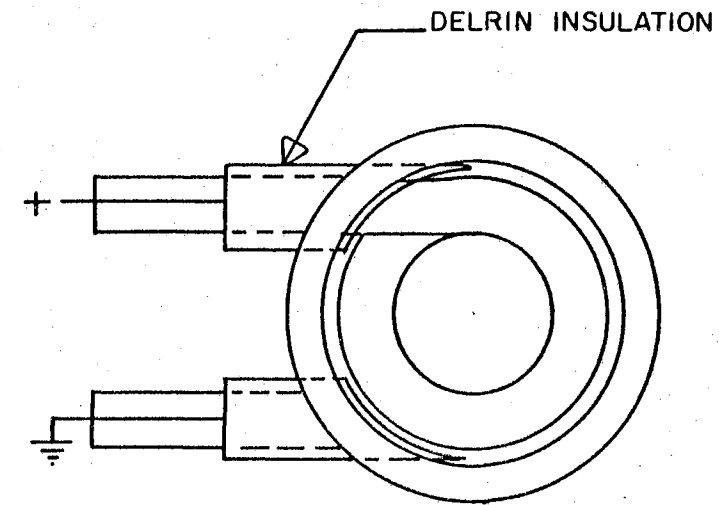


FIG. 35 DELTRIN INSULATION ON MODIFIED PUMPING CAVITY

Another problem encountered with the flashtubes was that of triggering both tubes simultaneously with a high degree of reliability. A schematic of the original triggering circuit is shown in Figure 36. As seen in the schematic, the primary of both trigger transformers are in parallel. With this type of arrangement it is conceivable that a trigger pulse from one transformer may travel through the flashtube to ground before the trigger pulse from the other transformer reaches ground. If this occurs, then the primary of the "grounded" transformer will assume most of the current from the trigger capacitor resulting in an extremely weak trigger pulse for the other flashtube. This problem coupled with the high failure rate of the original trigger transformers lead to a complete redesign of the trigger circuit. In redesigning the trigger circuit, the author used two automotive type trigger transformers because of reliability, higher secondary voltage and lower cost. The new trigger circuit is shown in Figure 37. An oscilloscope tracing of trigger output is shown in Figure 38.

The power supply used to charge the laser capacitor banks was capable of putting out 10 kilo-volts d.c. at a current rating of 20 ma. Although this power supply is somewhat limited in its current rating, it was readily available for use and worked very reliably throughout the project. Because of the low current rating of the power supply it was necessary to modify the existing charging circuit in favor of a circuit which would give a shorter charging time. The original design used a fixed charging resistor of sufficient value to insure a maximum current drain from the power supply of 20 ma at 10 kilo-volts. This type of circuit is shown in Figure 39. The problem with this type of circuit is that the current output of the power supply drops as the charging volt-

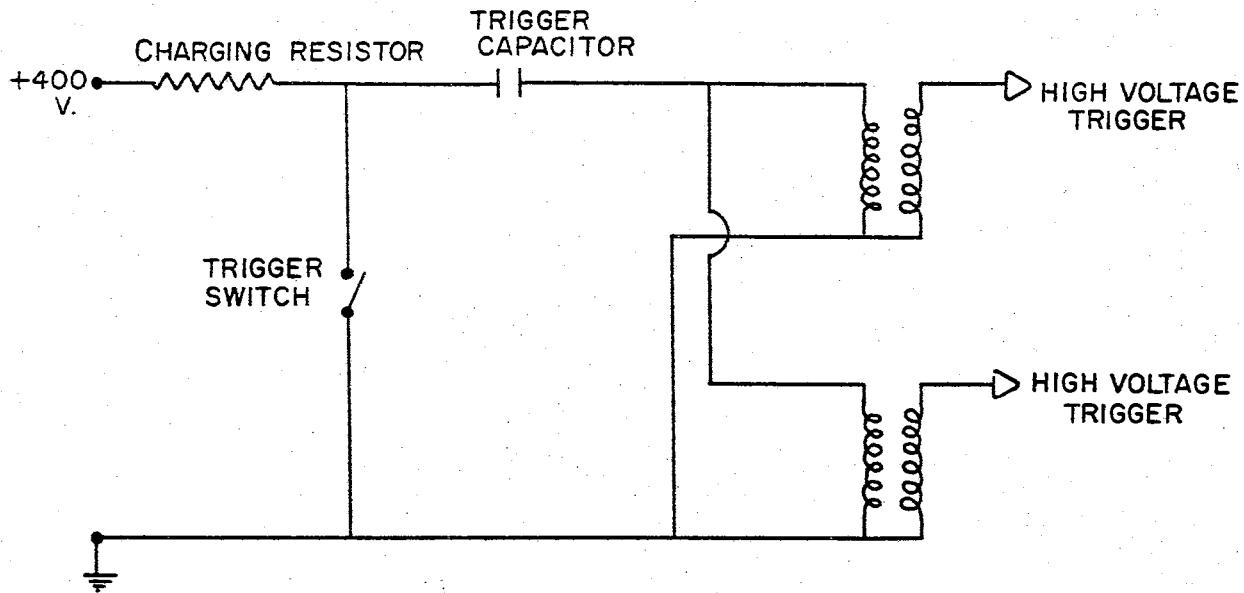


FIG. 36 SCHEMATIC OF ORIGINAL TRIGGER CIRCUIT



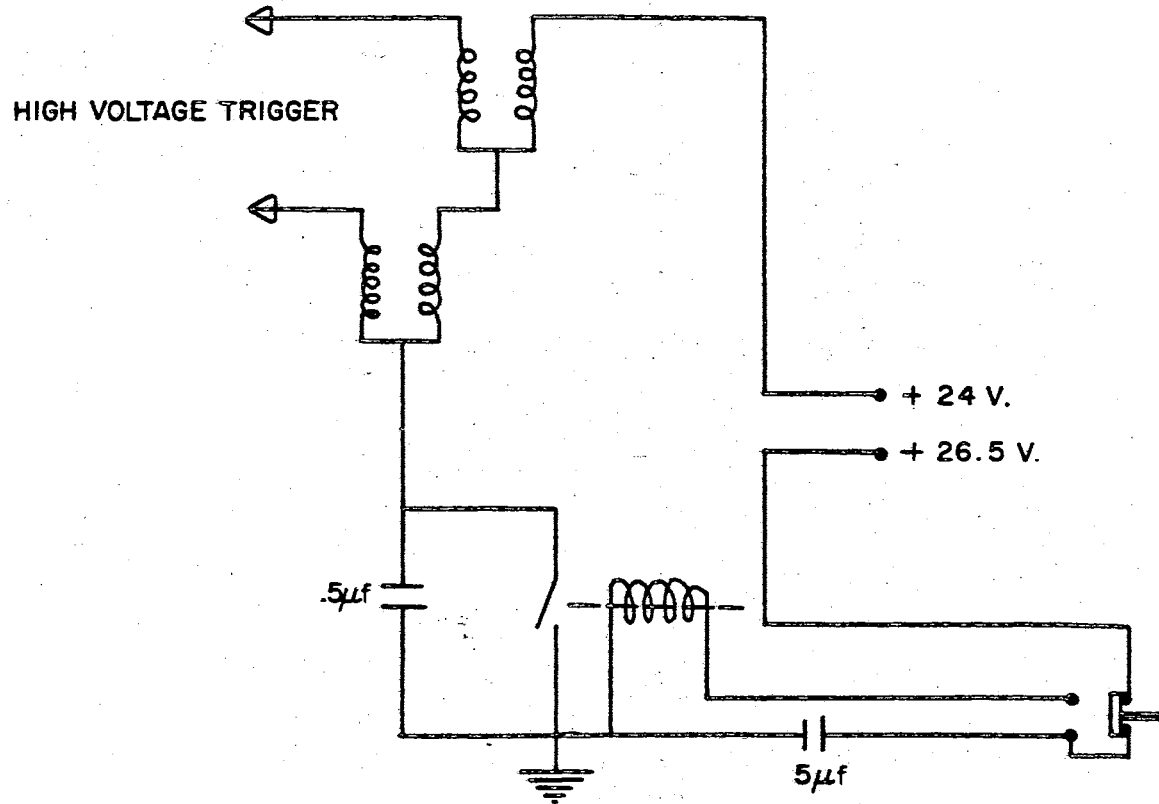


FIG. 37 MODIFIED TRIGGER CIRCUIT

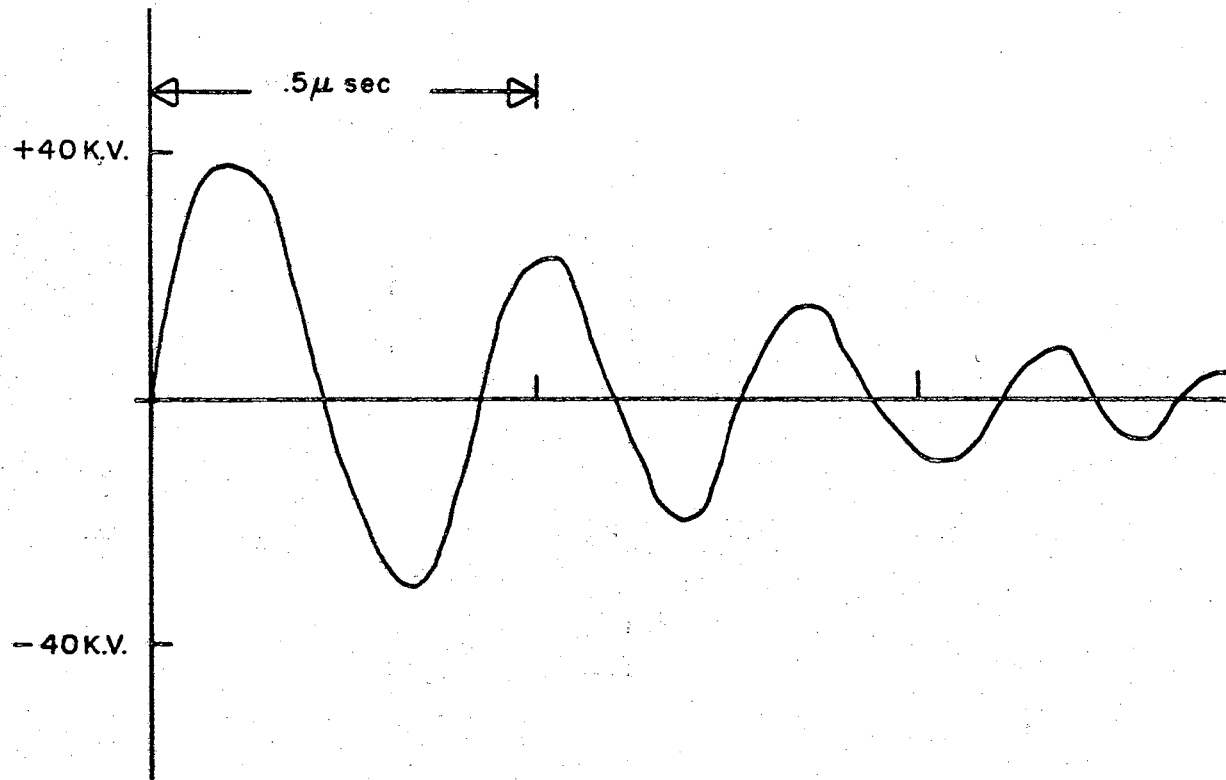


FIG. 38 HIGH VOLTAGE TRIGGER WAVEFORM

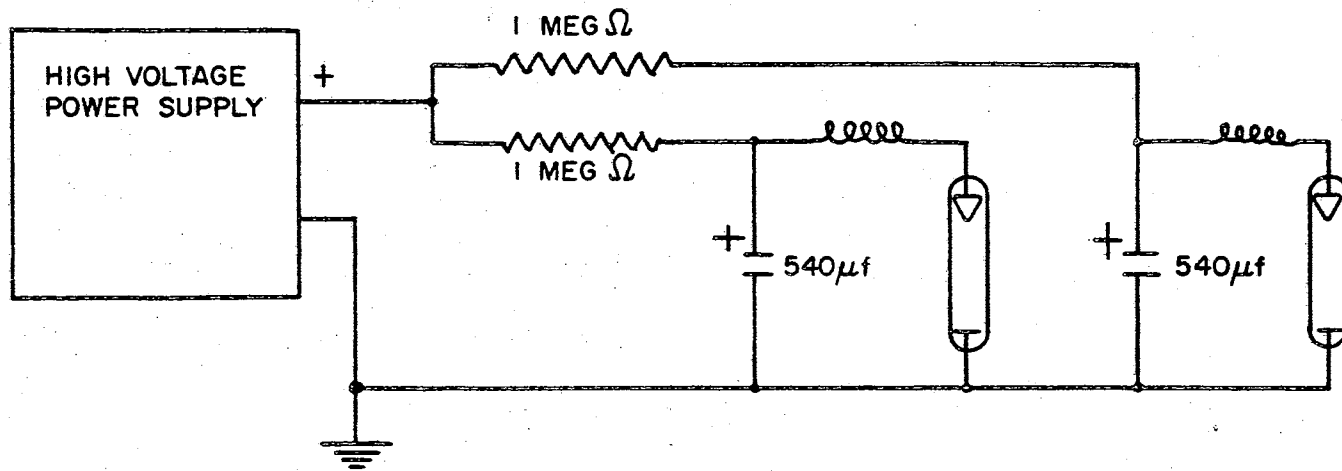


FIG. 39 ORIGINAL CHARGING CIRCUIT

age increases. The charge on the capacitor banks is given by

$$Q = C.V. (1 - e^{-t/RC}) \quad (40)$$

where  $Q$  is the charge on the capacitors,  $V_0$  is the charging voltage,  $t$  is the time,  $R$  is the charging resistance and  $C$  is the capacitance. The basic definition of current gives

$$I = \frac{dQ}{dt} \quad (41)$$

Combining Equations 40 and 41 gives the charging current as a function of time to be

$$\begin{aligned} I &= \frac{dQ}{dt} = \frac{d}{dt} [C V_0 (1 - e^{-t/RC})] \\ I &= \frac{V_0}{R} e^{-t/RC} \end{aligned} \quad (42)$$

Figure 40 shows Equation 42 plotted for an equivalent capacitive load of 1080  $\mu\text{f}$ , an equivalent charging resistor of 500  $\text{k}\Omega$  and a charging voltage of 10 KV. It can be shown from Equation 42 that after a time  $t = 4RC$ , the capacitors are charged to 98 percent of the final value. Thus, the approximate time to charge the capacitor banks is given as

$$\begin{aligned} t &= 4RC = 4 (500 \times 10^3)(1080 \times 10^{-6} \text{ f}) \\ t &= 2160 \text{ sec} = 36 \text{ min.} \end{aligned} \quad (43)$$

As seen from Equation 43, it took an extremely long time to charge the capacitor banks before the charging circuit was modified.

The modified charging circuit is shown in Figure 41. The charging resistor actually consist of ten 50  $\text{k}\Omega$  resistors mounted on a rotary switch. By decreasing the charging resistance as the charge on the

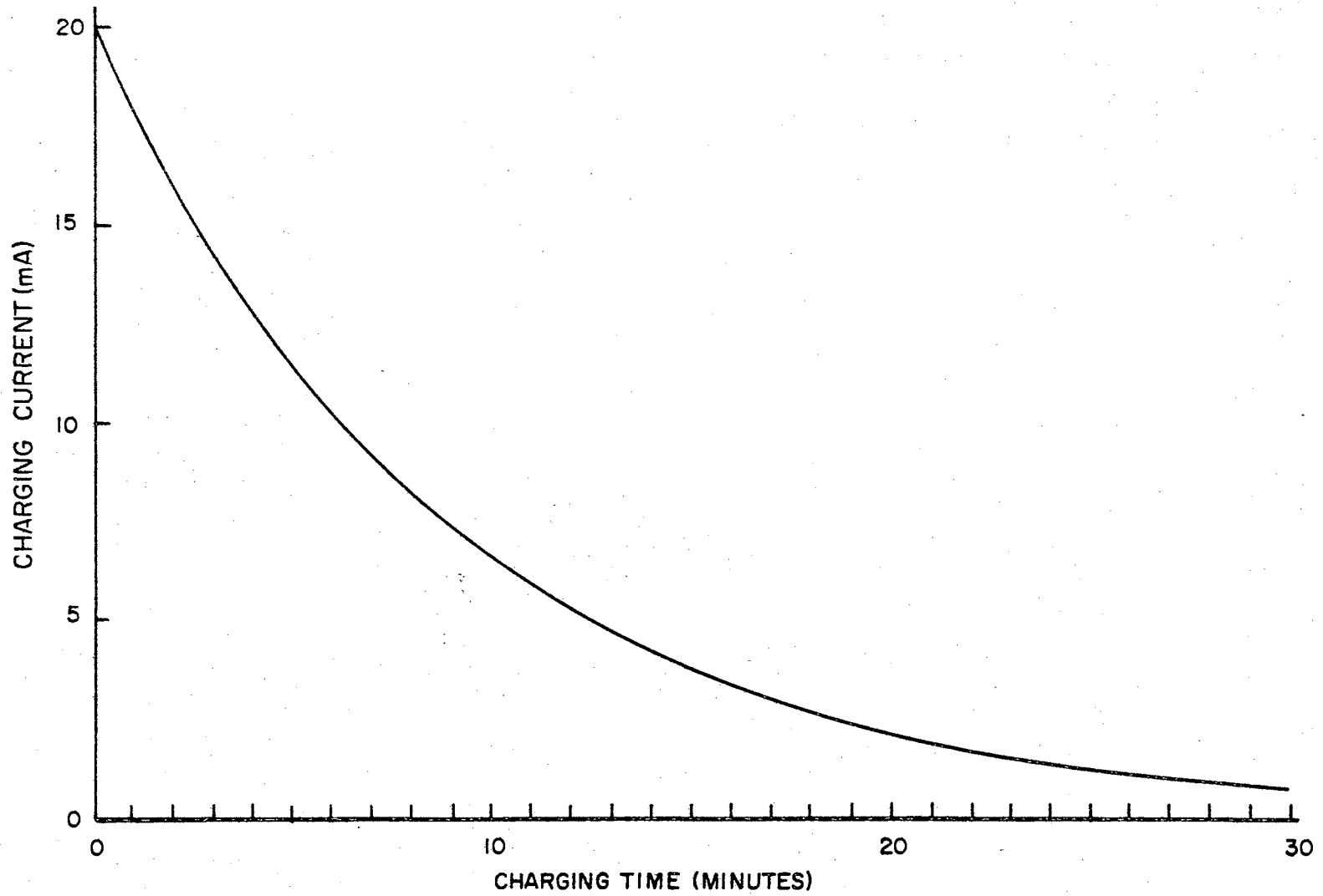


FIG. 40 CHARGING CURVE WITH CONSTANT CHARGING RESISTOR

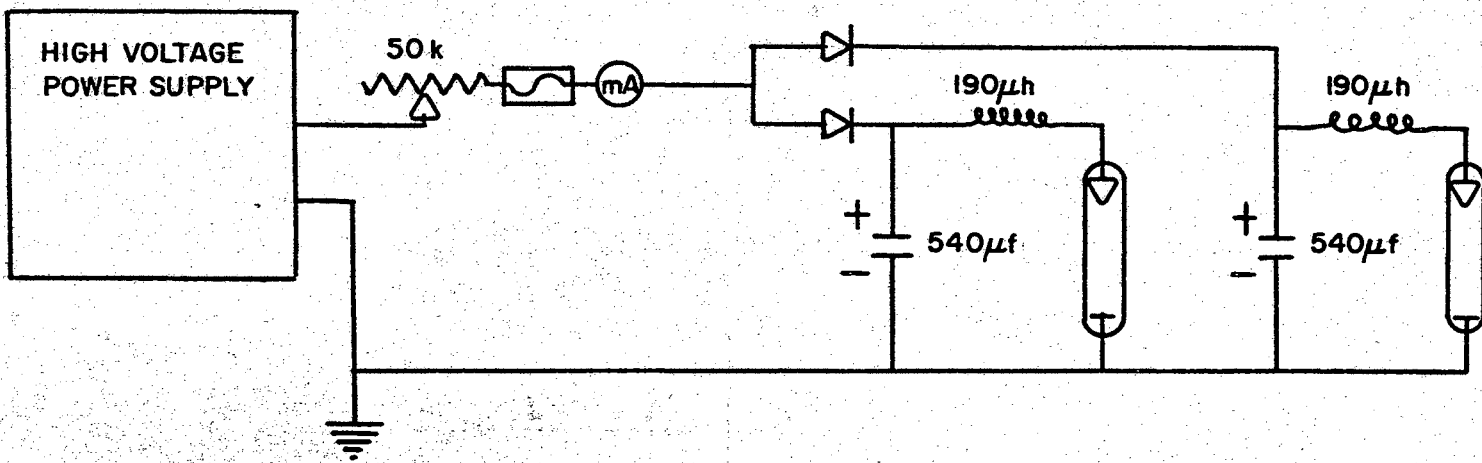


FIG. 41 MODIFIED CHARGING CIRCUIT

capacitor increased, the charging current can be kept fairly constant. Figure 42 shows the charging current as a function of time for a capacitive load of 1080  $\mu\text{f}$ . As seen from Figure 42, the average charging current for the modified circuit is approximately 19 ma. The net charge placed on the capacitor banks ( $Q = CV_0$ ) is 10.8 coul. The approximate charging time is then given as

$$t \approx \frac{\Delta Q}{\Delta I}$$

$$t \approx \frac{10.8 \text{ coul}}{19. \times 10^{-3} \text{ amps}} = .57 \times 10^3 \text{ sec}$$

$$t \approx 570 \text{ sec} = 9.5 \text{ min.} \quad (44)$$

Comparing Equation 43 and 44 shows that with the modified charging circuit, the charging time was cut from 36 min. to 9.5 min. Since both capacitor banks were charged through the same resistor, the banks were isolated from each other with high voltage silicon diodes. The diodes were Varo type 7715-10 rated at 10 KV, 25 ma. The diodes were placed in the charging circuit in the event that one capacitor bank discharged leaving the other bank charged. A 20 ma. fuse was also added to the charging circuit to protect the power supply.

Once the capacitor banks are charged, they may be quickly discharged, without triggering the flashlamps, by using the discharge resistor circuit as shown in Figure 43. The circuit was designed so that either bank or both banks could be discharged. Closing the grounded switch also eliminates charge accumulation when the laser is not in use.

Another problem encountered with the initial design was that of tremendous acoustical shock when the flashtube was first fired. Due to the fast rise time of the current pulse through the tube, the Xenon

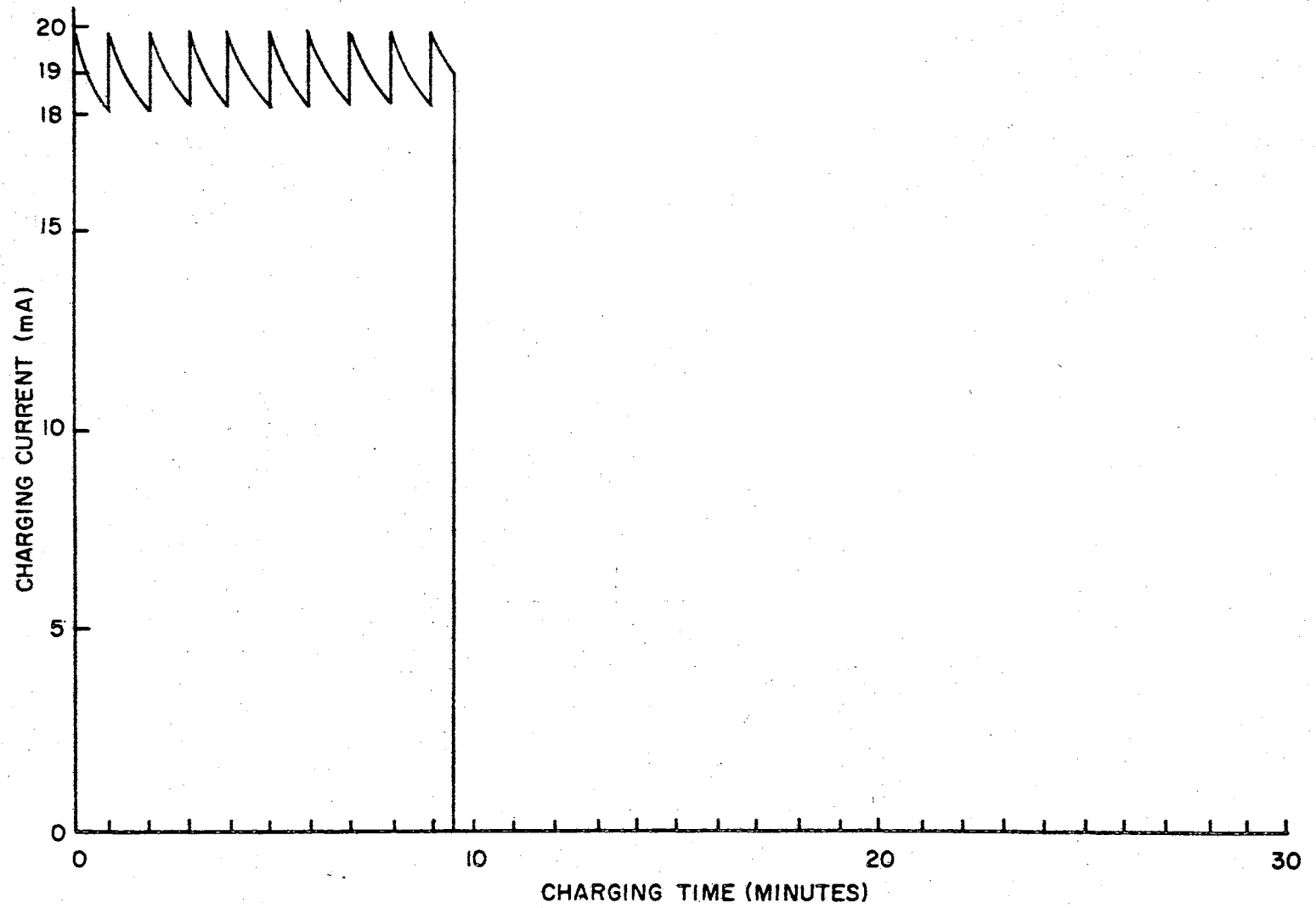


FIG. 42 CHARGING CURVE WITH VARIABLE CHARGING RESISTOR



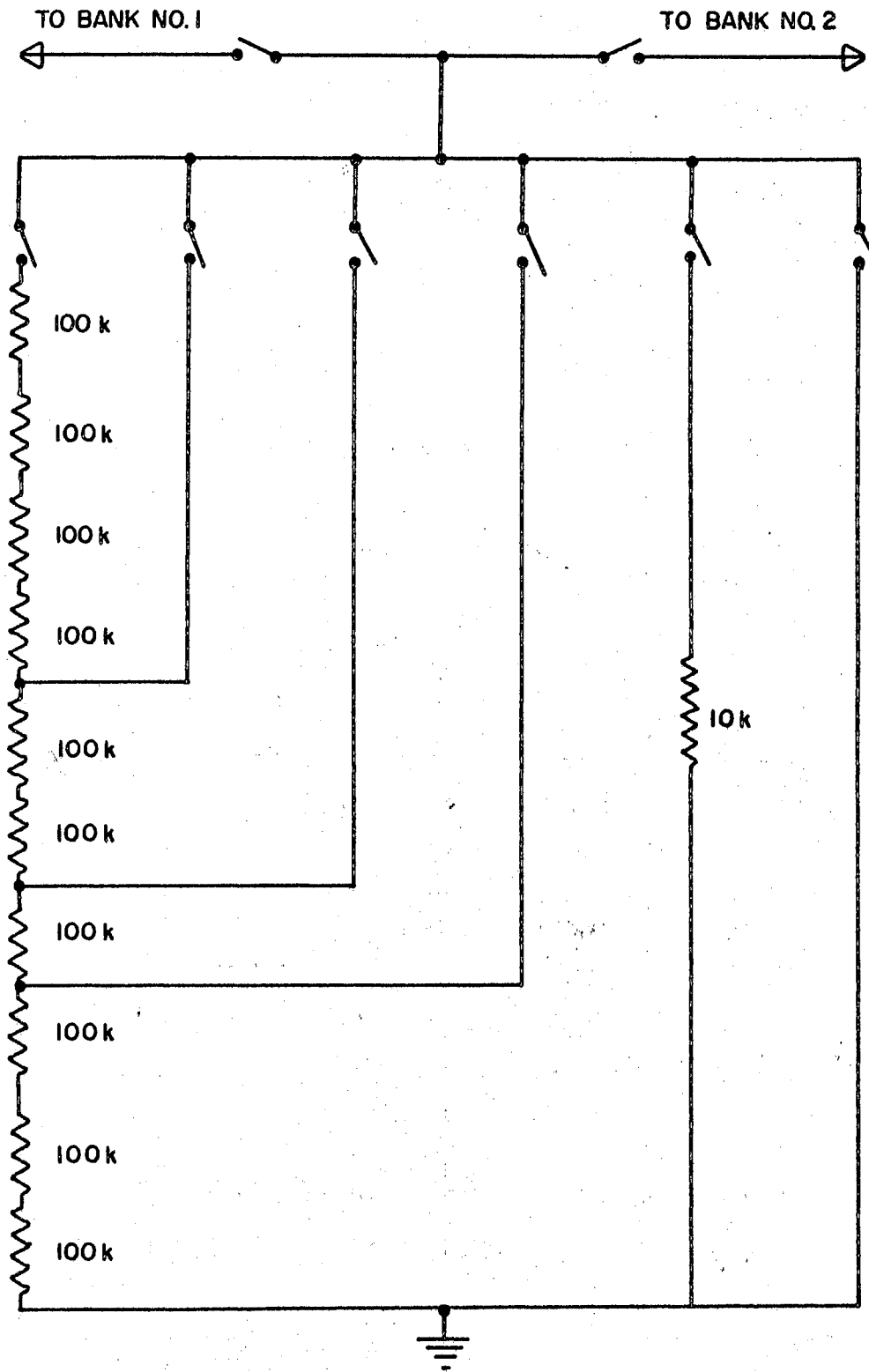


FIG. 43 CAPACITATOR BANK BLEEDER CIRCUIT

plasma expands rapidly causing an acoustical shock wave to be formed. To decrease the rise time of the current pulse, Peery inserted an inductor in the circuit between the capacitor bank and the flashtube. The type of inductor used by Peery is shown in Figure 44. This inductor was modified so that different values of inductance could be tapped off. The inductance at the various tap off points were measured by an inductance bridge. The modified inductor is shown in Figure 45.

### Vacuum

Because of the objectives involved, most of the experimental work described in this paper was done in vacuum. This section will describe the two different vacuum chambers used in the experimental work.

The first vacuum chamber designed by Peery was used for the target deformation experiment. The vacuum chamber was constructed of steel and was nickel plated to prevent corrosion. The vacuum chamber was pumped with a 6 inch oil diffusion pump, backed by a fore pump. The required vacuum of  $10^{-6}$  torr was easily obtained with this arrangement. The only difficulty encountered with this vacuum chamber was the proper positioning of the focusing lens with respect to the target. The steel vacuum chamber was modified slightly so that a new target could be placed at the laser beam focus without breaking vacuum each time. Figure 46 is a drawing of the steel vacuum chamber.

For the remainder of the experiment, a glass vacuum chamber was used. The glass chamber was designed with external laser focusing, rotatable target mount and multiple electrical feedthrough. The glass chamber accepted the plasma expansion velocity experiment, the quadrupole mass filter experiment and the vacuum ultraviolet spectrograph experi-

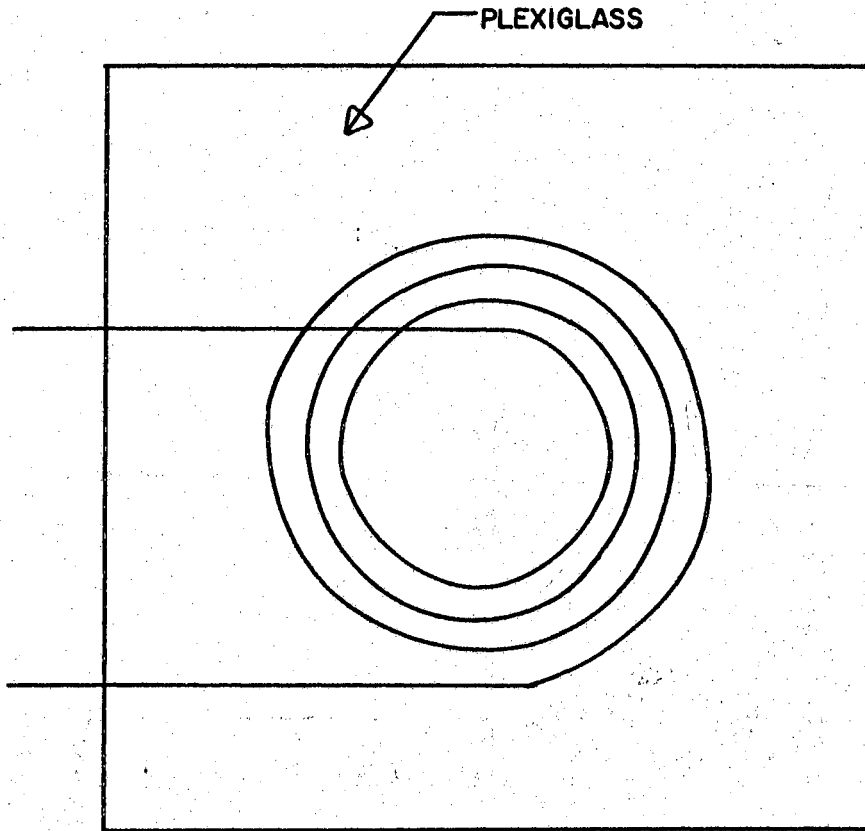


FIG.44 ORIGINAL DISCHARGE INDUCTOR

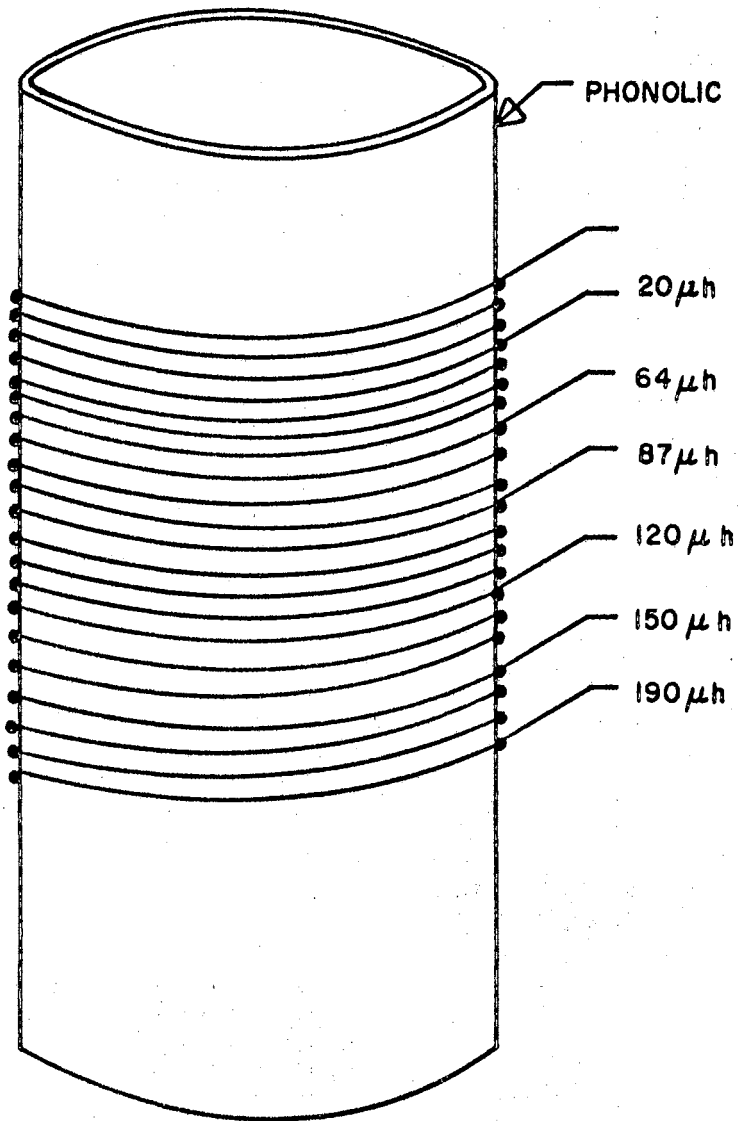


FIG. 45 MODIFIED DISCHARGE INDUCTOR

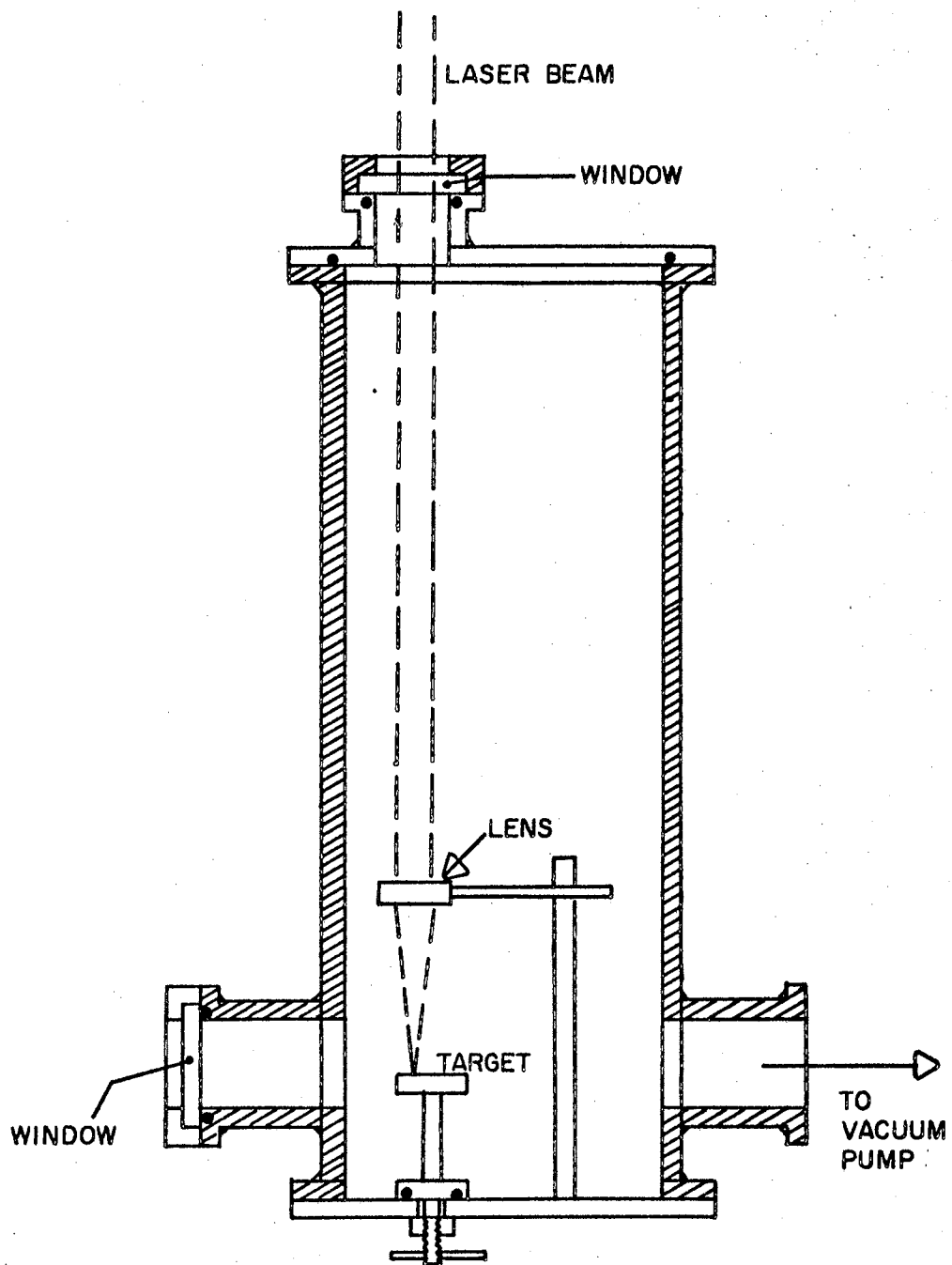


FIG. 46 METAL VACUUM CHAMBER

ment. The glass vacuum chamber is shown in Figure 47. For the purpose of shielding, the glass chamber was wrapped with aluminum foil and grounded. The glass chamber used the same vacuum pumps as were used with the metal chamber.

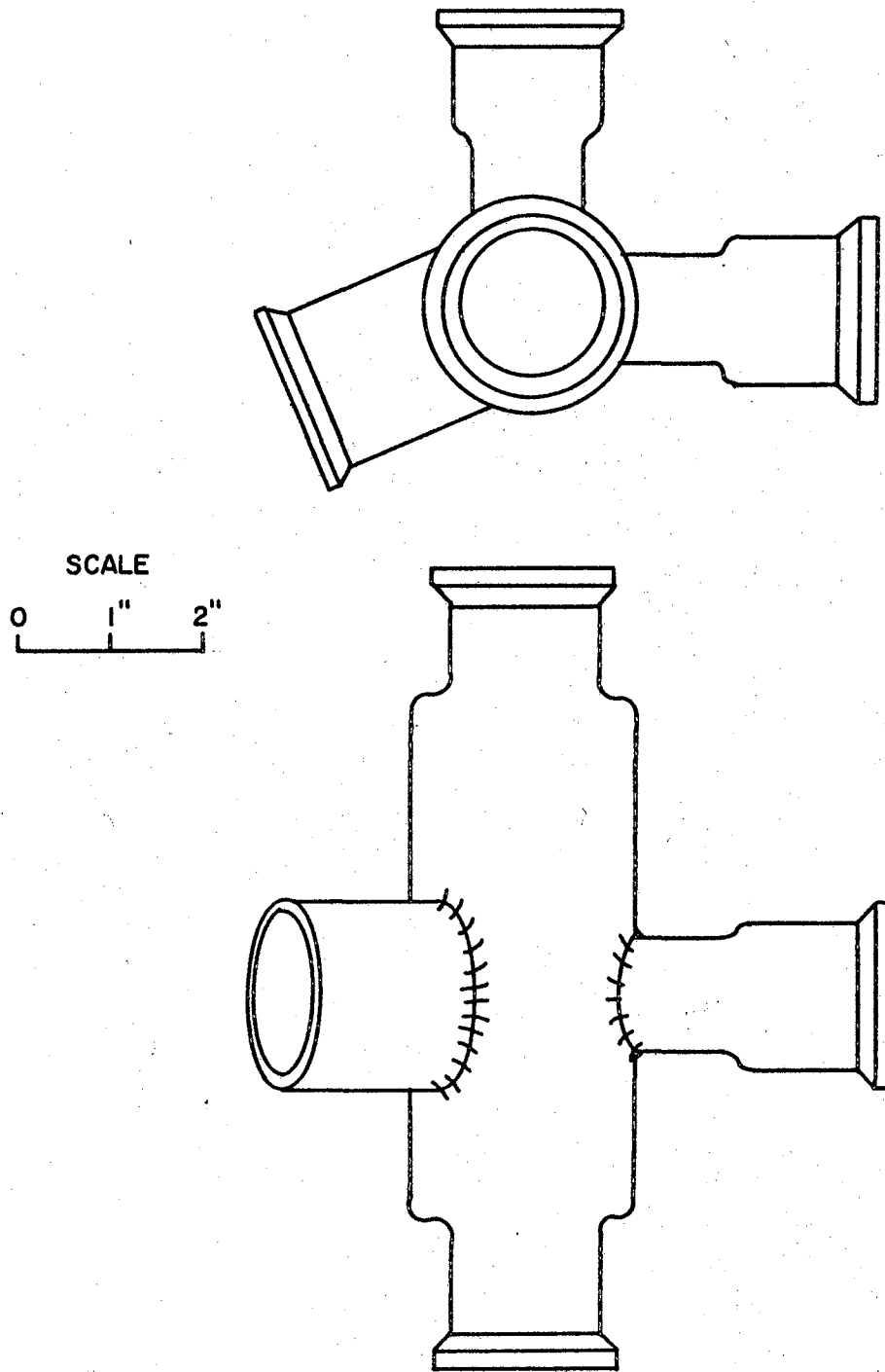


FIG. 47 GLASS VACUUM CHAMBER

## CHAPTER IV

### LASER ENERGY AND POWER

This chapter describes the method used for determining the output energy and power of the twin ruby laser. The output energy is measured directly with a calibrated calorimeter. The design, construction and calibration of the calorimeter will be described in the first part of this chapter. The results of the energy and power measurements will then be shown. Followed by a determination of the energy and power density of the focused laser beam.

#### Energy Measurement

One of the most inexpensive and accurate methods of measuring the output from a ruby laser is through the use of a calibrated "rat's nest" calorimeter. This type of calorimeter was first described by Baker (30) in 1963 and later by Schmidt and Greenhow (31) in 1967. The calorimeter described in this paper incorporates some features of both of the above references.

The main part of the calorimeter is a ball of fine insulated wire, appropriately called a "rat's nest". The tangled ball of wire is used as one arm of a bridge circuit. The calorimeter head is composed of approximately 1450 feet of No. 36 B & S gauge enameled copper wire which was loosely and randomly packed into a 50 ml. glass beaker. The total resistance of the "rat's nest" was 615 ohms. The outside of the beaker



was wrapped with aluminum foil and insulated with a large block of styrofoam. The entrance window to the "rat's nest" was covered with a glass plate to reduce convection currents. The calorimeter head is shown in Figure 48. The calorimeter circuit is shown in Figure 49.

In practice, a small percentage of the laser beam is directed into the calorimeter head. The glass plate reflects 8 percent of the normal incident beam energy and about 18 percent of the remaining energy is back scattered from the "rat's nest". That portion of the energy which is absorbed causes heating of the enamel insulation and the wire. When the wire is heated, the resistance of the "rat's nest" changes. Since the "rat's nest" is in one arm of the bridge circuit shown in Figure 49, a change in resistance will unbalance the circuit and cause a current to flow through the galvanometer. The galvanometer deflection is then a measure of the laser output energy. The "rat's nest" can be calibrated by putting a certain amount of energy into the wire and observing the deflection of the galvanometer. The calibration energy is supplied to the "rat's nest" by capacitor discharge.

Referring to Figure 49, switch S1 is placed in the "Read" position and capacitor C is charged through the resistor R8 to a voltage V. Switch S1 is then placed in the "Calibrate" position and the capacitor discharges through the resistor's R7 (rat's nest) and R6 to ground. Resistor R6 is used to monitor the current pulse through the "rat's nest". The switch S1 is then placed in the "Read" position and the galvanometer deflection D is read. Since the deflection D is proportional to the energy E put into the wire and since the energy E of the capacitor is proportional to the voltage V squared, the relationship between D, E and  $V^2$  is given as,

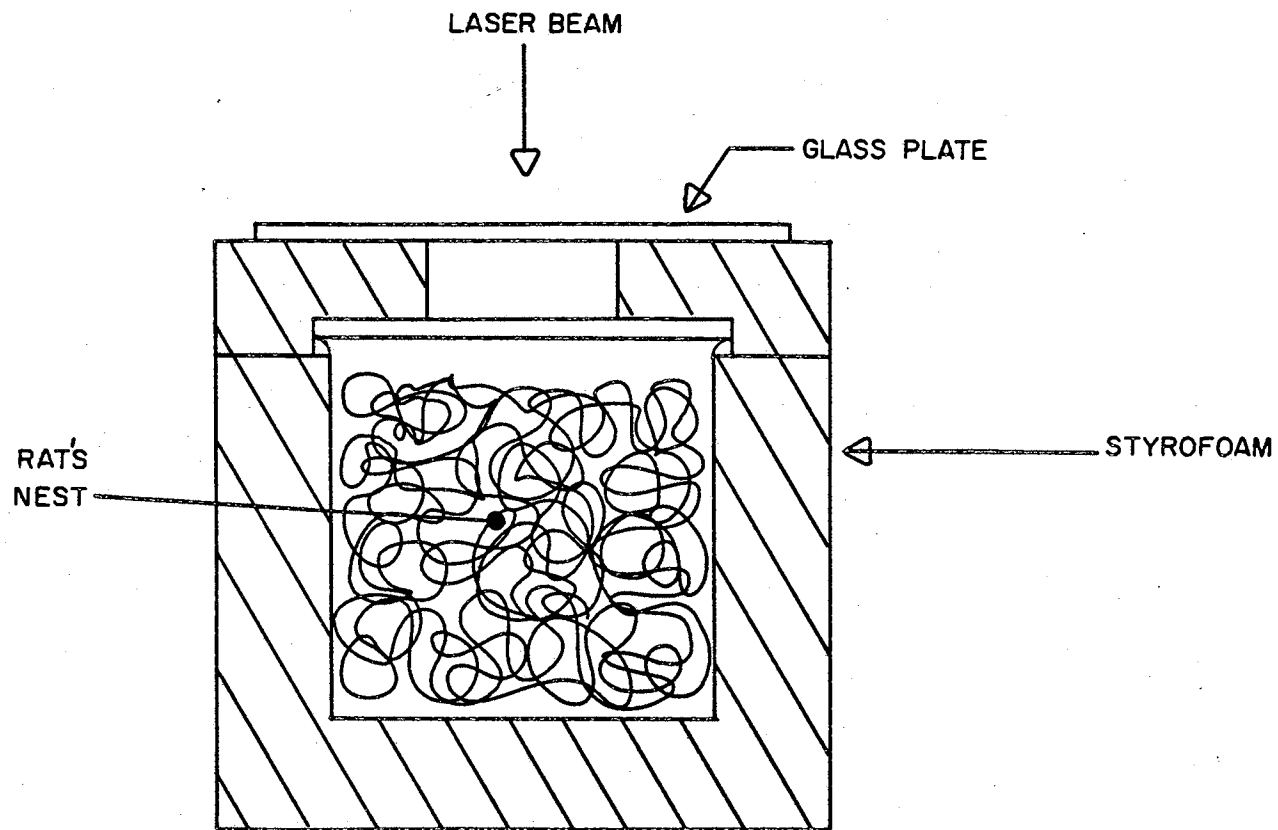
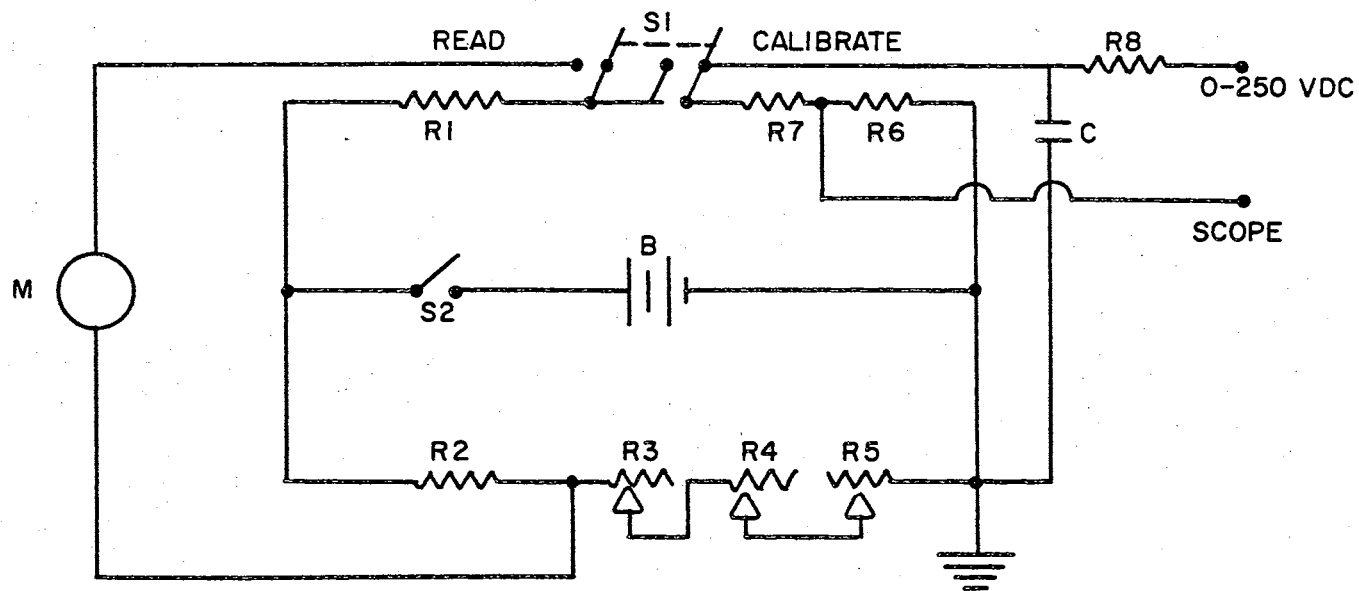


FIG. 48 CALORIMETER HEAD



$R1 = 1,000 \Omega$   
 $R2 = 1,000 \Omega$   
 $R3 = 0-1,000 \Omega$   
 $R4 = 0-25 \Omega$

$R5 = 0-2 \Omega$   
 $R6 = 1 \Omega$   
 $R7 = \text{RATS NEST}$   
 $M = \text{GALVANOMETER}$

$S1 = \text{d.p.d.t.}$   
 $S2 = \text{s.p.s.t}$   
 $B = 6 \text{ V.D.C.}$   
 $C = 16 \text{ mfd}$

FIG. 49 CALORIMETER CIRCUIT

$$D = \alpha E = \frac{1}{2} \alpha CV^2 \quad (45)$$

where  $\alpha$  is a proportionality factor. By plotting  $E$  against  $D$  for various values of  $V$ , a calibration curve can be produced for the "rat's nest". This is shown in Table IX and Figure 50 which also gives the proportionality factor  $\alpha$ . Figure 51 shows how  $\alpha$  changes with  $V^2$ .

In actual use only a small portion of the laser beam is directed into the calorimeter due to the damage threshold of the "rat's nest". The damage threshold of the "rat's nest" is estimated to be about  $.4 \text{ j/cm}^2$ . The energy levels at different points in the optical system are shown in Figure 52. Referring to Figure 52, the following equations can be written,

TABLE IX  
CALIBRATION FACTORS FOR CALORIMETER

V	$V^2$	E	D	$\alpha$
50	2,500	.020	.34	17.1
60	3,600	.029	.53	18.2
70	4,900	.039	.78	20.0
80	6,400	.051	1.07	20.9
90	8,100	.065	1.393	21.5
100	10,000	.080	1.760	22.0
110	12,100	.097	2.159	22.3
120	14,400	.115	2.615	22.7
130	16,900	.135	3.137	23.2
140	19,600	.157	3.685	23.5
150	22,500	.180	4.284	23.8
160	25,600	.205	4.936	29.1
170	28,900	.231	5.618	24.3
180	32,400	.259	6.376	29.6
190	36,100	.289	7.162	24.8
200	40,000	.320	8.00	25.0

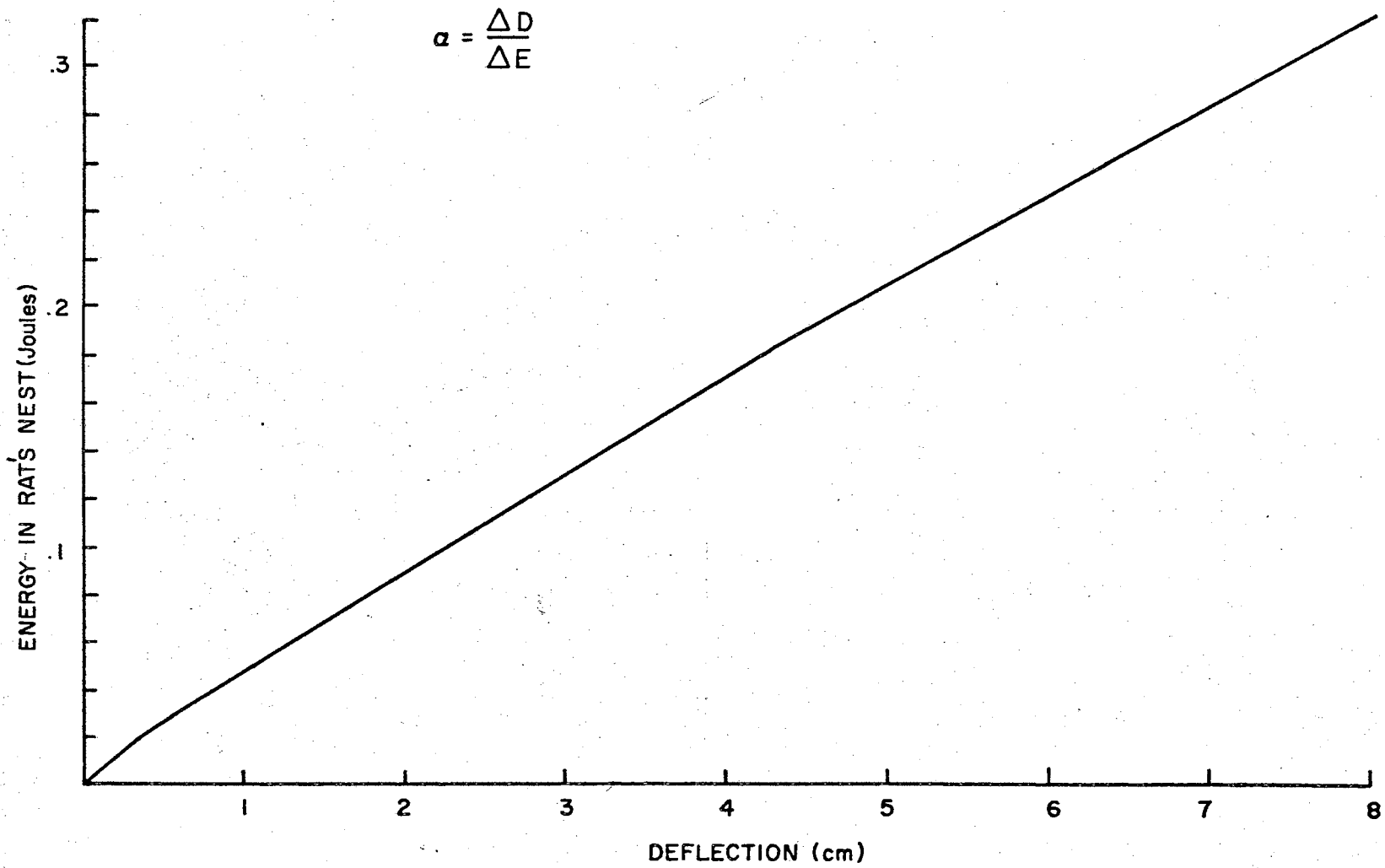


FIG. 50 ENERGY IN RAT'S NEST VERSUS GALVANOMETER DEFLECTION

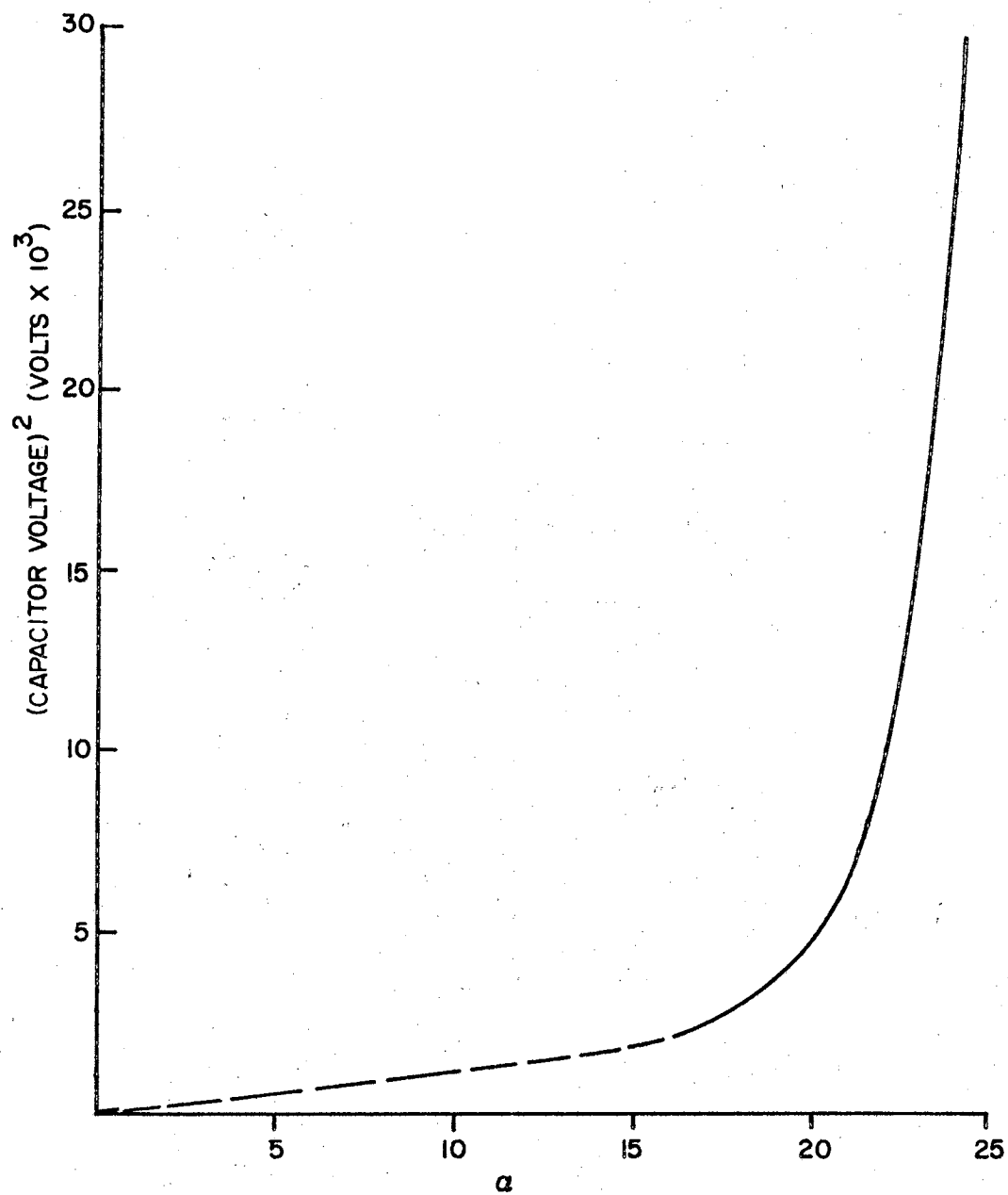


FIG. 51 CAPACITOR VOLTAGE SQUARED VERSUS  $\alpha$

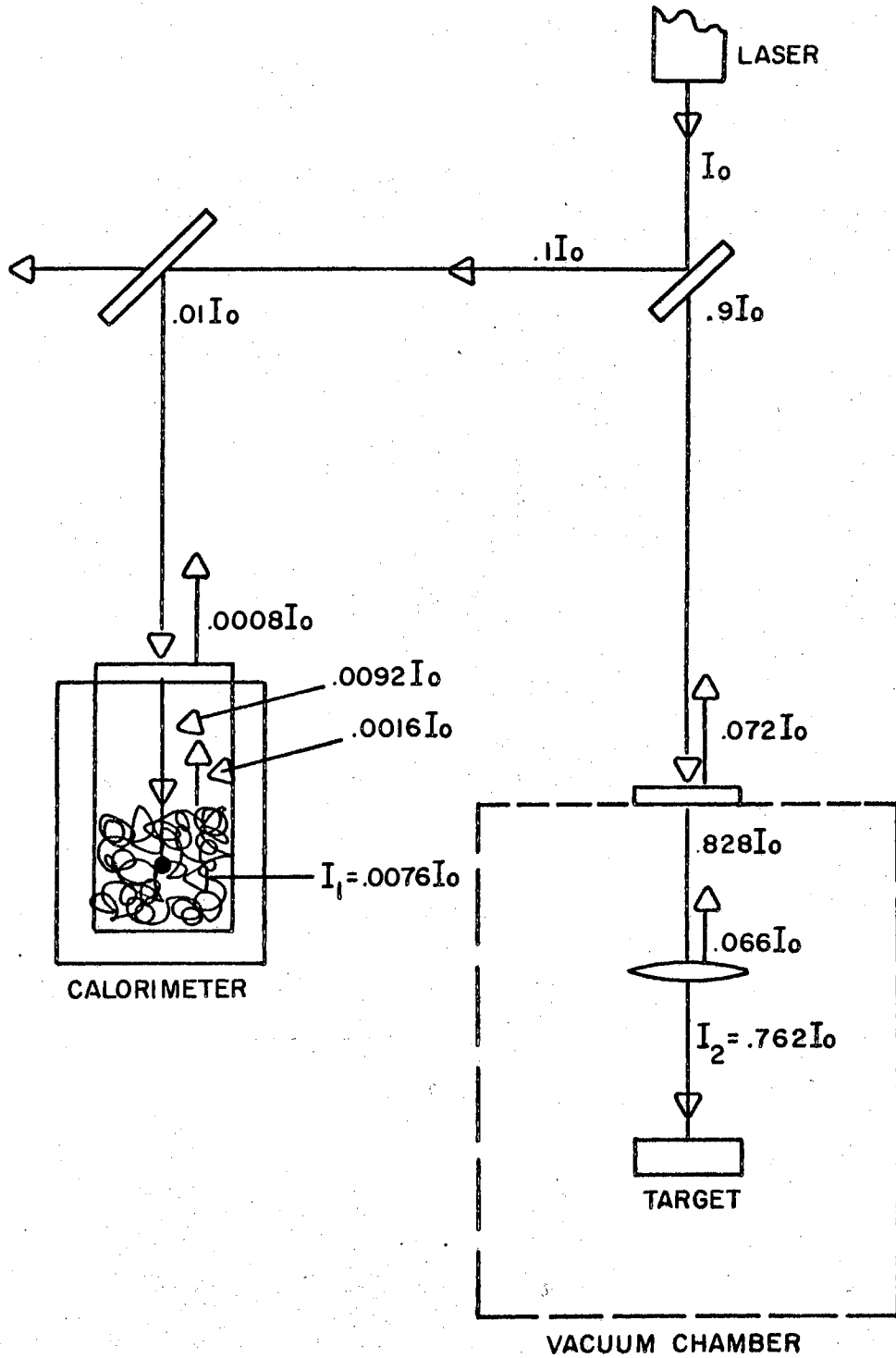


FIG. 52 ENERGY LEVELS IN OPTICAL TRAIN

$$I_1 = .0076I_0 = 7.6 \times 10^{-3} I_0 \quad (46)$$

$$I_2 = .76I_0 = 7.6 \times 10^{-1} I_0 \quad (47)$$

where  $I_0$  is the energy output of the laser,  $I_1$  is the energy measured by the calorimeter and  $I_2$  is the energy delivered to the target. Solving the above equations simultaneously gives,

$$I_1 = I_2 \times 10^2 \quad (48)$$

Figure 53 shows the energy output of the laser as a function of the calorimeter deflection. Figure 54 shows the energy delivered to the target as a function of the calorimeter deflection. The maximum energy output measured with the calorimeter was 15 joules.

#### Power Measurement

In order to determine the power delivered by the twin ruby laser it is necessary to know the energy output of the laser and the pulse duration which is the full width of the waveform measured at half maximum (FWHM). To measure the waveform of the laser pulse it is necessary to use a photometric device which exhibits a fast rise-time and has good spectral response at 6943 Å. The above criteria were met with an RCA 7102, ten stage photomultiplier with an S-1 photocathode. A schematic of the photomultiplier circuit is shown in Figure 55. The photocathode was protected from laser damage by attenuating the laser beam. The experimental arrangement is shown in Figure 56. An optical filter was used to get rid of unwanted flashtube light. The optical filter had a narrow bandpass of 25 Å and peaked at about 6943 Å. A transmission



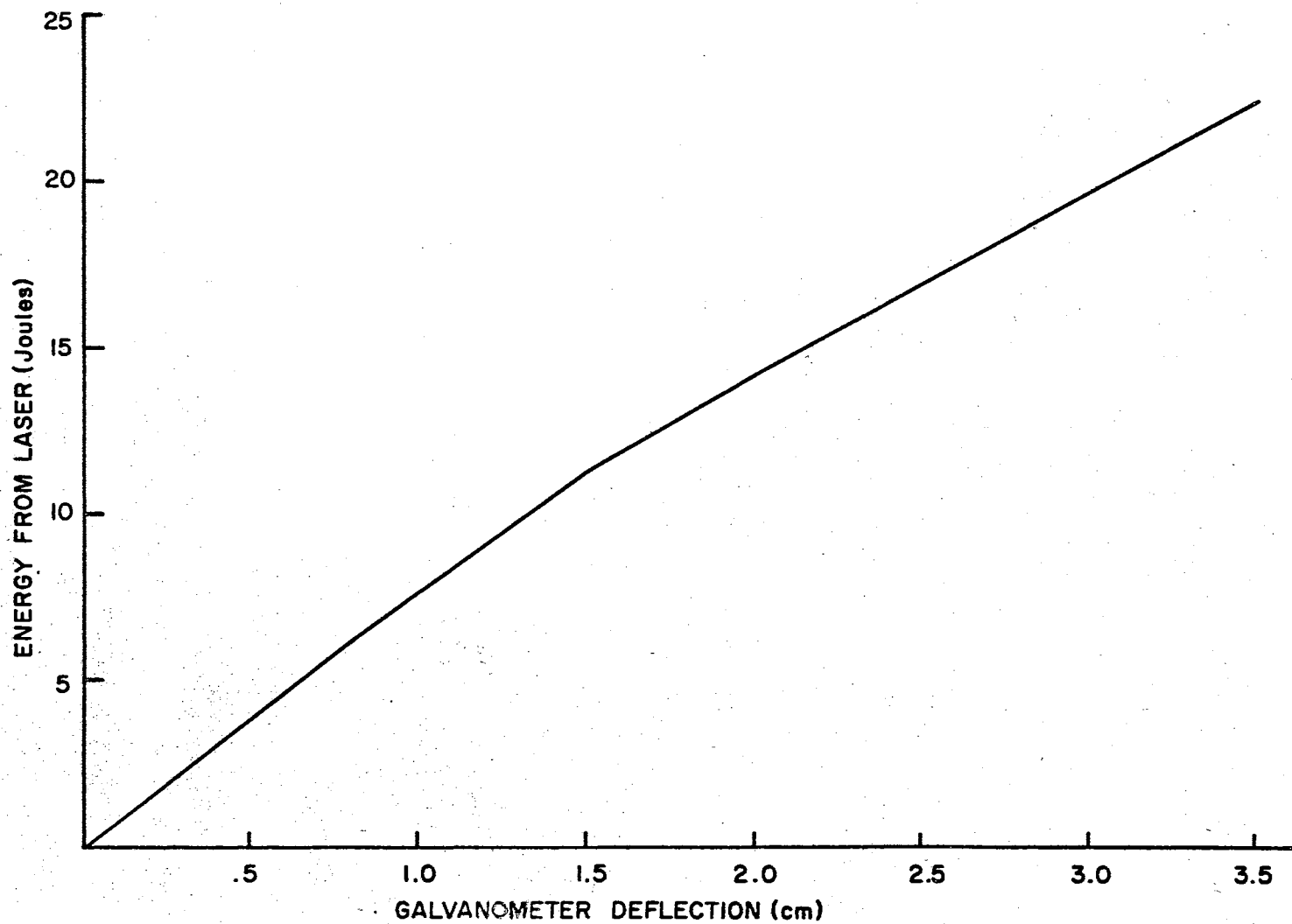


FIG. 53 LASER OUTPUT VERSUS GALVANOMETER DEFLECTION

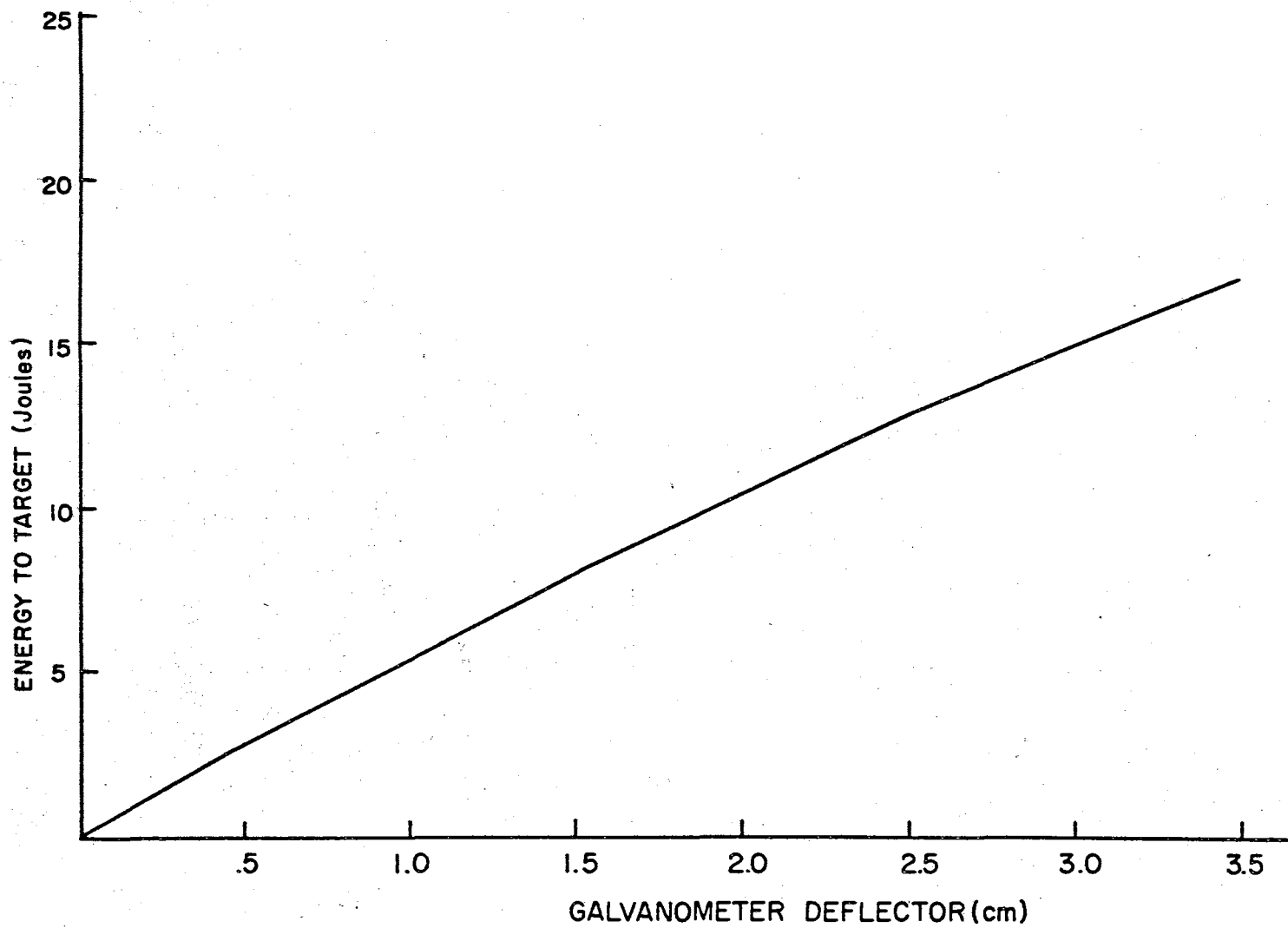


FIG. 54 ENERGY TO TARGET VERSUS GALVANOMETER DEFLECTION

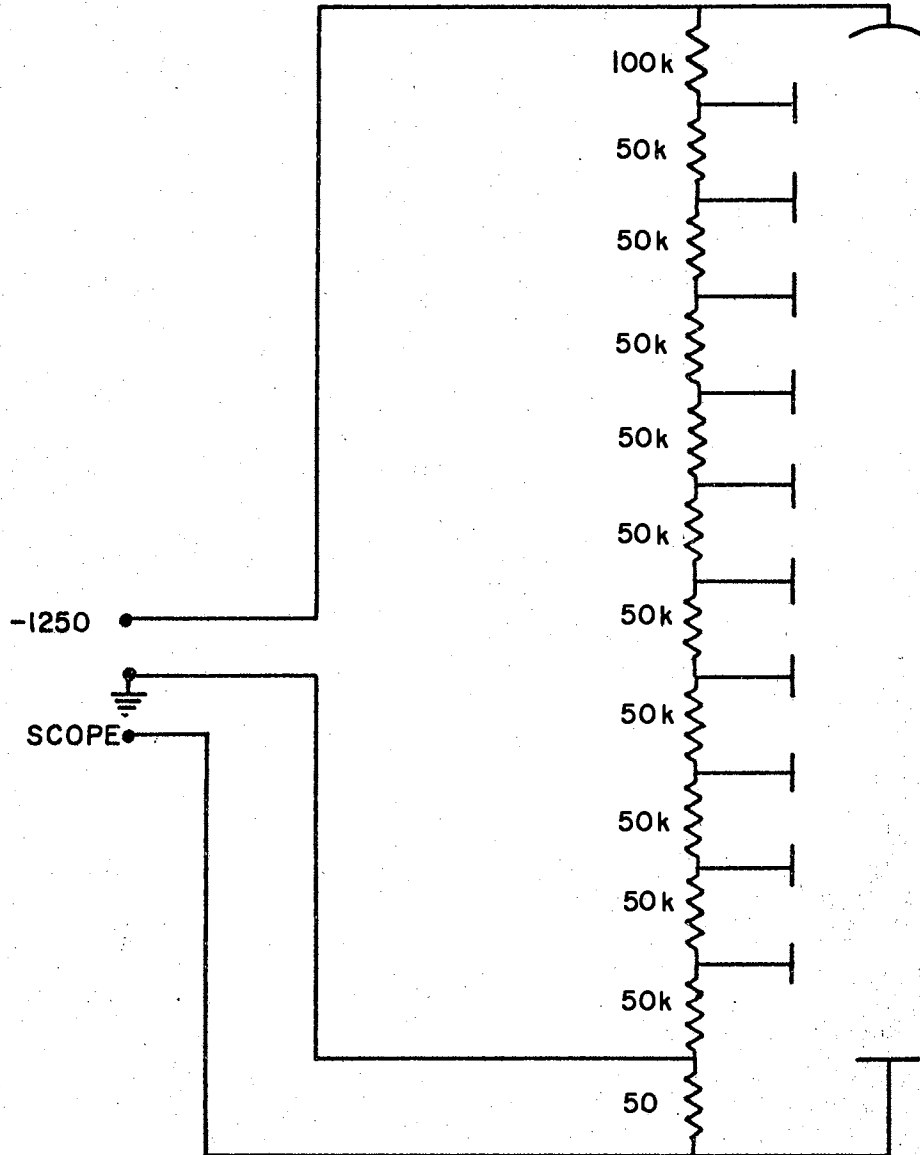


FIG. 55 PHOTOMULTIPLIER CIRCUIT

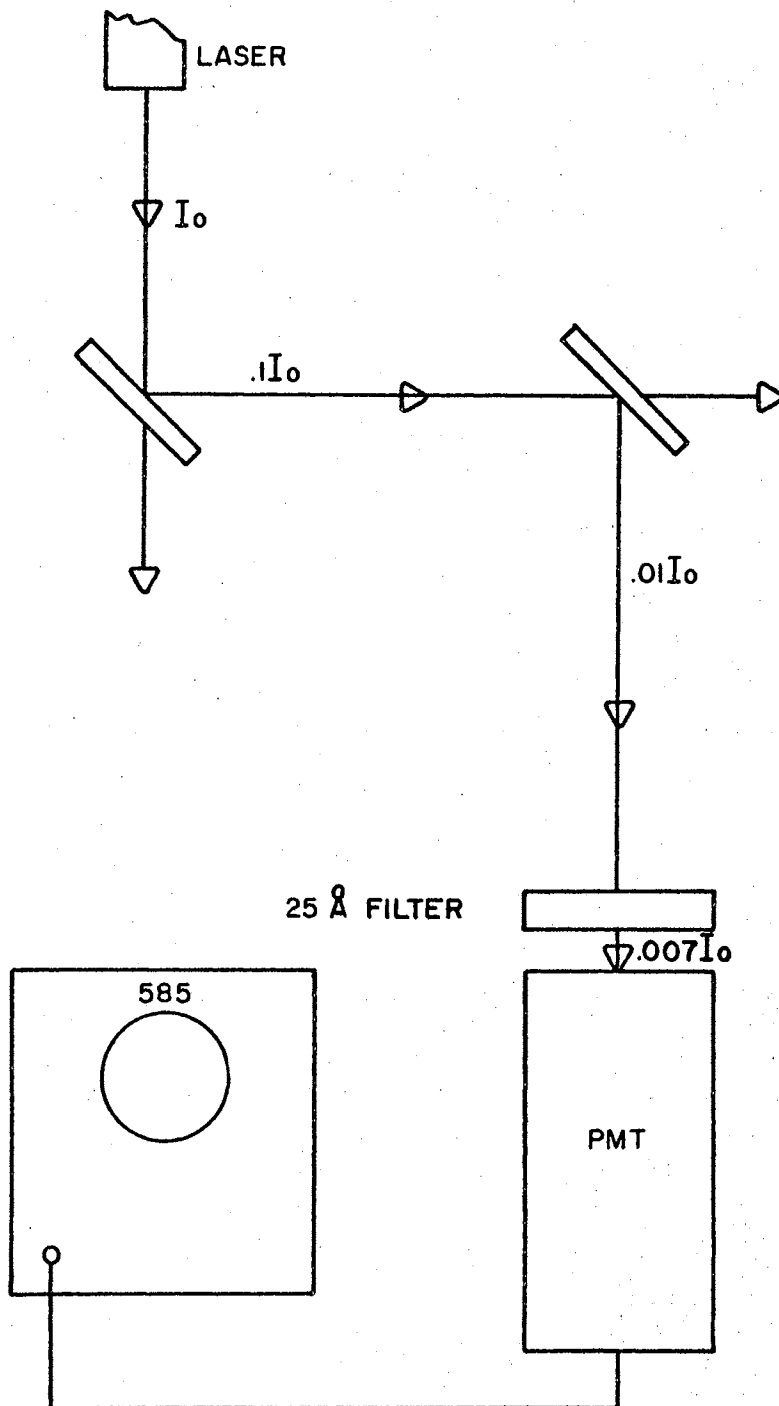


FIG. 56 EXPERIMENTAL WAVEFORM MEASUREMENT

curve of the filter is shown in Figure 57.

The waveform was measured with a Tektronix, Model 585 oscilloscope using 10,000 ASA Poloroid film. With a sweep speed of 50 nsec/cm, the pulse width at half maximum was 30 nsec. A typical pulse shape is given in Figure 58. With a 15 joule energy output and a pulse width (FWHM) of 30 nsec, the power output is calculated to be 500 megawatts. It might be mentioned at this point that the output energy can be measured using the RCA 7102 photomultiplier by integrating the output waveform with a capacitor of 5 pico-farads. However, this type of detector must first be calibrated against a known energy monitor.

#### Laser Beam Divergence

In order to determine laser energy and power densities of the focused laser beam, it is first necessary to determine the divergence of the laser beam. The divergence can be calculated if the diameter of the laser beam is measured at two positions along the optical path as shown in Figure 59. Referring to Figure 59, we can write the following equations,

$$\tan \phi = \frac{y}{x} \quad (49)$$

$$y = \frac{d_2 - d_1}{2} \quad (50)$$

where  $\phi$  is half of the angular divergence,  $y$  is half the vertical displacement,  $x$  is the horizontal displacement,  $d_2$  is the beam diameter at a distance  $x_2$  and  $d_1$  is the beam diameter at a distance  $x_1$ . Substituting (50) into (49) gives,

$$\tan \phi = \frac{d_2 - d_1}{2x} \quad (51)$$

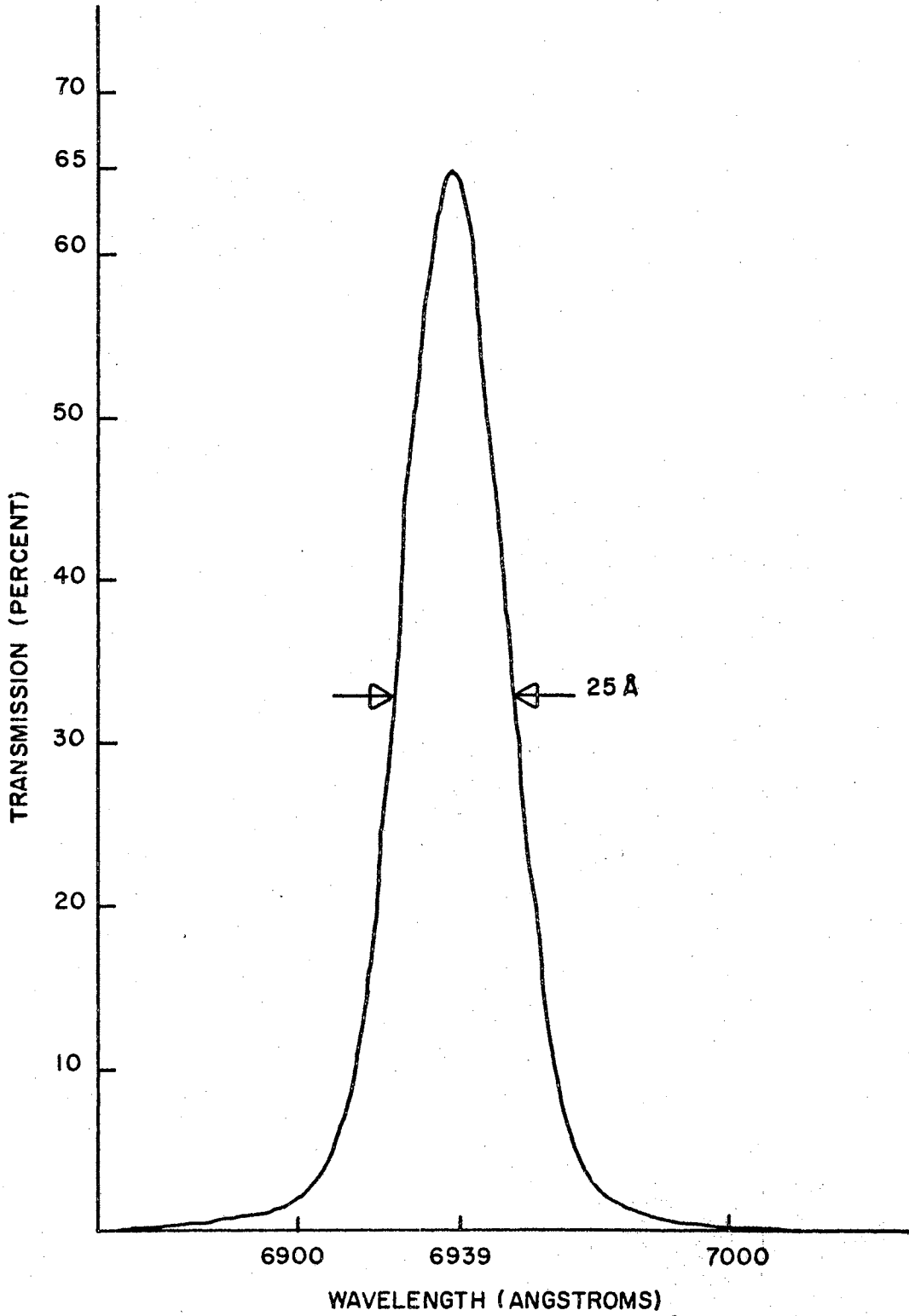


FIG. 57 TRANSMISSION CURVE FOR 6943 Å FILTER

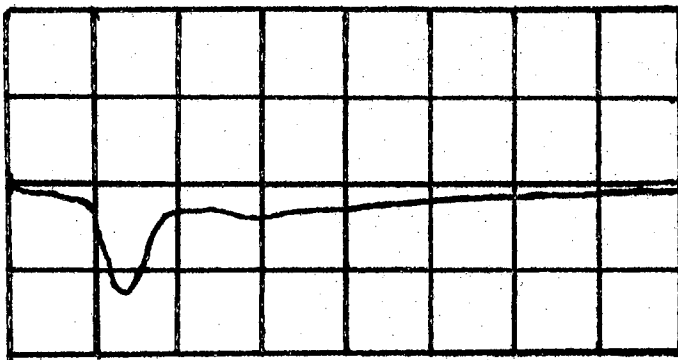


Figure 58. Typical Q-Switched Pulse Shape From  
Twin Ruby Laser. Horizontal  
Scale: 50 nsec/cm.

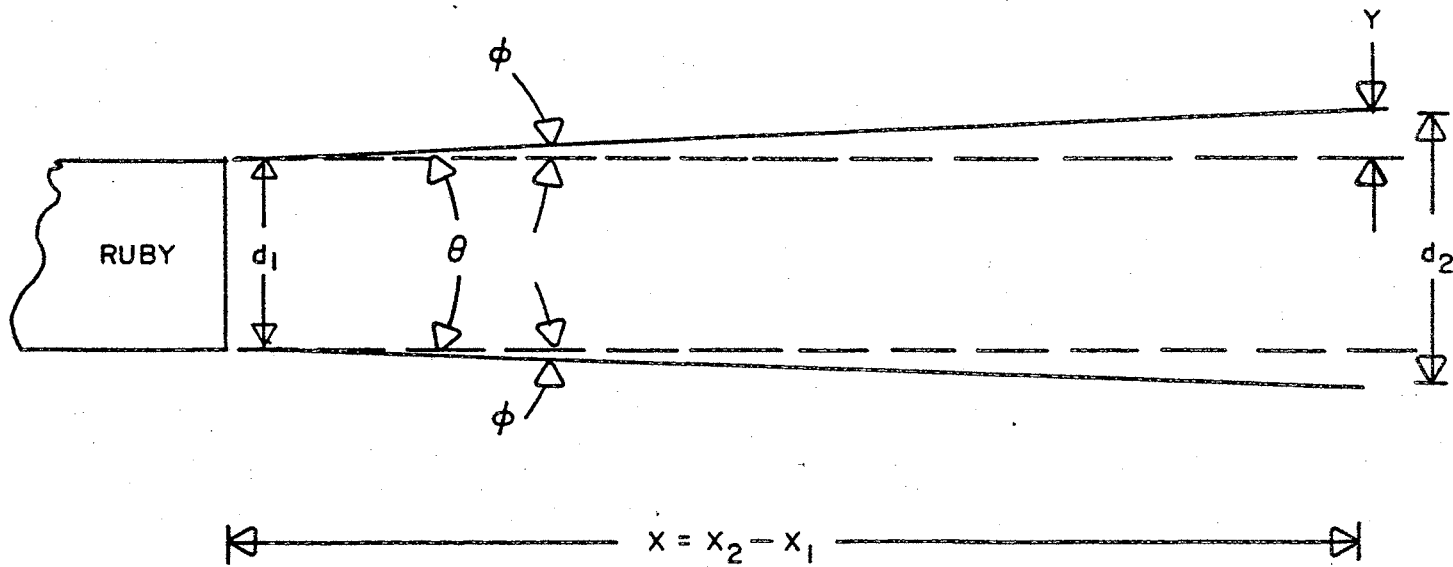


FIG. 59 MEASUREMENTS FOR BEAM DIVERGENCE



Now if  $\frac{d_2 - d_1}{2x} \ll 1$ , Equation (51) can be written as

$$\phi = \frac{d_2 - d_1}{2x} \text{ (rad.)} \quad (52)$$

Since the angular divergence is equal to twice  $\phi$

$$\begin{aligned} \theta &= 2\phi = \frac{d_2 - d_1}{x} \\ \theta &= \frac{d_2 - d_1}{x} \text{ (rad.)} \end{aligned} \quad (53)$$

Equation (53) then gives the angular divergence of the laser beam simply by measuring the beam diameter at two points along the optical path.

Experimentally, photographs of the laser beam were taken at two different points and the beam diameters were measured from the photographs. The experimental setup is shown in Figure 60 and the experimental results are shown in Figure 61. The diameter  $d_1$  was measured to be .5374 inches, diameter  $d_2$  was measured to be .5511 inches and the distance  $x$  was measured to be 34.5 inches. However, due to the cameras used, the actual image size and image size at the focal plane of the camera is in the ratio 1:.9. The actual diameter  $d_1$  is then given as .597 inches and diameter  $d_2$  is given as .612 inches. Putting these values into Equation (53) gives the divergence as,

$$\begin{aligned} \theta &= \frac{d_2 - d_1}{x} \\ \theta &= \frac{.612'' - .597''}{34.5''} \\ \theta &= \frac{.015''}{34.5''} \\ \theta &\cong .43 \text{ mrad} \end{aligned} \quad (54)$$

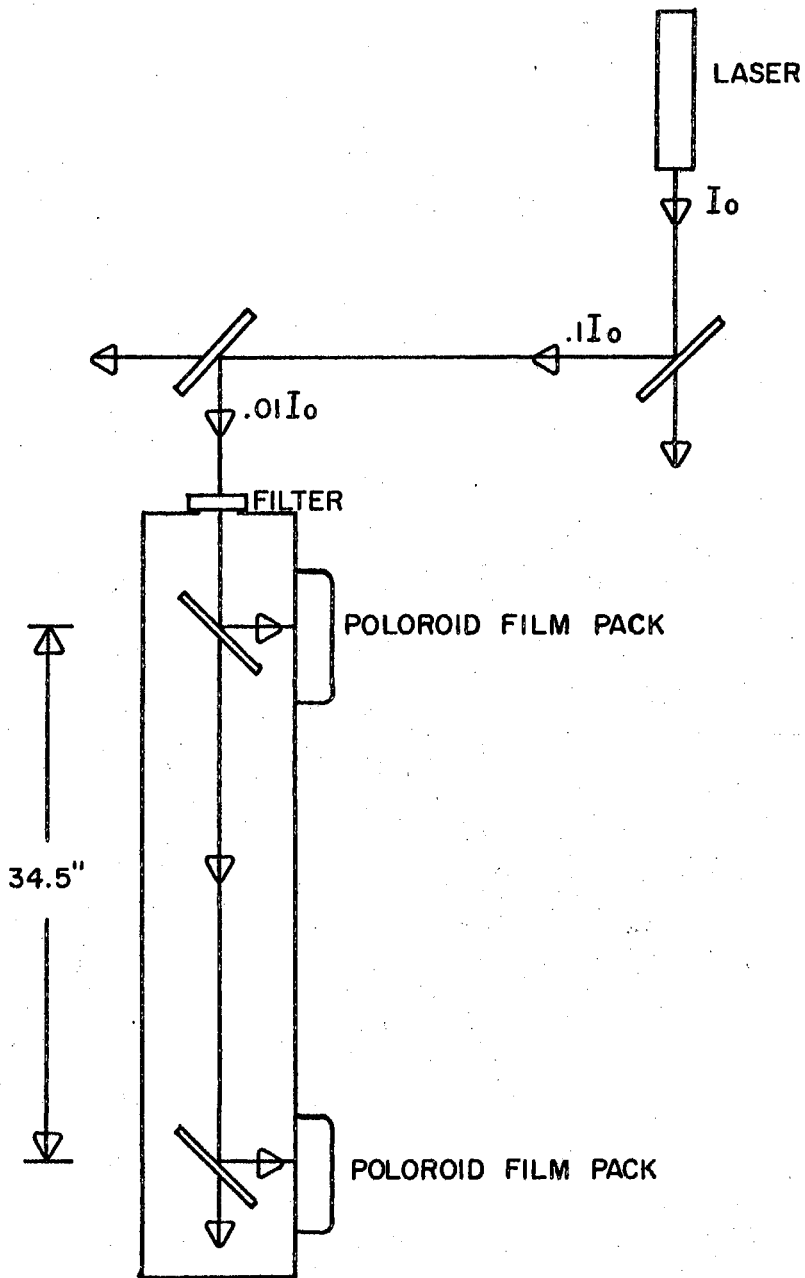


FIG. 60 BEAM DIVERGENCE APPARATUS

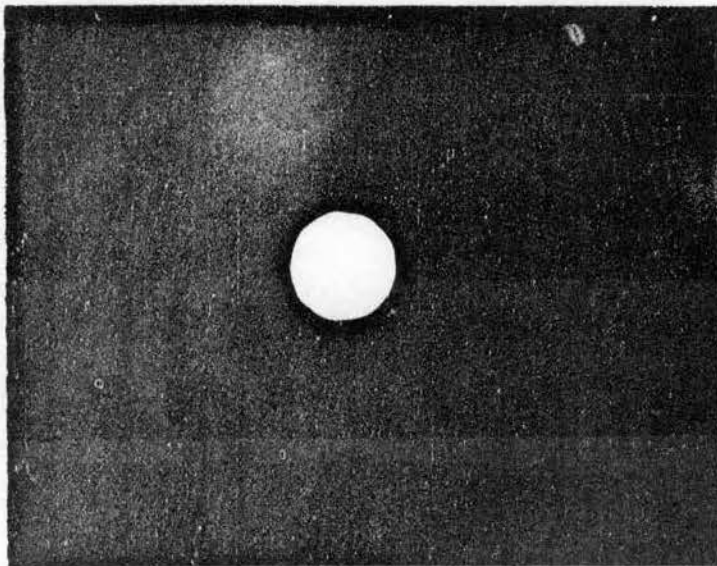
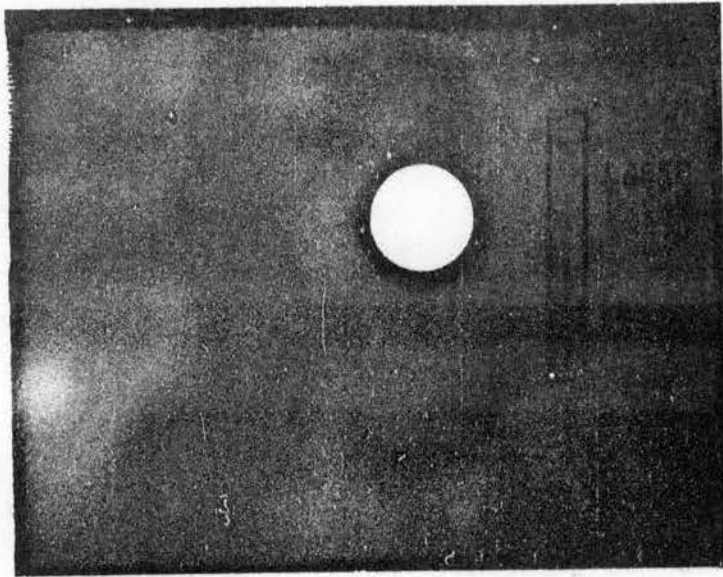


Figure 61. Laser Beam Spot Size

## Energy and Power Densities

Once the beam divergence is known it is a simple matter to calculate the focused spot diameter and from the spot diameter the energy and power density.

The spot diameter at the focus of a lens is given as

$$d = f\theta. \quad (55)$$

where  $d$  is the spot diameter,  $f$  is the focal length of the lens and  $\theta$  is the angular divergence of the laser beam. For a 17 cm focal length lens and a beam divergence of .43 mrad, the spot diameter is calculated to be,

$$\begin{aligned} d &= f\theta = 17 \text{ cm} (.43 \times 10^{-3} \text{ rad}) \\ d &\approx 7.3 \times 10^{-3} \text{ cm} \end{aligned} \quad (56)$$

This diameter gives a cross sectional area of

$$\begin{aligned} A &= \frac{\pi d^2}{4} = \frac{3.14 (53.29 \times 10^{-6} \text{ cm}^2)}{4} \\ A &\approx 4.2 \times 10^{-5} \text{ cm}^2 \end{aligned} \quad (57)$$

Where  $A$  is the cross sectional area and  $d$  is the spot diameter. The energy density  $\Sigma$  is then given as,

$$\begin{aligned} \Sigma &= \frac{E}{A} = \frac{15 \text{ joules}}{4.2 \times 10^{-5} \text{ cm}^2} \\ \Sigma &= 3.5 \times 10^5 \text{ joules/cm}^2. \end{aligned} \quad (58)$$

And the power density  $\pi$  is given as

$$\begin{aligned} \pi &= \frac{P}{A} = \frac{500 \times 10^6 \text{ watts}}{4.2 \times 10^{-5} \text{ cm}^2} \\ \pi &= 1.2 \times 10^{13} \text{ watts/cm}^2. \end{aligned} \quad (59)$$

## CHAPTER V

### TARGET DEFORMATION IN Q-SWITCHED MODE

As previously stated at the end of Chapter II, there have been several studies made of the target deformation caused by a focused laser operating in the Q-switched mode. Experimental data from similar work will now be presented.

The metal vacuum chamber was used in the following experiment. The targets used in the experiments were small aluminum slabs. One set of targets were approximately 1.5 cm long, 1.0 cm wide and .031 cm thick. The other set of targets were approximately .8 cm long, .8 cm wide and .25 cm thick. Before the targets were submitted to laser beam impact, they were thoroughly cleaned with soap and water and then rinsed with high purity methyl alcohol. The targets were then weighed and one set of the targets was placed on a rotatable table in the vacuum chamber. The vacuum chamber was then pumped down to  $2.5 \times 10^{-6}$  torr. All but one target in the vacuum chamber was then irradiated with one laser shot of 30 nsec. duration. This set of targets was then removed and replaced by the other set of targets. The same experimental procedure was carried out for the new set of targets. The small aluminum targets were then measured to obtain the mass loss. One target in each set was not submitted to laser impact in order to measure the amount of contamination to the targets and to determine the measuring error. In both cases there was no measured difference in mass of the control target before

and after the experiment. Table X shows the results obtained from the experiment. The experimental points shown in Table X are plotted in graph form in Figure 62. The results show that as the impact energy increases, the amount of mass removed decreases. This result can probably be explained by the fact that as the peak energy to the target increases, the rate of energy input increases and the temperature of vaporization is reached quicker. Thus, the target is shielded from the laser radiation sooner, resulting in less mass removal but a more energetic plasma. The results also showed that the difference in thickness of the two sets of targets had no bearing on the amount of mass removal. This result indicates that the laser beam and target interaction takes place very close to the surface.

Goldsmith, Waterman and Hirschhorn (32) report that the heat of vaporization of aluminum is approximately  $11.4 \times 10^3$  joules/gm. Knowing the heat of vaporization, the laser energy incident on the target and the mass removed as a result of laser beam and target interaction; the percent of incident energy needed to bring about a certain mass removal can be calculated. The amount of energy required to vaporize a given mass of aluminum is shown as

$$E_v = H_v M_v \quad (60)$$

where  $H_v$  is the heat of vaporization and  $E_v$  is the energy needed to vaporize a mass  $M_v$ . Table XI shows the energy incident on the target ( $E_t$ ), the amount of mass removed from the target ( $M_v$ ), the calculated energy needed to vaporize the amount of mass removed ( $E_v$ ), and the ratio  $R$  of  $E_v$  to  $E_t$ . The quantities  $M_v$  and  $E_v$  are plotted in Figure 63, the slope of which is equal to  $H_v$ . The ratio  $E_v/E_t$  and the quantity  $E_t$

TABLE X  
ENERGY TO TARGET VERSUS MASS REMOVAL

Energy to Target (joules)	Mass Removed (gm x 10 <sup>-4</sup> )
6.0	.46
4.9	.33
7.0	.56
10.9	.69
4.2	.20
9.0	.64
7.0	.59
4.9	.25
4.9	.25
3.8	.14
5.7	.39

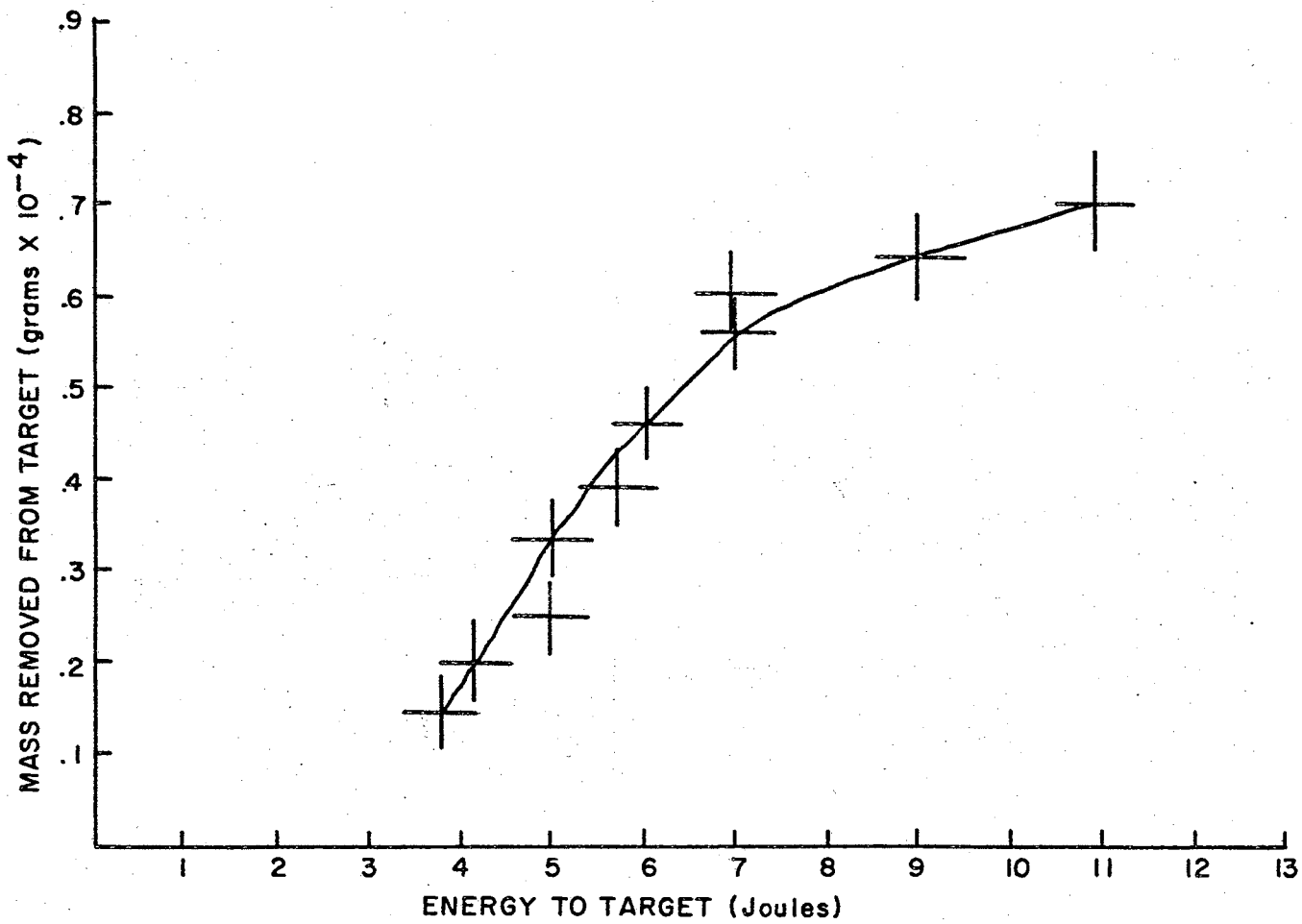


FIG. 62 MASS REMOVAL VERSUS ENERGY TO TARGET



are plotted in Figure 64. From the analysis of Figure 64, it is apparent that the percent of incident energy required to vaporize a given amount of target material is not constant nor is it a linear function as might be expected. In plotting the ratio  $E_v/E_t$  as a function of  $E_t$ , it has been assumed that the heat of vaporization remains constant. It is, however, possible that the heat of vaporization does not remain constant, in which case Equation (60) may be written

$$E_v = H_v(T,P)M_v \quad (61)$$

where T is the temperature of the impact area and P is the pressure on the impact area. From Table XI we have defined the quantity R to be given as

$$R = E_v/E_t \quad (62)$$

Combining Equations (60) and (62) gives,

$$H_v = \frac{RE_t}{M_v} \quad (63)$$

If R is assumed to be constant,  $H_v$  can be calculated for different experimental values of  $E_t$  and  $M_v$  as shown in Tables XII through XX. The heat of vaporization as a function of incident energy is plotted in Figure 65 for different values of R.

Assuming, as stated in Chapter II, that 5 percent of the incident energy goes into heating of the target and 1 percent of the incident energy is reflected or scattered from the surface, the following equation can be written,

$$E_p = 1.0 - E_h - E_r - R \quad (64)$$

TABLE XI  
PARAMETERS INVOLVED WITH MASS REMOVAL

$E_t$ (joules)	$M_v$ (gm x $10^{-4}$ )	$E_v$ (joules)	$R = E_v/E_t$
3.8	.14	.15	.040
4.2	.20	.22	.052
4.9	.25	.28	.057
5.7	.39	.43	.075
6.0	.46	.51	.085
7.0	.57	.63	.090
9.0	.64	.70	.078
10.9	.69	.76	.070

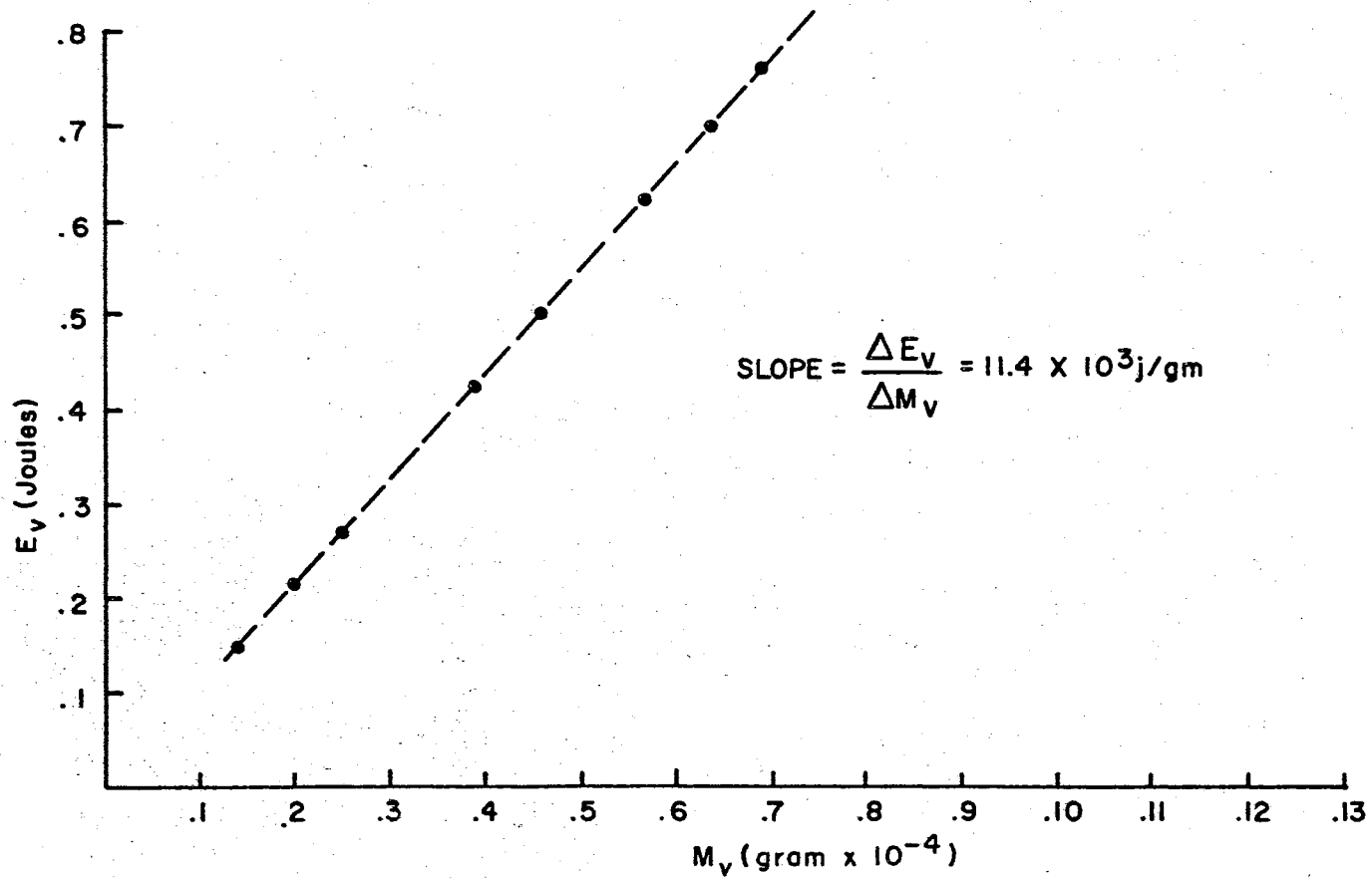


FIG.63 ENERGY OF VAPORIZATION VERSUS MASS VAPORIZED

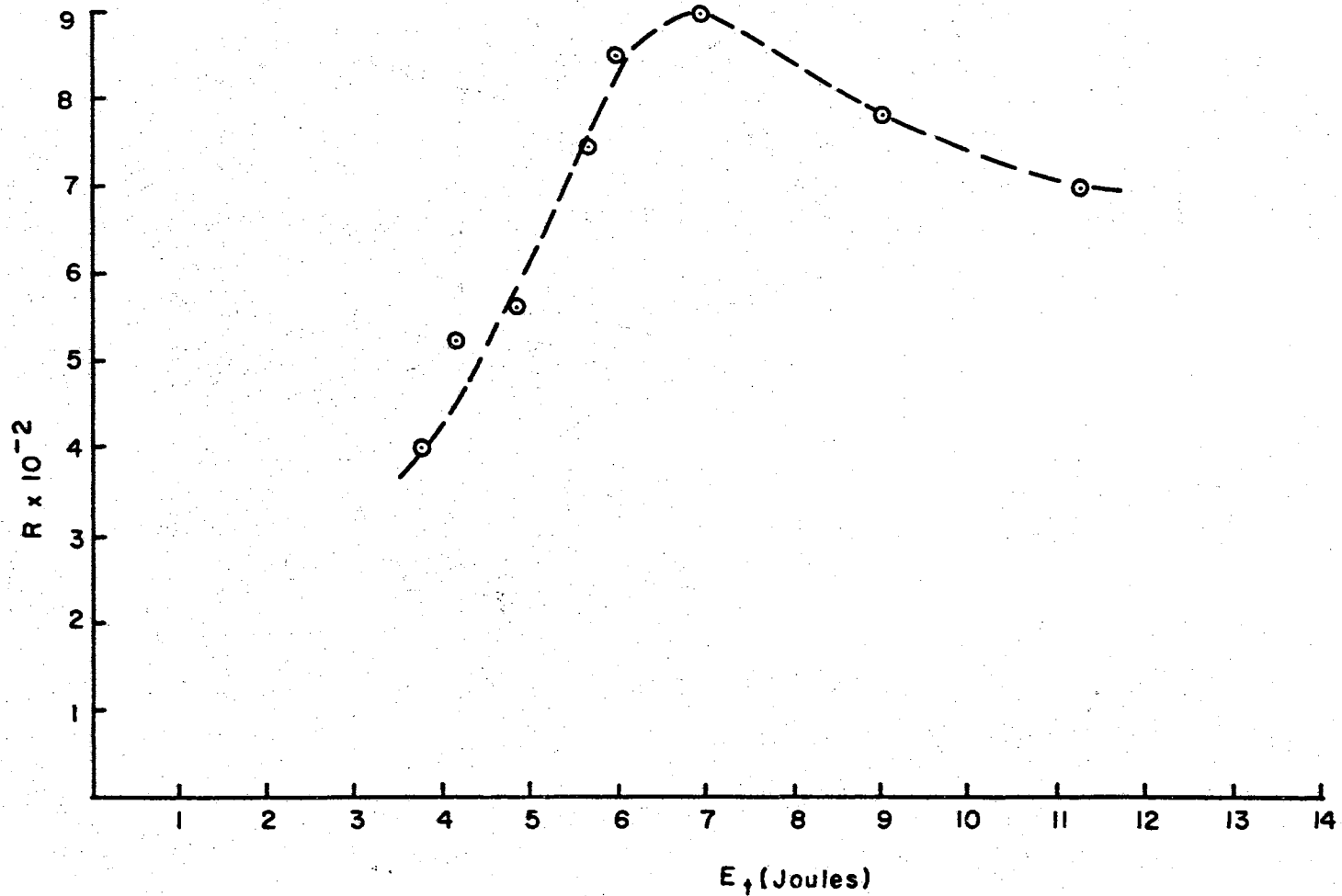


FIG. 64 PERCENT OF INCIDENT ENERGY REQUIRED TO CAUSE TARGET VAPORIZATION

where  $E_p$  is the percent of energy absorbed by the plasma,  $E_h$  is the percent of energy that goes into heating the target,  $E_r$  is the reflected and scattered energy and  $E_v$  is the percent of energy that goes into vaporizing the target material. With the assumed values given above, Equation (64) becomes

$$\begin{aligned} E_p &= 1.0 - .05 - .01 - R \\ E_p &= .94 - R. \end{aligned} \tag{65}$$

For the case where  $H_v$  is assumed to be constant,  $E_p$  varies from 90 percent to 85 percent as  $R$  varies from .04 to .09. For the case of a constant  $R$  but varying  $H_v$ ,  $E_p$  is constant with a value dependent on  $R$ . Figure 66 shows typical photographs of the impact area.

TABLE XII

EXPERIMENTAL VALUES OF MASS REMOVAL PARAMETERS FOR  $R = .02$ 

R	ET	EV	M	H
.02	5.8	.076	.14	.540
---	6.9	.098	.25	.380
---	6.0	.120	.46	.260
---	7.0	.140	.57	.245
---	9.0	.180	.61	.280
---	10.9	.218	.69	.315

TABLE XIII

EXPERIMENTAL VALUES OF MASS REMOVAL PARAMETERS FOR  $R = .03$ 

R	ET	EV	M	H
.03	3.8	.114	.14	.815
---	4.9	.148	.25	.590
---	6.0	.180	.46	.390
---	7.0	.210	.57	.370
---	9.0	.270	.64	.420
---	10.9	.328	.69	.475

TABLE XIV

EXPERIMENTAL VALUES OF MASS REMOVAL PARAMETERS FOR  $R = .04$ 

R	ET	EV	M	H
.04	3.8	.148	.14	1.06
---	4.9	.190	.25	.76
---	6.0	.240	.46	.52
---	7.0	.280	.57	.49
---	9.0	.360	.64	.56
---	10.9	.435	.69	.63

TABLE XV

EXPERIMENTAL VALUES OF MASS REMOVAL PARAMETERS FOR  $R = .05$ 

R	ET	EV	M	H
.05	3.8	.190	.14	1.36
---	4.9	.245	.25	.98
---	6.0	.300	.46	.65
---	7.0	.350	.57	.61
---	9.0	.450	.64	.70
---	10.9	.545	.69	.79

TABLE XVI

EXPERIMENTAL VALUES OF MASS REMOVAL PARAMETERS FOR  $R = .06$ 

R	ET	EV	M	H
.06	3.8	.228	.14	1.628
---	4.9	.294	.25	1.176
---	6.0	.360	.46	.783
---	7.0	.420	.57	.737
---	9.0	.540	.64	.844
---	10.9	.654	.69	.948

TABLE XVII

EXPERIMENTAL VALUES OF MASS REMOVAL PARAMETERS FOR  $R = .07$ 

R	ET	EV	M	H
.07	3.8	.266	.14	1.900
---	4.9	.343	.25	1.372
---	6.0	.420	.46	.913
---	7.0	.490	.57	.860
---	9.0	.630	.64	.984
---	10.9	.763	.69	1.106



TABLE XVIII

EXPERIMENTAL VALUES OF MASS REMOVAL PARAMETERS FOR  $R = .08$ 

R	ET	EV	M	H
.08	3.8	.304	.14	2.171
---	4.9	.392	.25	1.568
---	6.0	.480	.46	1.043
---	7.0	.560	.57	.982
---	9.0	.720	.64	1.125
---	10.9	.872	.69	1.264

TABLE XIX

EXPERIMENTAL VALUES OF MASS REMOVAL PARAMETERS FOR  $R = .09$ 

R	ET	EV	M	H
.09	3.8	.342	.14	2.443
---	4.9	.441	.25	1.764
---	6.0	.540	.46	1.174
---	7.0	.630	.57	1.105
---	9.0	.810	.64	1.266
---	10.9	.981	.69	1.422

TABLE XX

EXPERIMENTAL VALUES OF MASS REMOVAL PARAMETERS FOR  $R = .10$ 

R	ET	EV	M	H
.10	3.8	.38	.14	2.70
---	4.9	.49	.25	1.96
---	6.0	.60	.46	1.30
---	7.0	.70	.57	1.22
---	9.0	.90	.64	1.40
---	10.9	1.09	.69	1.58

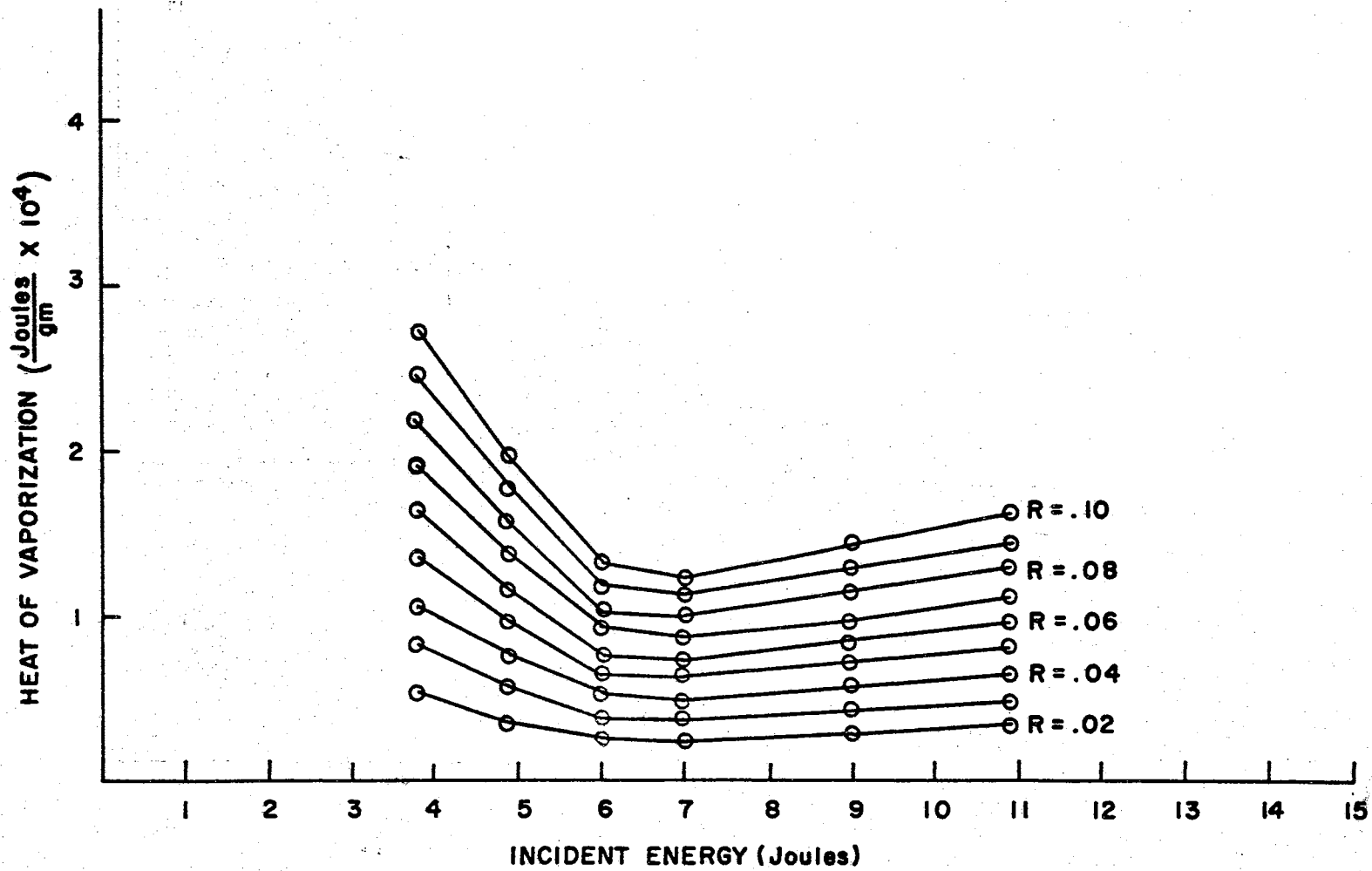


FIG. 65 HEAT OF VAPORIZATION VERSUS INCIDENT ENERGY

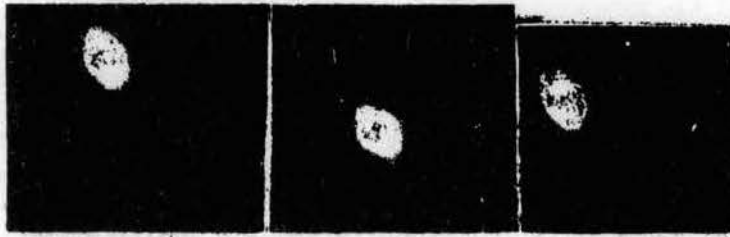


Figure 66. Photographs of Target Deformation

## CHAPTER VI

### PLASMA PRODUCTION

One of the more interesting aspects of impacting a focused laser beam onto a solid aluminum target is the plasma produced as a result of this interaction. The ruby laser has proven to be an invaluable tool for high temperature, high density plasma production. One very promising example of its application is in producing a high temperature plasma that can attain fusion temperatures. From the manner in which the laser produces a plasma, the plasma itself is very transient. This transient nature offers many experimental challenges to the research scientist and has pushed the state-of-the-art in high speed measurements. This chapter will describe several experiments that were undertaken by the author to gain an insight into the properties of a transient, laser-produced plasma.

#### Introduction

After performing the mass removal experiment that is described in the previous chapter, the question arose as to the symmetry of the plasma about the axis of the laser beam. In order to investigate the possibility of non-symmetry, and to determine the velocity of plasma expansion, a probe was designed. Before describing the experiments with the probe, the author wishes to give some background information on probe measurements.

Any conducting probe that is connected so as to pass current from one position in the plasma to a circuit that provides a reference potential will collect a current. The amount of current is a function of the characteristics of the plasma at the position of the probe. This phenomena was discovered early in this century. The first theory on the use of probes in glow discharges was published by I. Langmuir and H. M. Moth-Smith (33) in 1923. Langmuir showed that measurements with probes could be employed to obtain the potential at the point of the probes insertion into a rarified discharge and that the ionization density could be determined at that point.

#### Kinetic Theory Concepts

By the application of the kinetic theory of gases, additional measurements could be obtained, such as the effective electron temperature of the plasma and the density of the positive ions in the plasma at the position of the probe. Assuming that the energy distribution of electrons in the gas are Maxwellian, the following equation may be written:

$$\frac{1}{2} m_e v_e^2 = \frac{3}{2} n k T = \frac{3}{2} k T_e = eV \quad (66)$$

where  $m_e$  is the electron mass,  $v_e$  is the electron velocity,  $n$  is the Townsend Multiplier to express the electron energy as a multiple of the molecular energy at the gas temperature  $T$ ,  $k$  is Boltzman's constant,  $T_e$  is the equivalent electron temperature and  $eV$  is the electron energy expressed in electron-volts. There is also a similar set of relations which expresses conditions for the positive ions.

### Probe Measurements

The theory of the Langmuir probe, as outlined by Loeb (34), will be presented with frequent reference of Figure 67, which schematically depicts a glow-discharge plasma. When a probe is used it is usually inserted into the plasma which exists between the anode and cathode. If the cathode is grounded and the anode is at a potential,  $V_a$ , there must be a decrease in the potential from the anode to the cathode. Assume that a plane parallel probe electrode (P) is placed into the plasma with its surface parallel to the axis of the tube and its center at some point (B) in the plasma which is at a potential ( $V_b$ ), called the "space potential," with respect to the grounded cathode. By means of the voltage supply (C) and the voltage divider (R), the probe can be made negative with respect to the anode by the amount  $V_a - V_p$  so the potential  $V = V_p - V_b$  may be made positive or negative by an amount equal to the voltage of the voltage supply (C). The galvanometer, or microammeter, (G) permits one to measure the current,  $i$ , to the probe as the potential  $V$  is changed. In some cases, the current density,  $j$ , will be evaluated. Since a space charge sheath surrounds the probe, the effective surface area of the probe is difficult to determine.

#### Strongly Negative Probe

If the potential,  $V_p$ , on the probe is very negative with respect to potential,  $V_b$ , of the plasma at the point B, i.e.,  $V = V_p - V_b \ll 0$ , the electrons in the plasma are repelled by the plate, P. As a consequence a positive-ion space-charge-limited current,  $i_+$ , flows to the plate, P. This is evident since the fastest electrons in the plasma have suffic-

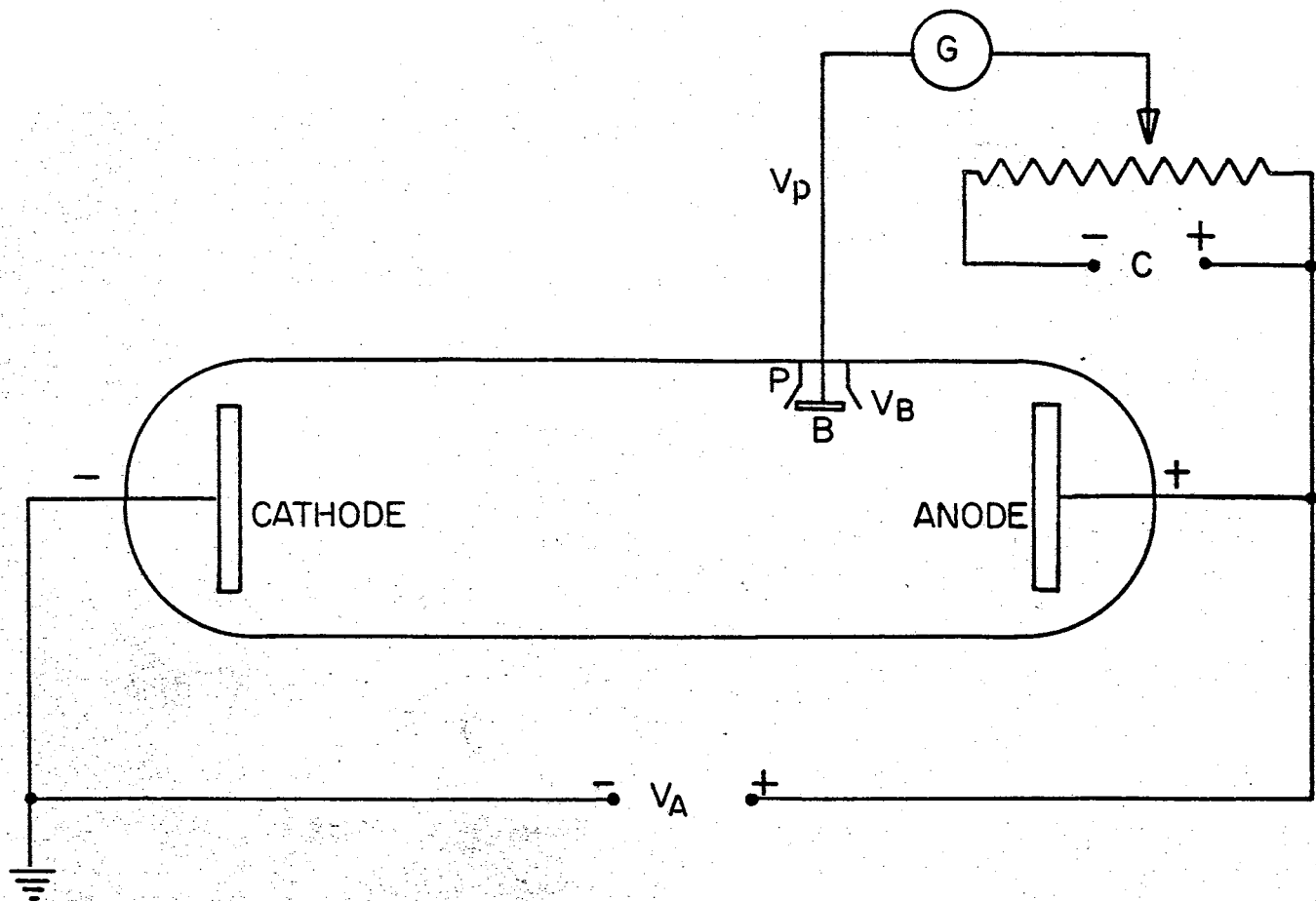


FIG. 67 SCHEMATIC OF GASEOUS DISCHARGE APPARATUS



ient energy to reach the probe with its high negative potential. This negative potential is evidence of the presence of a positive-ion space charge sheath. The thickness,  $d$ , of the positive ion sheath is a function of the ratio of the negative potential of the probe,  $V_p$ , to the average density and energy of the electrons in the plasma. This is true since the velocity of the electrons determines their closest approach to the probe before the electrons are repulsed by the high electric field. For practical purposes, the outer area of the space charge sheath may be taken as the effective electrode area. Outside of the space-charge sheath,  $F$ , the ion density is  $N_+$ . The electron probe current,  $i_p$ , is equal to the ion probe current,  $i_f$ , which flows through the space charge sheath,  $F$ , provided no ionization by impact occurs within the sheath and no electrons are liberated by any action from the probe.

Because of the random motion of the ions, the ions diffuse into the sheath across the area of the space-charge sheath,  $F$ . This positive probe current is described by the equation

$$i_+ = \frac{FN_+ e \bar{v}_+}{4} \quad (67)$$

where  $i_+$  is the ion probe current,  $F$  is the area of the sheath,  $e$  is the charge of an electron,  $N_+$  is the ion density and  $\bar{v}_+$  is the mean ion velocity. The current density is determined by dividing equation 67 by the area of the sheath and thus gives the equation,

$$j_+ = \frac{N_+ e \bar{v}_+}{4} \quad (68)$$

where  $j_+$  is the ion current density. Equation 68 can also be written in terms of the voltage,  $V$ , and the thickness,  $d$ , of the space-charge sheath in the following form,

$$j_+ = \frac{1}{9\pi} \frac{2e}{m_+} \frac{V^{3/2}}{d^2} = \frac{N_+ e \bar{v}_+}{4} \quad (69)$$

where  $M_+$  is the ion mass. For strongly negative values of  $V$ , the ion current  $j_+$ , is constant and  $d$  varies as  $V^{3/4}$ . It is therefore, possible to calculate  $d$  if  $j_+$ ,  $M_+$  and  $V$  are known. In addition, the ion density,  $N_+$ , may be calculated for this condition.

A similar argument can be followed for a cylindrical probe and a spherical probe rather than a plane probe. The theory of the spherical probe and cylindrical probe is given by Langmuir and Blodgett (35).

#### Energy Distribution and Electron Temperature

As the negative voltage,  $V$ , is reduced,  $V_p$  becomes less negative with respect to  $V_b$ . The ion current is constant at first and only the value of  $d$  decreases. When  $V$  becomes sufficiently low, the faster electrons with normal incidence to the probe are able to penetrate the distance,  $d$ , and to reach the probe surface. This penetration of the probe sheath produces an electron current,  $i_-$ , which reduces the probe current  $i_p = i_+$  to a value given by

$$i_p = i_+ - i_- \quad (70)$$

where  $i_-$  is the electron current that reaches  $P$ . If it is assumed that the molecules inside the sheath do not influence the electrons, then the change of electron current with a decrease in  $V$  would give a clear picture of the energy distribution of the electrons.

In a Maxwellian energy distribution, the number of electrons which are incident on the area,  $A$ , of electrode per second with a velocity

component normal to the surface between  $v_n$  and  $v_n + dv_n$ , is given by

$$N_n = \frac{N_-}{a\sqrt{\pi}} \exp\left(-\frac{v_n^2}{a^2}\right) dv_n. \quad (71)$$

The current  $i_-$  will then be given as

$$i_- = \frac{Ae N_-}{4\sqrt{\pi}} \int_{v_0}^{\infty} \frac{v_n}{a} \exp\left(-\frac{v_n^2}{a^2}\right) dv_n \quad (72)$$

$$i_- = \frac{Ae N_- a}{2\pi} \exp\left(-\frac{v_0^2}{a^2}\right) \quad (73)$$

where  $v_0$  is defined by the expression

$$\frac{1}{2} m_- v_0^2 = eV_e \quad (74)$$

Assuming  $a^2 = 2kT_-/m_-$  and  $V_e = \frac{1}{2} m_- v_0^2$ , the current of electrons  $i_-$  reaching the probe is given as

$$i_- = e AN_- \sqrt{\frac{k T_-}{2\pi m_-}} \exp\left(\frac{-eV_e}{kT_-}\right) \quad (75)$$

where  $T_-$  is the electron temperature in degrees K, and  $m_-$  is the electron mass. For non-Maxwellian velocity distributions, the quantity  $N_n$  in Equation 71 must be changed to  $N-f(v_n)dv_n$  where  $f(v_n)$  represents the form of the energy-distribution function.

Assuming a Maxwellian energy distribution of the electrons and that the electron temperature and electron density are independent of  $V$ , Equation 75 may be written in logarithmic form as

$$\ln \left( \frac{i^-}{A} \right) = \ln j^- = \ln \left( e N^- \sqrt{\frac{kT}{2\pi m^-}} \right) - \frac{Ve}{kT}$$

$$\ln \left( \frac{i^-}{A} \right) = \ln j^- = B - \frac{Ve}{kT} . \quad (76)$$

If Equation 76 is plotted logarithmically against  $V$ ,  $\ln j^-$  yields a straight line, with its slope equal to  $Ve/kT^-$  and its intercept with the  $j^-$  axis given by  $B$ . From Equation 76 it is possible to write

$$\frac{d(\ln j^-)}{d(V)} = \frac{d(\ln j^-)}{d(V_p)} = - \frac{e}{k T^-} . \quad (77)$$

Since the constants  $e$  and  $k$  are known, the slope yields the value of  $T^-$ , the electron "temperature."

#### Wall Potential

If  $V$  is decreased further, a point will be reached when  $i_p = i^+ - i^- = 0$ . The potential  $V$  at which the above condition occurs is called the "wall potential" and is designated  $V_w$ . When  $i^- = i^+$ , the random electron current from diffusion is equal to the positive space-charge limited current from the potential,  $V_w$ . Since the electrons and the ions have the same energy when they are in equilibrium, the electrons have a higher random velocity and will reach the probe even against a negative potential  $V_w$ . The electrons will reach the probe in greater numbers than the slower ions and thus cause  $V$  to have a momentary negative value. The negative value of  $V_w$  is then enough to draw in the positive space-charge-limited current to a point where  $i^- = i^+$ , so that no net current flows and  $i_p = 0$ . At the surface of the probe, or wall, the electrons and ions moving over the surface in two dimensions readily

recombine, giving their heat of combination to the wall. This diffusion to the walls of a discharge tube causes a loss of carriers from the plasma to the walls. As this mechanism is basically one of diffusion involving both electrons and ions, it is called ambipolar diffusion.

The process of ambipolar diffusion has been studied in detail, primarily in plasmas where the conditions are relatively simple. The effects of ambipolar diffusion are more pronounced for electrons in gases where  $\bar{v}_- \gg \bar{v}_+$ , but occur wherever the electrons and ions have different mobilities.

If the wall potential is given as

$$V_w = V_p - V_B \quad (78)$$

when  $i_- + i_+ = i_p = 0$ , theoretically

when  $V = V_w$ ,

$$i_+ = \frac{e N_+ \bar{v}_+}{4} = \frac{e N_- \bar{v}_-}{4} \exp\left(\frac{-e V_w}{k T_-}\right) = i_- \quad (79)$$

If  $N_+ = N_-$ , then Equation 79 simplifies to

$$V_w = \frac{k T_-}{e} \ln \frac{\bar{v}_-}{\bar{v}_+} = \frac{k T_-}{2e} \ln \frac{T_- M_+}{T_+ M_-} \quad (80)$$

#### Space or Plasma Potential

If the potential is made more negative by decreasing  $V_w$  to 0,  $V_p - V_B = 0$  and  $V_p = V_B$ . This indicates that the center of the probe is at the same potential as the surrounding plasma and that there is no repulsion of either the electrons or the ions. Thus, the electrons and ions reach the probe in proportion to their normal rates of diffusion.

As a consequence of their greater mobility, the electrons will diffuse to the probe more rapidly than the ions and thus the electron current  $i_-$  is greater than the ion current  $i_+$ . This excess of  $i_-$  drives the plate potential lower than the wall potential. The negative value of  $i_p$  begins just below  $V_w$  and becomes more negative as  $V$  goes from  $V_w$  to zero. In theory all electrons can diffuse to the probe at  $V = 0$  because  $\exp(-Ve/kT)$  becomes unity and the electron current density becomes

$$j_- = eN_- \frac{kT_-}{2m_-} \quad (81)$$

The ion current density becomes

$$j_+ = eN_+ \frac{kT_+}{2M_+} \quad (82)$$

The net current density is given as

$$j = j_+ - j_- \quad (83)$$

#### The Positive Probe

As the probe potential is made positive, the ions are repelled and electrons are attracted by positive values of  $V$ . Since  $T_+$  for ions is usually low, the potential  $V$  needs to be only slightly positive to repel all of the ions and to give a negative space charge sheath. The absence of positive ion contribution to the probe current and the fact that electrons are being drawn to the probe by the positive value of  $V$ , causes an increase in negative probe current. The rate of increases will, however, be slower than the previous rate since the electron current is now space-charge-limited and changes as  $V^{3/2}/d^2$  instead of exponentially. With the negative values of  $V$ , which was discussed pre-

viously, the negative current was increasing exponentially, while with positive values it should only increase proportionally to the three-halves power of  $V$ . From this conclusion, the electron current for positive values of  $V$  is given as

$$i^- = \frac{e FN^- \bar{v}^-}{4} = e FN^- \sqrt{\frac{k T^-}{2\pi m^-}} = \frac{2F}{9} \sqrt{\frac{2e}{m^-}} \frac{V^{3/2}}{d^{-2}} \quad (84)$$

Similarly, the current is given as

$$j^- = e N^- \sqrt{\frac{k T^-}{2\pi m^-}} = \frac{2}{9} \sqrt{\frac{2e}{m^-}} \frac{V^{3/2}}{d^{-2}} \quad (85)$$

It is therefore seen that a plot of the current density against the potential  $V$ , will undergo an abrupt change in slope at  $V = 0$  and  $V_p = V_B$ . A curve of  $\ln i_p$  v.s.  $V_p$  which was taken from the data of Druyvesteyn (36), is shown in Figure 68a. This curve shows two lines of different slope. The slope of the lower line is given by Equation 75 which was derived for a Maxwellian velocity distribution. The slope of the upper line is given by Equation 84.

As stated previously, Equation 75 is only valid for a Maxwellian energy distribution. For a non-Maxwellian energy distribution, Equation 71 must be changed to

$$N_n = N^- \int f(v_n) dv_n \quad (86)$$

Druyvesteyn (36) found that in a low voltage arc, the slope of the lower line does not stay constant since the energy distribution of the electron is not Maxwellian. Figure 68b shows how the Druyvesteyn energy distribution differs from the Maxwellian energy distribution. If the energy

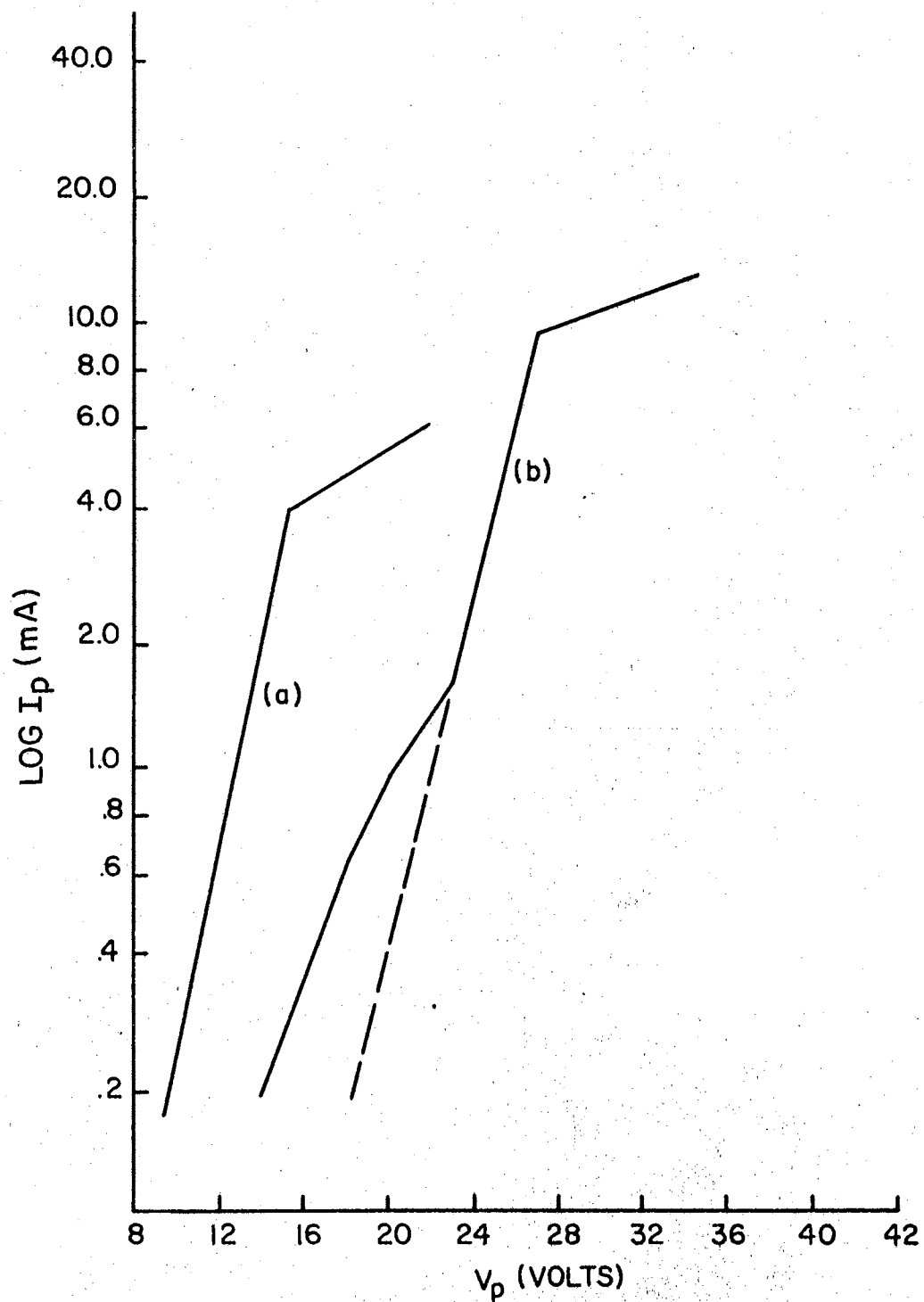


FIG. 68 CHARACTERISTIC PLOTS FOR  $\text{LOG } I_p$  RELATIVE TO  $V_p$ . AFTER DRUYVESTYEN.



distribution is of the Druyvesteyn form, the negative probe current is given as

$$i_- = e AN \sqrt{\frac{k T_-}{2\pi m_-}} \exp \left[ -\left(\frac{eV}{kT_-}\right)^2 \right]. \quad (87)$$

Thus the current-potential relationship is given as

$$\ln j_- = B' - \left(\frac{eV}{k T_-}\right)^2. \quad (88)$$

This relation should be compared with Equation 76 for the Maxwellian energy distribution.

#### Laser Induced Plasma

All of the discussions in this section has assumed a steady state discharge. The laser produced plasma "plume" is not in a steady state. It is a transient plasma from its production to its disappearance. As a consequence of this lack of steadiness, the variations in the probe current are probably very much influenced by both the density pulsations and the potential. Loeb (34) and Medicus (37) discuss the difficulties involved in probe measurements on plasmas in equilibrium. These difficulties and inaccuracies are compounded many times over for transient plasmas. Because of the transient nature of the laser produced plasma, the use of a probe to ascertain the energy spectrum of the carriers is completely out of the question. Instead of using probes, a quadrupole mass filter is employed to measure the velocity distribution of the ions that escape from the plasma. The use of the quadrupole mass filter will be discussed again later on in this chapter.

Before discussing the probe experiment on the plasma plume, it is

desirable to present our present understanding of the laser produced plasma. The available information from the Oklahoma State University plasma group, headed by Dr. F. C. Todd, consists of an approximate analytical solution for the phenomena by Peery (38), who was one of this group. Bruce (39) proved that a cold shell forms about a plasma that expands into a vacuum and the experimental observations of Brown (40) have confirmed the existence of this shell. The solution assists in the interpretation of the measurements by Willis (41) with a quadrupole mass filter on the ions that escape from the plasma.

Although the probe measurements made by the author on an unstable plasma do not offer significant hope for a major extension of the information on the subject, it is essential to the overall understanding of the conditions in the laser "plume" that these results be correlated with the existing experimental results from all other sources.

A tentative interpretation by Todd (42) of the preliminary measurements made by Willis with the quadrupole mass filter indicate that individual, dense plasmas cohere sufficiently so that they react with each other as different bodies and do not inter-diffuse into each other under all conditions. Thus, two plasmas do not necessarily merge into each other, but instead they tend to bounce off of each other like elastic bodies. The force required to make them merge has not been measured but is estimated to be a function of their ionization density and physical density.

In the discussion of the mechanical properties of plasmas by Todd, there are several references to the work by Willis. To assist in this discussion, two figures are included. The ordinate for the curve in Figure 69 is given in voltage drop across a resistor through which the

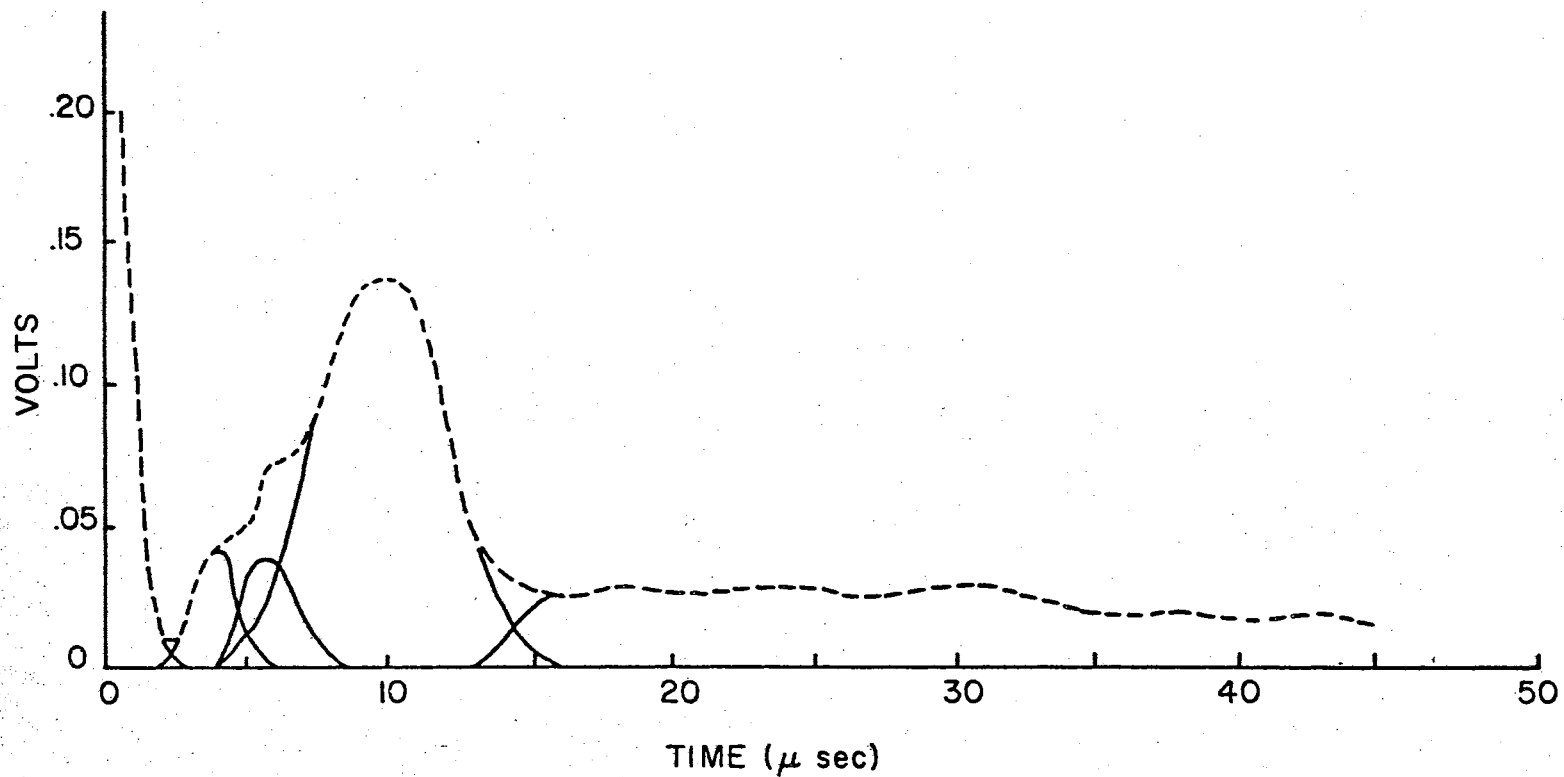


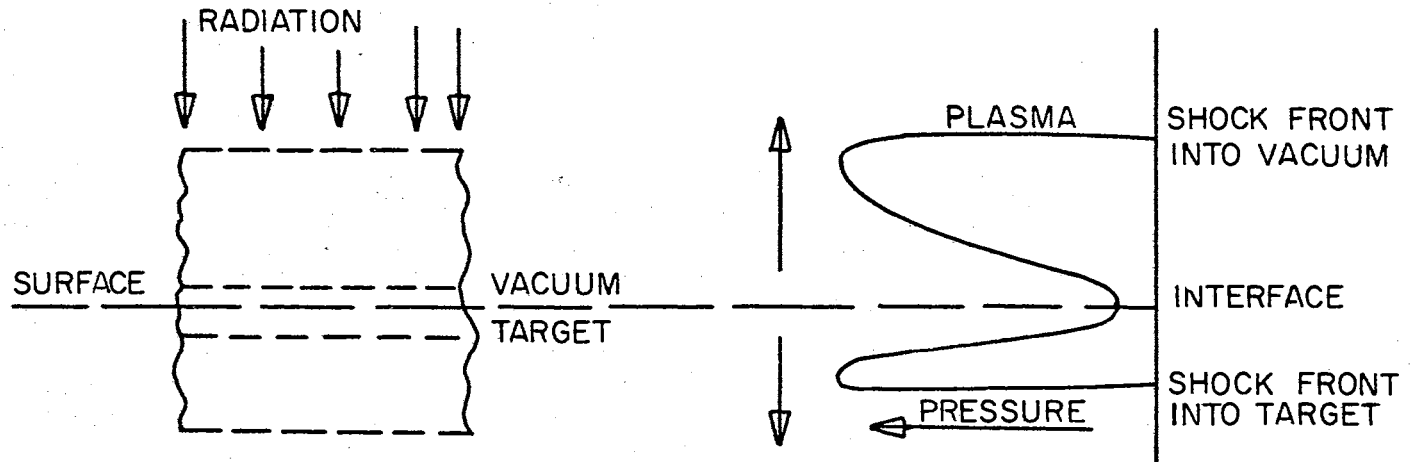
FIG. 69 INTENSITY VERSUS TIME OF ARRIVAL OF AL<sup>+3</sup> IONS. AFTER WILLIS.

current from the electron multiplier flows. As plotted, the voltage is proportional to the relative intensity of  $Al^{+3}$  ions that escape from the laser produced plasma and reach the electron multiplier. The dotted lines represent the actual data that was collected during the experiment. The solid lines represent groups of ions which were obtained by resolving the humped curve into separate peaks. The appearance of the separate peaks was not expected before the data was obtained. Their appearance is attributed to the exponential absorption of energy in the plasma and to the coherence of dense plasmas. The giant pulse from the laser is incident on the aluminum target and the resulting plasmas for approximately 30 nsec. The basis for the hypothesis is presented in Figure 70.

When the radiation of the surface is initiated, the radiation penetrates a predictable distance into the metal surface and gives energy to atoms in the volume that is under the radiated surface. The emitted vapor is ejected as a high pressure shock that propagates away from the surface. The shock is confined to the emitted vapor and is about a megabar, or more in pressure. A second shock is generated by the reaction to the ejected vapor and this second shock propagates in the opposite direction from the gaseous shock; i.e., it propagates into the metal of the target. This is illustrated by the sketch in Figure 70a.

The ejected vapor continues to absorb radiation from the giant pulse. Since the vapor, or plasma pulse is essentially separate from the base and since the absorption decreases exponentially with depth into the plasma; plasma sections (a) and (b) separate from each other. This is indicated by the sketches in Figure 70b. The separation mechanism for this relatively isolated gas pulse has the characteristics of separating masses inasmuch as momentum must be conserved. Since the most of

(A) PLASMA PRODUCTION AND ASSOCIATED SHOCKS



(B) FORMATION OF SEVERAL PEAKS

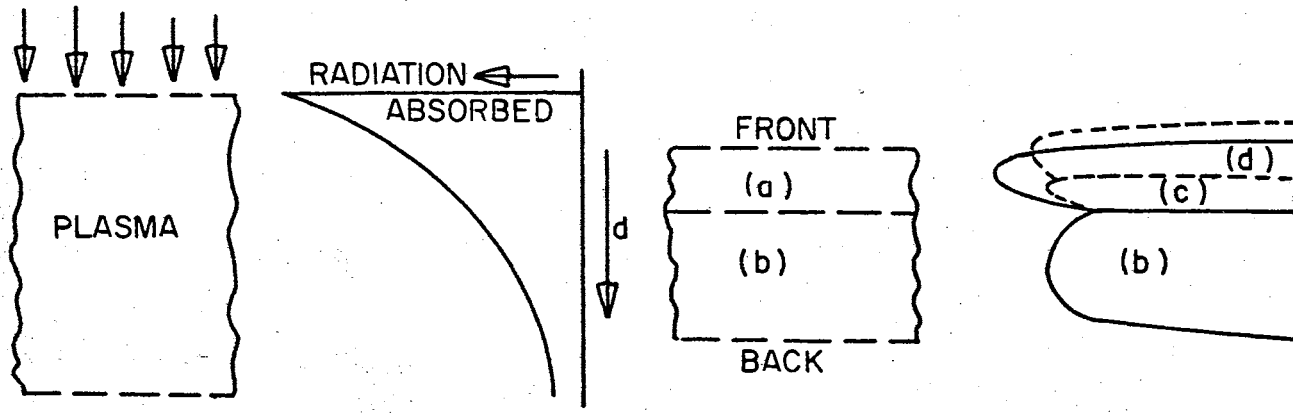


FIG. 70 PLASMA SEPARATION. AFTER TODD.

the energy is absorbed in the side of the plasma that is nearest to the impinging laser beam, this requires that plasma in (a) have greater energy and move faster than the partially shielded portion of the plasma that is nearest to the metal of the target. This part is designated as plasma (b). This explanation requires that the mass in (a) always be less than the slow moving plasma (b). Since the plasma coheres, considerable energy must be expended to produce the new plasma faces between the adjacent faces of plasmas (a) and (b).

Turbulence in the gas plasma may result in an apparent violation of the conservation of momentum inasmuch as the advanced peak (a) will be much smaller than predicted by the conservation of momentum. In order for the conservation of momentum to fail, turbulence must produce pockets in the plasma which have a radically different elasticity than the plasma as a whole. As a consequence, the plasma may not be considered to be a relatively homogeneous body. Failures of this type will always result in the material in the faster plasma (a) being less than expected. By this mechanism, there can never be a larger peak that is moving faster than the initial peak.

The plasma in the advance peak (a) is still absorbing radiation from the giant pulse so there may be another separation of the plasma (a) into two smaller parts, (b) and (c). The peak (b) will never be larger than peak (c) by the requirements of the conservation of momentum.

In the preceding section, the discussion is concerned with the hypothesis that the humps in the curve of ion density vs arrival time may be explained by a separation of the plasma into smaller plasmas. This consequence was attributed to the recognized cohesion of a dense plasma, the exponential absorption with depth of the incident energy in

the laser beam and the application of the conservation of momentum. There is another basic mechanism that could produce a break in the continuous development of the plasma. This second mechanism will be considered in this section.

An incident, monochromatic beam of light will enter a plasma, or will be reflected from it, depending on the natural frequency of the plasma oscillations. Plasma oscillations are an oscillation of the electrons with respect to the ions. The frequency of these oscillations are so high that the ions may be considered as fixed in space. The ions serve to neutralize the charge of the oscillating electrons. The condition for light penetration into the plasma is

$$\omega_{\ell} \gg \omega_p \quad (89)$$

where  $\omega_{\ell}$  is the frequency of the monochromatic light from the laser and  $\omega_p$  is the natural frequency of the oscillation of the electrons in the plasma. The condition for total reflection of light from the plasma is

$$\omega_{\ell}' \ll \omega_p \quad (90)$$

There is a change from absorption to reflection if the natural frequency of the plasma changes from below to above the frequency of the incident light from the laser.

Some considerations are given to the consequences of the occurrence of a variation of the plasma frequency from above to below the frequency of the laser light. These considerations are introduced to ascertain the possibility that reflection at the plasma surface may occur. If reflection occurs, it is desired to know the phenomena that might be ex-

pected in order to search for this phenomena in the observations and measurements on the laser "plume." The strongest evidence against the occurrence of reflection is from the computer program of Peery. The computer program for the production of a "plume" of plasma was programmed to calculate the plasma frequency and to show reflection if it should occur. Instead of reflection, the program indicated that the plasma became more and more penetrable by the laser light as the ionization increased and the plasma expanded. This evidence would be sufficient if the computer program were completely satisfactory. There is still some question about the program so other information must be considered.

To add to the hint from the computer program that reflection does not occur, it is necessary to investigate the structure of the "plume" and attempt to predict the effect of reflection of the laser beam. The first step is to consider the significant structure of the "plume." A double layer of charge forms at the surface of every plasma. If local thermodynamic equilibrium exists, the electrons move so much faster than the ions that they form a negative space charge outside the boundary of every plasma. Positive ions are attracted from the plasma to form a positive space charge on the boundary of the plasma that neutralizes the charge of the electron cloud. This positive charge prevents the escape of most of the electrons in the negative space charge sheath. This double layer exists on the outside of the plasma on both the irradiated and non-irradiated surfaces. In addition, the expansion of the non-irradiated surface into the vacuum results in the formation of a cold shell at the surface of the plasma. If the consequences of this observation is considered, the cold plasma surface will allow ions and electrons to escape from the plasma with about the same velocity and inten-



sity in all directions. The "cold" surface cannot occur on the surface of the plasma that receives radiation.

If total reflection of the incident laser pulse occurs, it will be from the irradiated surface of the plasma which will be from the portion of the plasma which is directly below the double layer at the surface of the plasma. The energy input to the plasma is a maximum at that position and the density of ionization must also be a maximum. The frequency of the plasma oscillations is the greatest where the density of electrons is the greatest. This is shown by the equation for the natural frequency of the plasma which is

$$\omega_p = \left( \frac{4 \pi n_e q_e^2 c^2}{m_e} \right)^{1/2} . \quad (91)$$

In this equation,  $\omega_p = 2\pi f$ , where  $f$  is the frequency of the plasma,  $n_e$  is the number of free electrons per  $\text{cm}^3$ ,  $q_e$  is the charge on an electron,  $c$  is the velocity of light and  $m_e$  is the mass of an electron. If there is total reflection in the substrate, only the atoms and ions in the double layer will receive energy to escape from the plasma. These ions will be fairly uniformly scattered in all directions from the elevated central core of the radiated surface. The geometry of the situation will insure uniform scattering.

The radiated core should be higher, physically, than the partially irradiated rim which surrounds it. The radiation which is outside of the theoretical image will decrease rapidly to zero. The rim of vapor about the central core cannot be as hot, or extend as far above the base plate as the core. Radiation pressure from the laser beam is not expected to produce much effect on ions which are moving at roughly  $\frac{1}{2}$  to  $1 \times 10^7$  cm. per second.

In contrast, consider that total reflection of the beam of light from the plasma surface never occurs. All of the laser radiation penetrates into the laser "plume" where it is absorbed exponentially with depth. Since the period of radiation is only 30 nanoseconds in duration, the vacuum-metal vapor interface can only be irregular on a microscopic scale. With exponential absorption of the radiation with depth of penetration into the plasma, most high speed ions will come from below the surface. The escape of these ions at right angles to the direction of radiation would be a practical impossibility. The escaping high energy ions should be primarily in a cone that is centered about the vertical axis. This assumed mechanism for the production of the ions below the surface of the irradiated region of the plasma would produce a fairly well defined cone in which light from the recombination is to be expected. As indicated by Figure 71 there does appear to be a well defined cone. With reflection from the surface of the plasma, only a cold, high rim of dense gas could give the observed effect. This high rim of a cold gas does not appear to be a mechanism that total reflection could produce. It is also not feasible for the irradiated region to be depressed by light pressure, particularly when the energy of the ions is considered.

The photograph in Figure 71, which covers the period of production, development and decay of the plasma "plume" was taken with the camera lens opened before the experiment and closed after everything is over. The laser produced "plume" projects upward from the base plate with a slightly converging column and then expands into a less dense plasma which finally fades out at the top. There is, however, a faint background of illumination with the more intense illumination above the

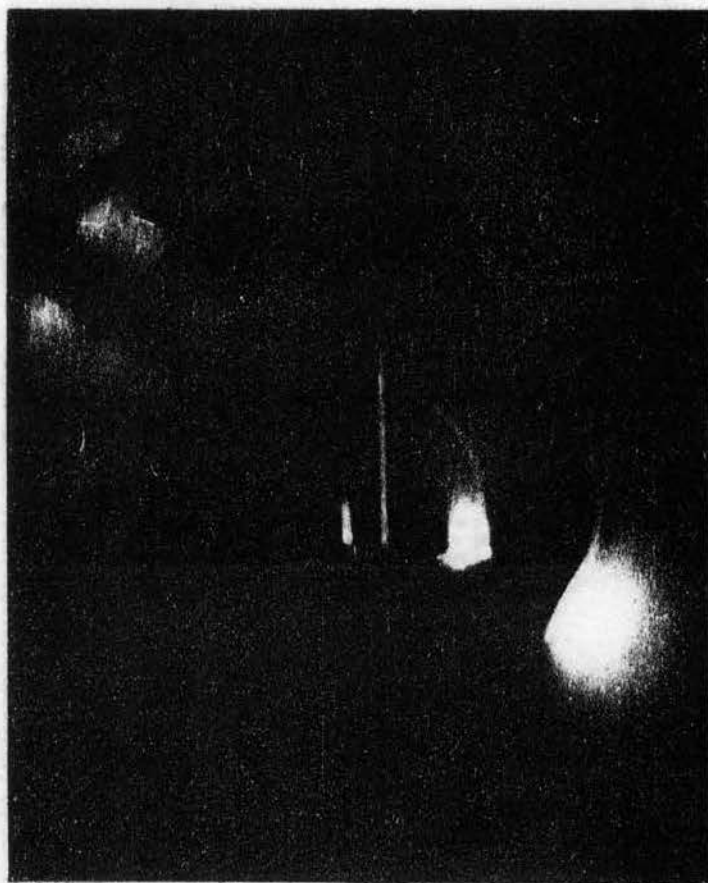


Figure 71. Photograph of Laser Induced Plasma Plume

clearly defined edge of a cone that is indicated on the sketch. Below this boundary, the radiation background is less dense than it is above. This clearly defined boundary does not intersect the edge of the plasma on the target plate. It is not clear whether the plasma has expanded and the intercept is with the original plasma-plate edge, or whether it actually intercepts the plasma column at a position above the target plate. Either could be possible and would require no additional discussion. The irradiated area is about 1 mm. in diameter. The light from the giant pulse is directed vertically down in Figure 71.

The preceding discussion is intended to indicate that total reflection of the incident giant pulse by the highly ionized plasma is not probable. The photograph presents evidence which appears to confirm continuous absorption and which would be very difficult to explain on the basis of occasional periods of total reflection. The appearance of added, faster peaks in the ion velocities that are measured by the quadrupole mass filter also appears to require an explanation of the basis of continuous absorption during the entire period of radiation.

#### Probe Experiment

An experiment was performed in which probes were mounted so the expanding plasma would pass the probes. At a minimum, the experiment was expected to show the average rate of expansion of the plasma. It was hoped that it might show some of the structure of the plasma. Both of these expectations were fulfilled. It does not give significant information on the temperature and density according to the Langmuir theory. It does indicate something about the temperature for it shows the arrival time of the expanding plasma at the probe.

The experiment employed four probes. Each probe was designed as illustrated in Figure 72. The four probes were symmetrically arranged around the giant pulse impact area as shown in Figure 73. The direction of polarization of the incident laser beam and the elliptical shape of the target roughened area are also shown in the last figure. The object of the experiment was to monitor, with an oscilloscope, the probe potential as a function of time. The schematic for the electrical circuit is presented in Figure 74. The power source that supplied a potential to the probe was reversible in polarity and variable in voltage. The energy from the laser was kept at approximately 8 joules for each pulse during the experiment and the experiment was carried out in a vacuum of approximately  $5 \times 10^{-6}$  Torr. After each shot, the target was rotated by means of a vacuum feedthrough so that a fresh surface could be used for the next probe measurement. The data, the probe measurements is shown in Figures 75-91.

In analyzing the data in Figures 75-91, it is interesting to note that practically all of the curves exhibit three major peaks. It is also interesting to note that the first peak occurs at about the same time, regardless of the angle between the probe and the target face. Only electrons which approach close to the probe, or are collected by the probe could cause a negative peak, regardless of the probe potential. For this reason, the first peak is thought to be caused by electrons that form the front edge of the plasma from the target. The electron peak is always followed by peaks from the neutral plasma. The data indicates a most probable average velocity of the plasma front of about  $1.6 \times 10^7$  cm/sec.

The emphasis on the plasma front is explained in this manner. A

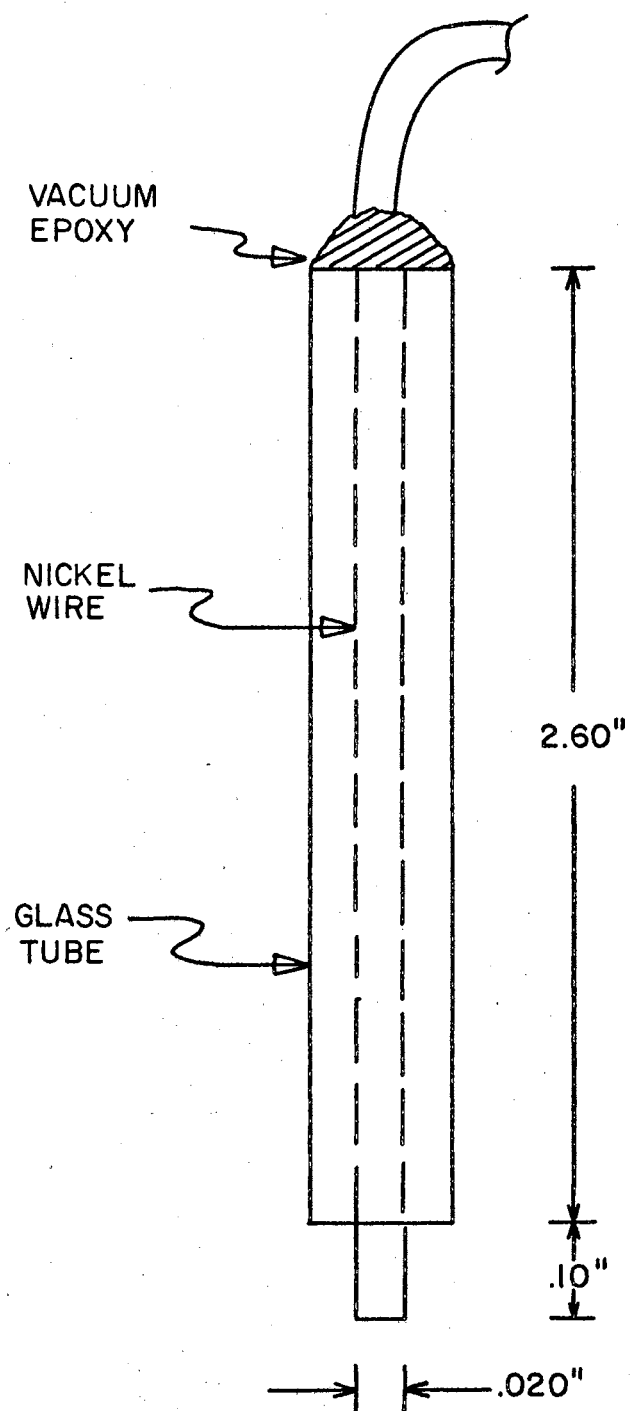


FIG.72 EXPERIMENTAL PLASMA PROBE

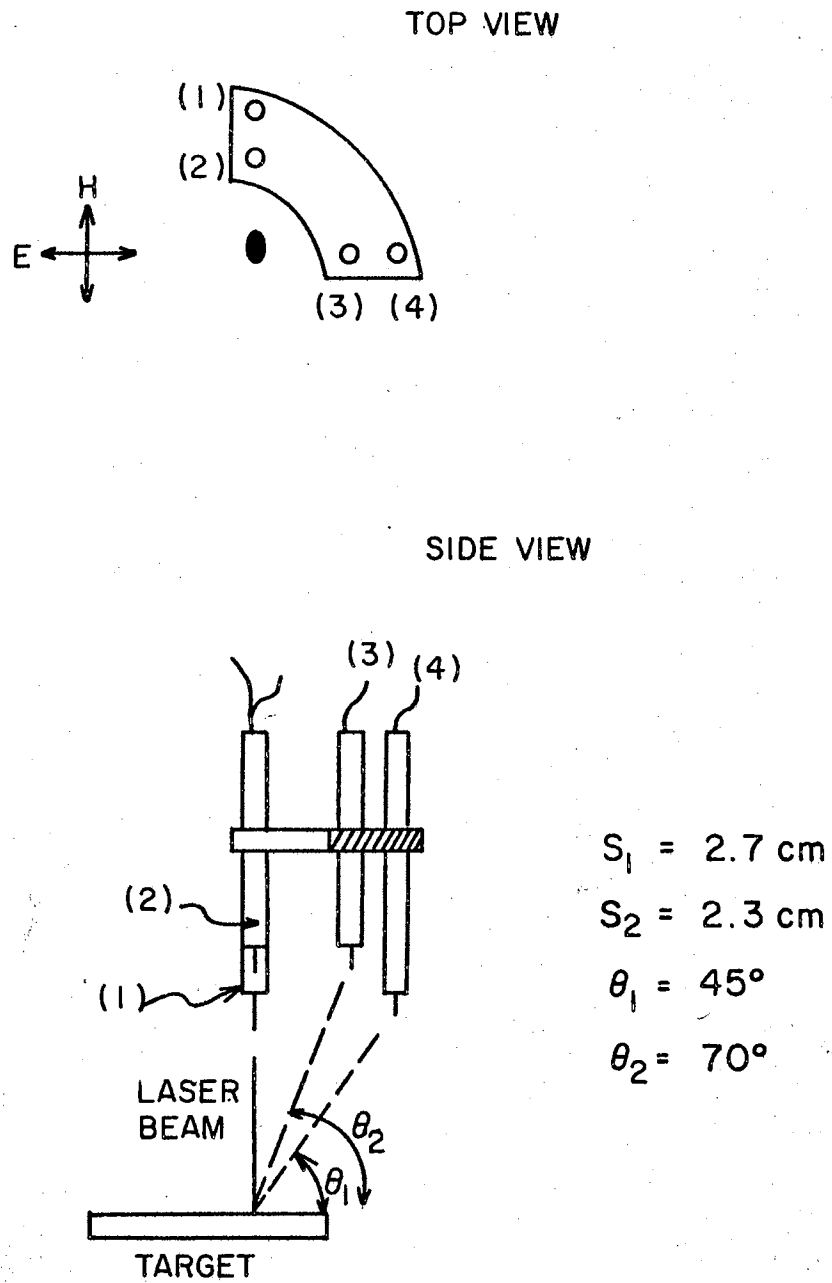


FIG. 73 EXPERIMENTAL PROBE ARRAY

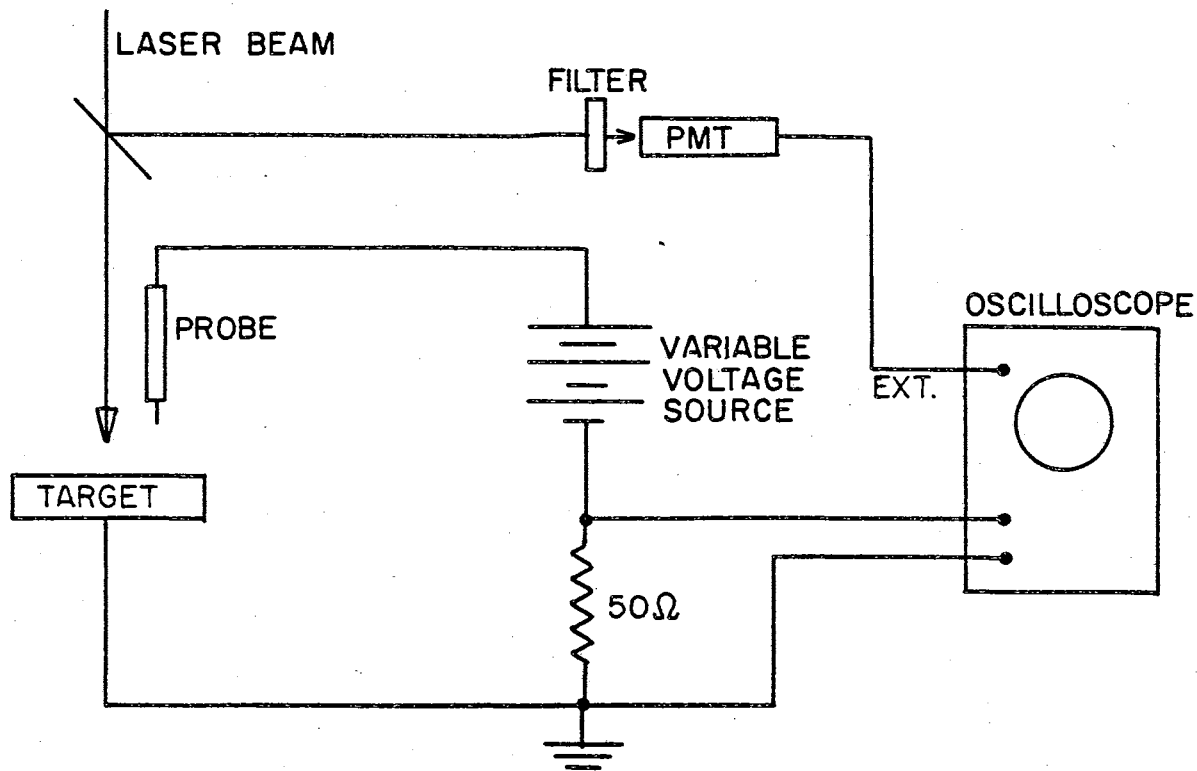
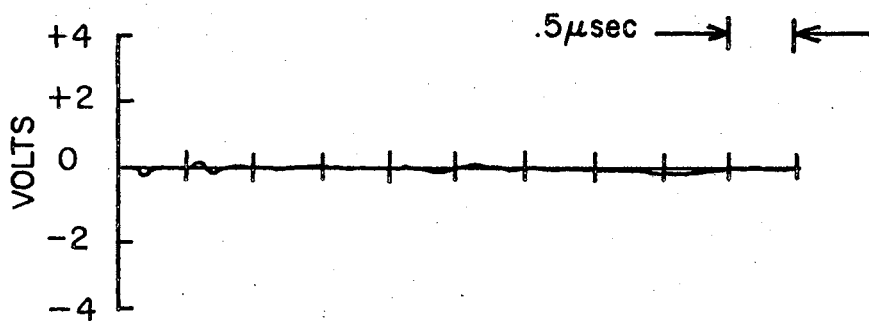
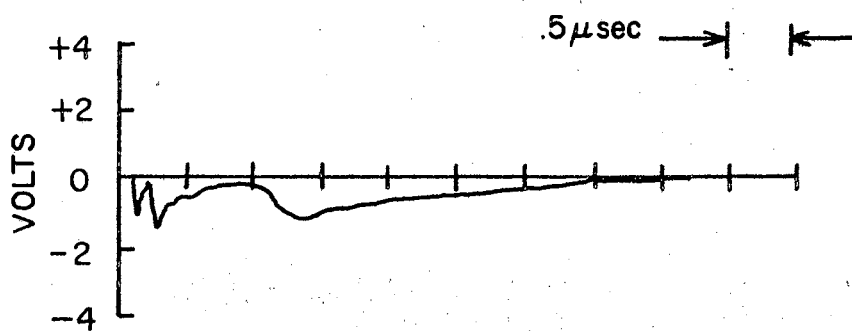
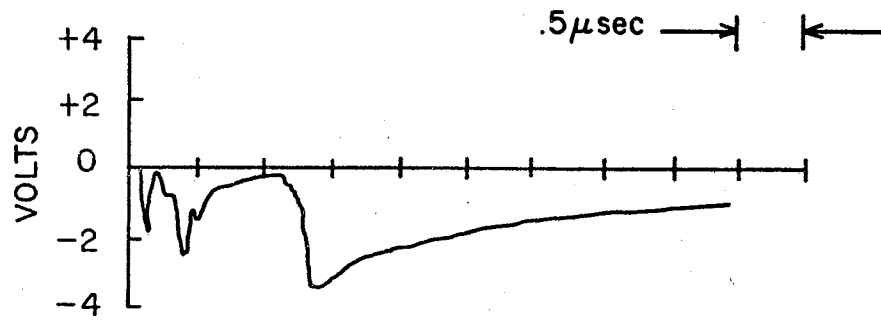
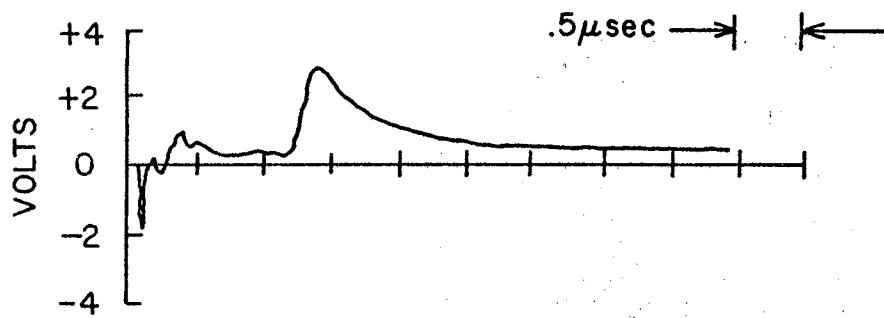
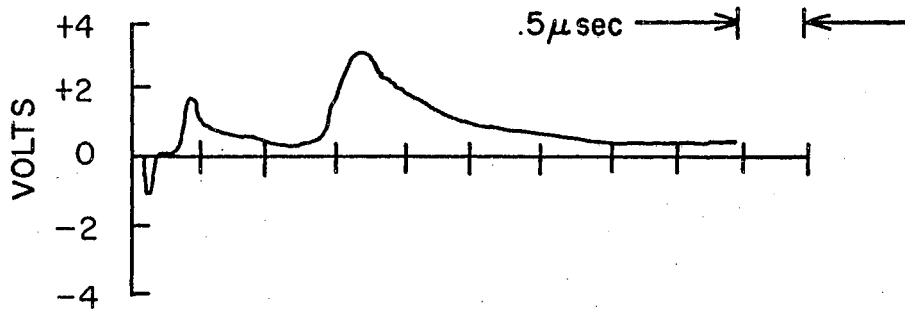
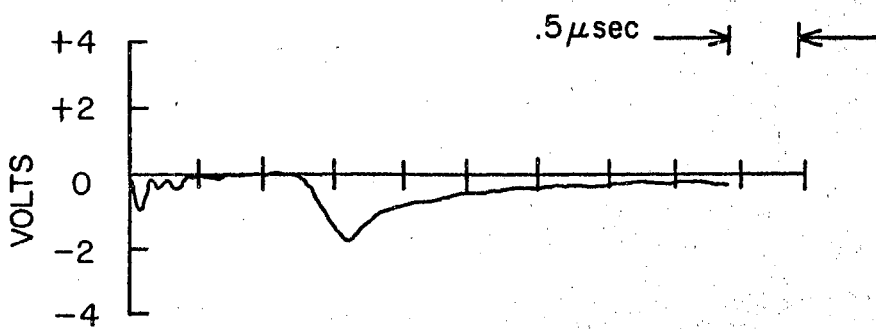


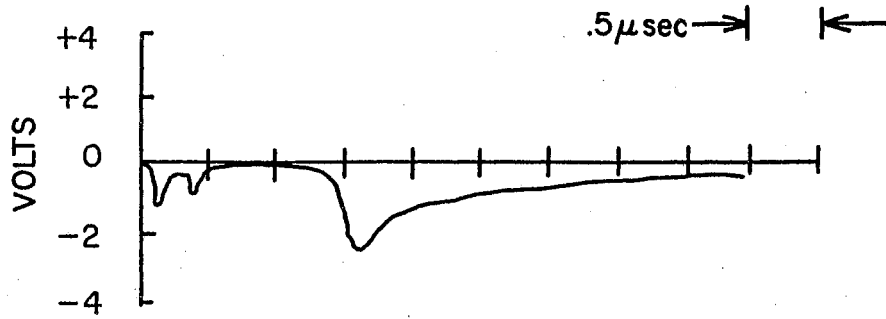
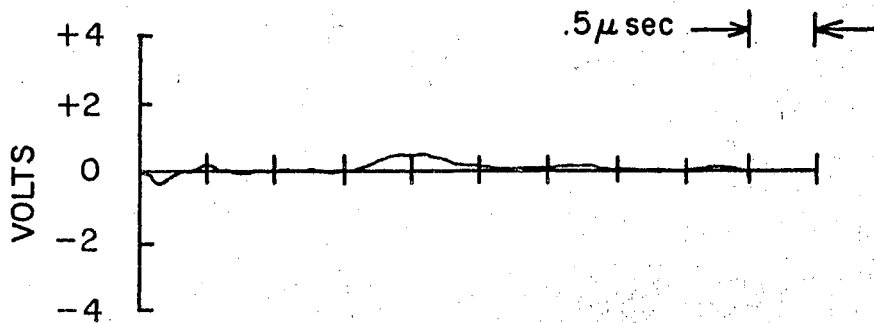
FIG. 74 SCHEMATIC DIAGRAM OF PROBE EXPERIMENT

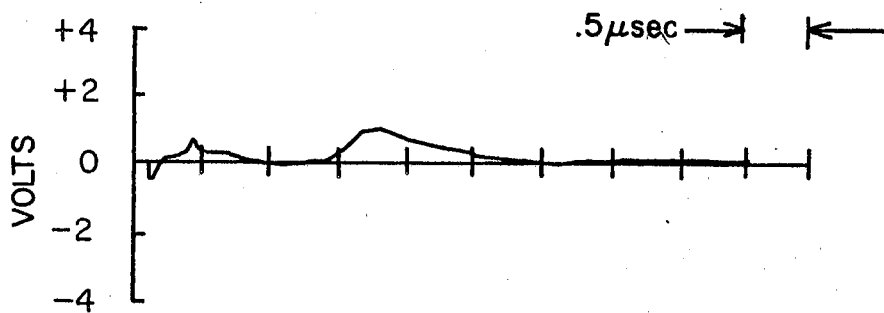
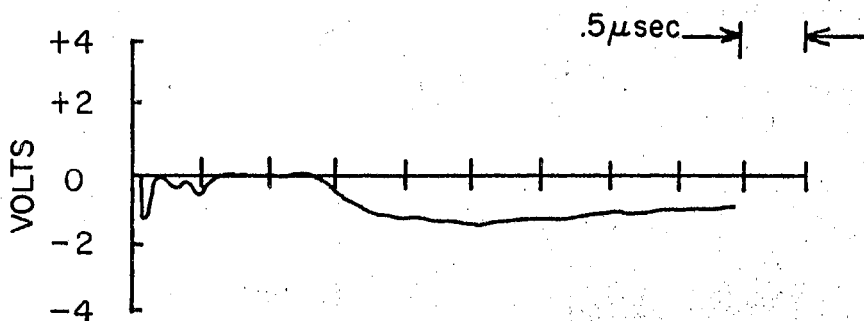


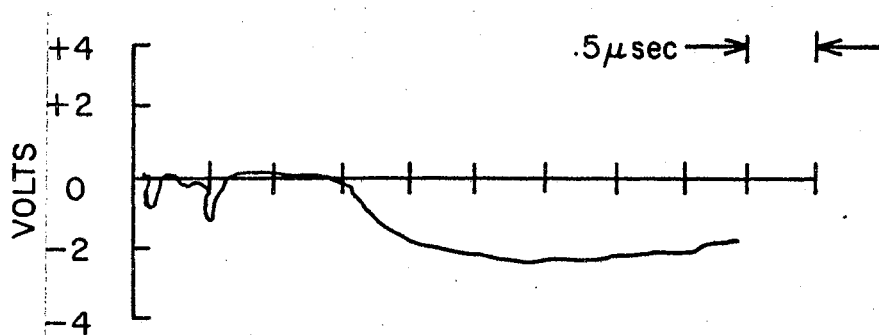
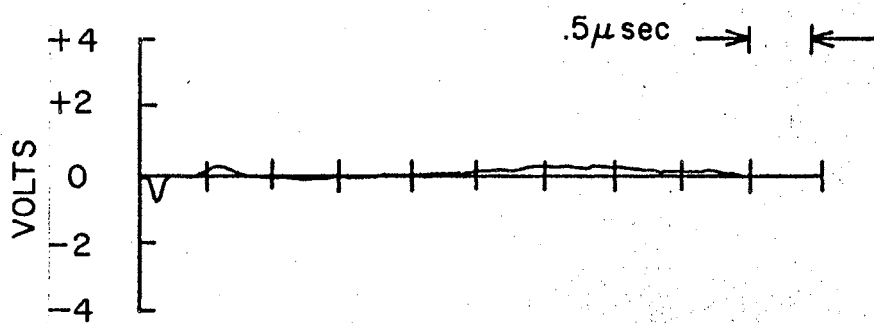
FIG. 75 PROBE NO.2,  $V_p = 0.0$  VDCFIG. 76 PROBE NO.2,  $V_p = +5.0$  VDC

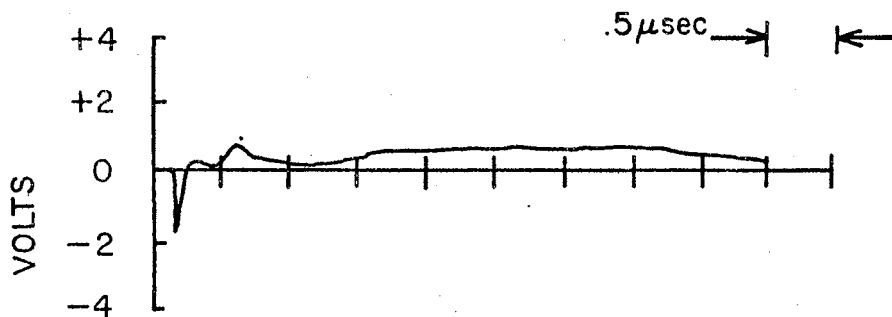
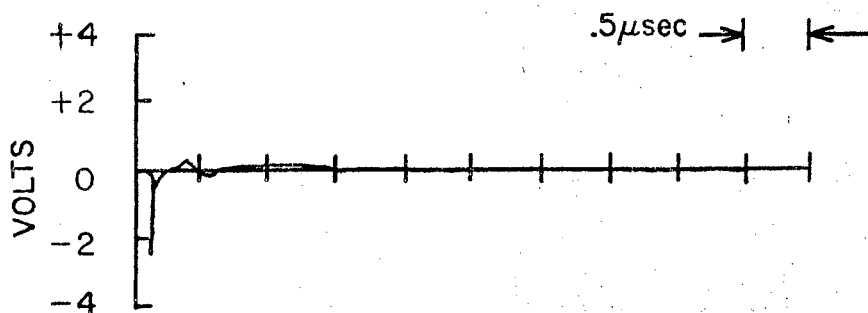
FIG. 77 PROBE NO.2,  $V_p = +10.0$  VDCFIG. 78 PROBE NO.2,  $V_p = -5.0$  VDC

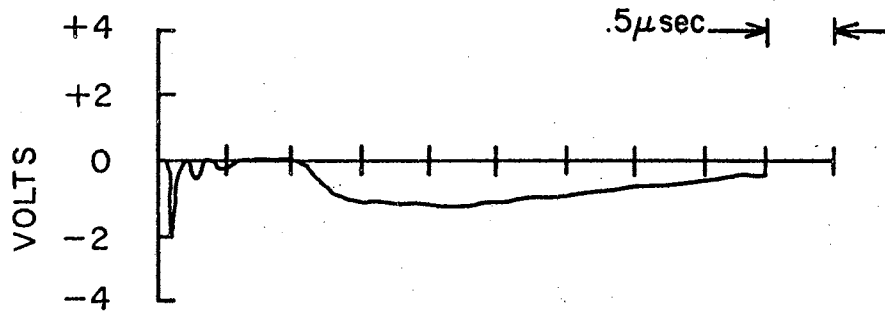
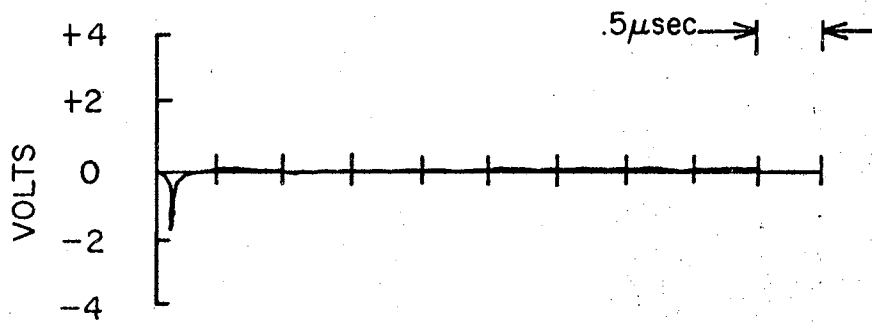
FIG. 79 PROBE NO.2,  $V_p = -10.0$  VDCFIG. 80 PROBE NO.3,  $V_p = +5.0$  VDC

FIG. 81 PROBE NO.3,  $V_p = +10.0 \text{ VDC}$ FIG. 82 PROBE NO.3,  $V_p = -5.0 \text{ VDC}$

FIG. 83 PROBE NO. 3,  $V_p = -10.0$  VDCFIG. 84 PROBE NO. 1,  $V_p = +5.0$  VDC

FIG. 85 PROBE NO.1,  $V_p = -10.0\text{VDC}$ FIG. 86 PROBE NO.1,  $V_p = -5.0\text{VDC}$

FIG. 87. PROBE NO.1,  $V_p = -10.0\text{VDC}$ FIG. 88 PROBE NO. 4,  $V_p = +5.0\text{VDC}$

FIG. 89 PROBE NO.4,  $V_p = +10.0$  VDCFIG. 90 PROBE NO.4,  $V_p = -5.0$  VDC



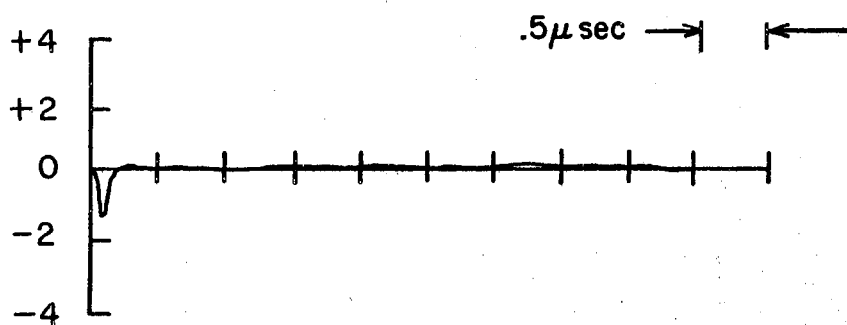


FIG. 91 PROBE NO.4,  $V_p = -10.0\text{ VDC}$

cloud of electrons cannot leave the plasma because of the electric field between the electrons and the ions that they are trying to leave. The electrons travel so much faster than the ions that the electrons are always on the front edge and they are followed by positive ions that neutralize the charge of the electrons. The net result is a double layer of charge with a negative charge in front that is followed by a positive charge. The double layer exists in a vacuum and in a gas. The propagation of the double layer was recognized many years ago. In gases, it is called ambipolar diffusion and its explanation was proposed by Cobine (43) in 1929.

The second and third peaks are found to occur at different times and thus have an average velocity which is dependent on the probe positions with respect to the impact of the laser beam on the target. The second and third peaks were, at first, thought to be a result of positive ions. If this were true, these peaks would not be reversed in polarity when the probe voltage is reversed. It would also not be logical that these peaks would diminish in size as the probe voltage became more positive. As a consequence of the performance, it is believed that the second and third peaks indicate the charge that is drawn from a neutral plasma that may be fluctuating in density. The plasma is conducting and extends from the laser "plume" to the probe so charge of either sign may be extracted from the plasma and may be made to flow through a closed circuit by an appropriate source of e.m.f.

It is interesting at this point to calculate the threshold wavelength for which photoelectrons could be emitted from the surface of the probe. The equation to be used is given as

$$\lambda_0 < \frac{hc}{W} \quad (92)$$

where  $\lambda_0$  is the threshold wavelength,  $h$  is Planks constant,  $c$  is the speed of light and  $W$  is the work function of nickel. Equation 92 becomes,

$$\lambda_0 \leq \frac{(4.12 \times 10^{-16} \text{ eV} - \text{sec})(3 \times 10^{10} \text{ m/sec})}{(4.34 \text{ eV})} \quad (93)$$

$$\lambda_0 \leq \frac{12.36 \times 10^{-6} \text{ eV} - \text{m}}{4.34 \text{ eV}} \quad (94)$$

$$\lambda_0 \leq 2847 \text{ \AA} . \quad (95)$$

Therefore, light emission from the plasma which falls in the region below  $2847 \text{ \AA}$  could cause photoelectron emission from the probe. However, it is the author's conviction that the amount of photoelectron emission from the probe is negligible since there is no indication of a positive peak at the beginning of the trace. Similar calculations show that there are probably photoelectrons emitted from the target surface also. These are also considered negligible.

It is evident from the probe data that the electron density of the laser induced plasma varies considerably with time and most likely, space. As a consequence, the laser induced plasma can be described as a rarified plasma with "lumps" or regions of high electron and ion densities.

The important features of the probe curves are summarized in Table XXI. The probe curves definitely show that the laser induced plasma is not symmetrical about the point of laser beam impact. The average maximum velocity for the different probes is given in Table XXII. Notice that for the first peak, the average maximum velocity for probes 1 and 4 is greater than for probes 2 and 3. The two main differences between probes 1, 2, 3 and 4 are that probes 1 and 4 are farther away from the

TABLE XXI  
TABULATION OF PROBE DATA

Probe No.	2	2	2	2
Probe voltage (V)	5.0	10.0	-5.0	-10.0
Voltage, 1st peak (V)	-1.2	-2.0	-2.0	1.2
Start, 1st peak ( $\mu$ sec)	0.10	0.10	0.10	0.10
Velocity, 1st peak (cm/sec x $10^7$ )	2.30	2.30	2.30	2.30
Voltage, 2nd peak (V)	-1.6	-2.8	1.0	1.6
Start, 2nd peak ( $\mu$ sec)	0.20	0.20	0.30	0.30
Velocity, 2nd peak (cm/sec x $10^7$ )	1.20	1.20	0.77	0.77
Voltage, 3rd peak (V)	-1.4	-3.6	2.8	3.2
Start, 3rd peak ( $\mu$ sec)	1.10	1.10	1.20	1.40
Velocity, 3rd peak (cm/sec x $10^7$ )	0.21	0.21	0.21	0.16
Probe No.	3	3	3	3
Probe voltage (V)	5.0	10.0	-5.0	-10.0
Voltage, 1st peak (V)	-1.0	-1.2	-0.4	-0.6
Start, 1st peak ( $\mu$ sec)	0.10	0.10	0.10	0.10
Velocity, 1st peak (cm/sec x $10^7$ )	2.30	2.30	2.30	2.30
Voltage, 2nd peak (V)	-0.4	-0.4	0.4	0.6
Start, 2nd peak ( $\mu$ sec)	0.30	0.35	0.35	0.35
Velocity, 2nd peak (cm/sec x $10^7$ )	0.77	0.66	0.66	0.66
Voltage, 3rd peak (V)	-1.0	-2.8	0.6	0.8
Start, 3rd peak ( $\mu$ sec)	1.30	1.30	1.60	1.40
Velocity, 3rd peak (cm/sec x $10^7$ )	0.18	0.18	0.14	0.16
Probe No.	1	1	1	1
Probe voltage (V)	5.0	10.0	-5.0	-10.0
Voltage, 1st peak (V)	-1.6	-1.0	-0.8	-2.0
Start, 1st peak ( $\mu$ sec)	0.10	0.10	0.10	0.10
Velocity, 1st peak (cm/sec x $10^7$ )	2.70	2.70	2.70	2.70
Voltage, 2nd peak (V)	-0.6	-1.4	-0.4	-0.6
Start, 2nd peak ( $\mu$ sec)	0.45	0.50	0.50	0.45
Velocity, 2nd peak (cm/sec x $10^7$ )	0.60	0.54	0.54	0.60
Voltage, 3rd peak (V)	-1.4	-2.6	0.2	0.6
Start, 3rd peak ( $\mu$ sec)	1.40	1.40	1.50	1.3
Velocity, 3rd peak (cm/sec x $10^7$ )	0.19	0.19	0.18	0.21
Probe No.	4	4	4	4
Probe voltage (V)	5.0	10.0	-5.0	-10.0

TABLE XXI (Continued)

Voltage, 1st peak (V)	-1.1	-1.0	-1.6	- 1.2
Start, 1st peak ( $\mu$ sec)	0.10	0.10	0.10	0.10
Velocity, 1st peak (cm/sec x $10^7$ )	2.70	2.70	2.70	2.70
Voltage, 2nd peak (V)	-0.2	-0.3	0.0	0.0
Start, 2nd peak ( $\mu$ sec)	0.35	0.35	----	----
Velocity, 2nd peak (cm/sec x $10^7$ )	0.77	0.77	----	----
Voltage, 3rd peak (V)	-0.3	-1.2	0.0	0.0
Start, 3rd peak ( $\mu$ sec)	1.00	1.00	----	----
Velocity, 3rd peak (cm/sec x $10^7$ )	0.27	0.27	----	----

TABLE XXII

AVERAGE MAXIMUM VELOCITY FOR DIFFERENT PROBES

Probe No.	Velocity, 1st Peak	Velocity, 2nd Peak	Velocity, 3rd Peak
2	$2.3 \times 10^7$	$.96 \times 10^7$	$.19 \times 10^7$
3	$2.3 \times 10^7$	$.69 \times 10^7$	$.16 \times 10^7$
1	$2.7 \times 10^7$	$.57 \times 10^7$	$.19 \times 10^7$
4	$2.7 \times 10^7$	$.77 \times 10^7$	$.27 \times 10^7$

target area and they are at a lower angle to the target face. This then may indicate that the velocity of the electrons, which caused the first peak, is dependent on the angle of ejection. The average maximum velocity for the second peak is shown in Figure 92. Along the +y-axis, the velocity of the plasma is greater at an angle of 70 degrees than it is at 45 degrees. While along the +x-axis, the velocity of the plasma is greatest at an angle of 45 degrees. The average maximum velocity for the third peak is shown in Figure 93. In all cases the third peak is considerably slower than the second peak. Along the +y-axis, the velocity of the plasma is about the same for both the 45 degree and 70 degree probes. However, along the +x-axis the plasma velocity is greatest at an angle of 45 degrees. This also occurred along the +x-axis for the second peak. Besides the velocity of the peaks being non-symmetrical about the impact area, it is also interesting to note the differences in the shape and amplitude of the probe curves. The third peak of probes 2 and 3 are similar and are characterized by a rather fast rise-time and fall-time compared to the third peak of probes 1 and 4 which have a rather slow rise-time and fall-time. The amplitude of third peak for probes 2 and 3 are approximately the same, whereas the third peak for probes 1 and 4 are considerably different.

#### Light Emission From the Plasma

In order to obtain more information about the laser induced plasma, the light emitted from the plasma was monitored. One experiment which was carried out in conjunction with an experiment performed by H. W. Willis, was to monitor the light emission from the laser induced plasma with a 10 state electron multiplier. The experiment was set up to

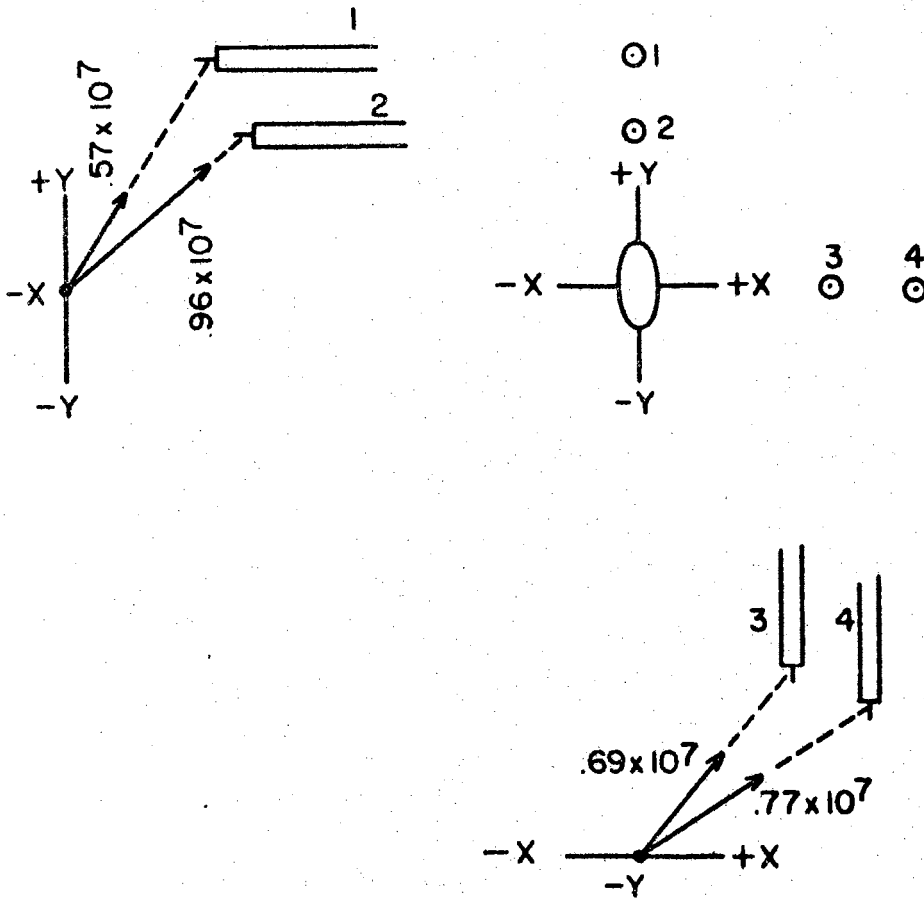


FIG. 92 VELOCITY VECTORS FOR SECOND PEAK



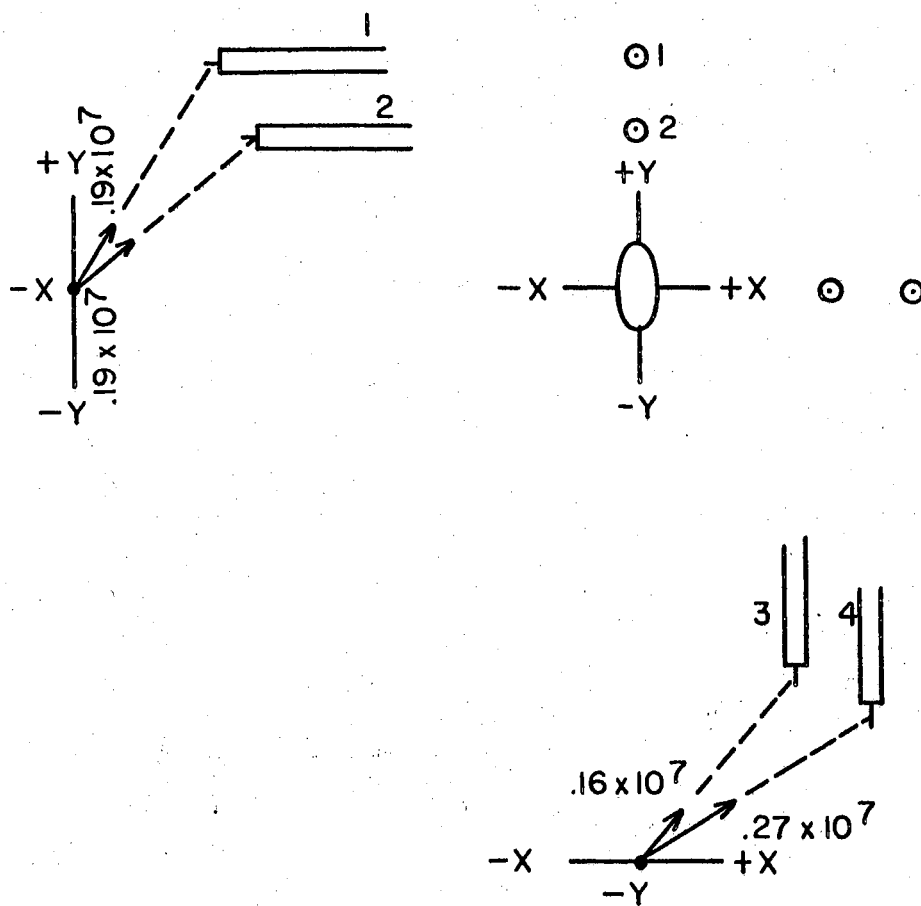


FIG. 93 VELOCITY VECTORS FOR THIRD PEAK

measure both the light emitted from the plasma and the relative number of ionic species produced in the plasma. The different ionic species are measured with the aid of a quadrupole mass filter that was constructed by H. W. Willis. The experimental layout is shown in Figure 94. The electron multiplier for the detection of ions has a cathode that is normally used to increase the number of electrons by secondary electron emission. This cathode surface also emits electrons when photons of high energy are incident on it. By means of a cut-off filter, it has been proved that the cathode will not respond to photons with an effective wave length that is longer than  $3900 \text{ \AA}$ . Repeated measurements with the electron multiplier have shown that there is an intense burst of ultra-violet light, the light decays to zero in very close to  $2\frac{1}{2}$  microseconds with relatively small deviations from experiment to experiment. This light comes from the transitions from ions of all charges to ions with less excitation, or to neutral atoms. It is a little surprising that this process terminates within  $2\frac{1}{2}$  microseconds. Figure 95 shows a typical trace of the light intensity of the plasma as a function of time.

Another experiment was designed to obtain the vacuum ultra-violet spectra of the laser produced aluminum plasma. The experimental layout is shown in Figure 96. The experiment was carried out at a vacuum of  $10^{-6}$  torr with a one meter, grazing incidence spectrograph that was built in our laboratory by Payne (44) and was used by Carpenter (45) for aluminum spark discharge experiments. The spectrograph is capable of recording lines in the wavelength region from  $100 \text{ \AA}$  to  $1400 \text{ \AA}$ . A spectra was obtained by Carpenter for which the source was an aluminum spark discharge. The film was exposed approximately 150 times to the

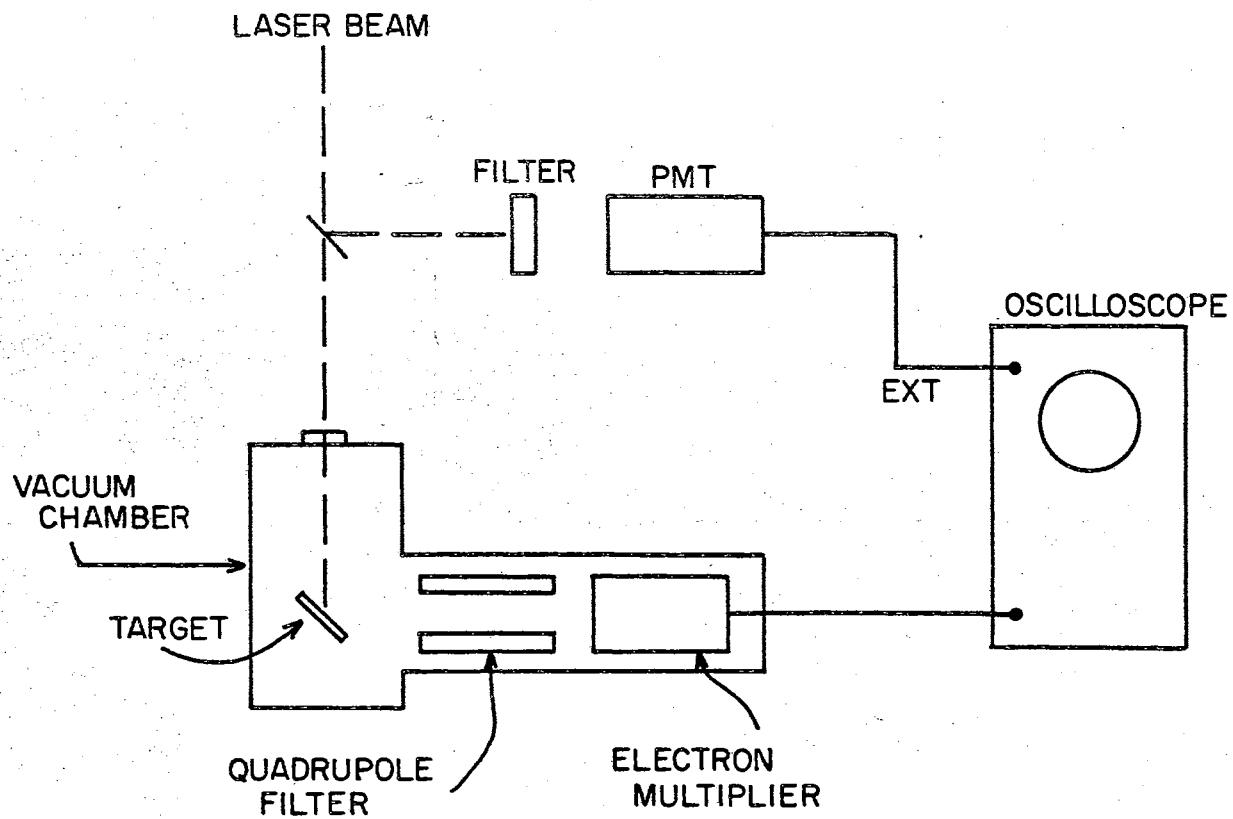


FIG. 94 EXPERIMENTAL ARRANGEMENT FOR LIGHT EMISSION MEASUREMENT

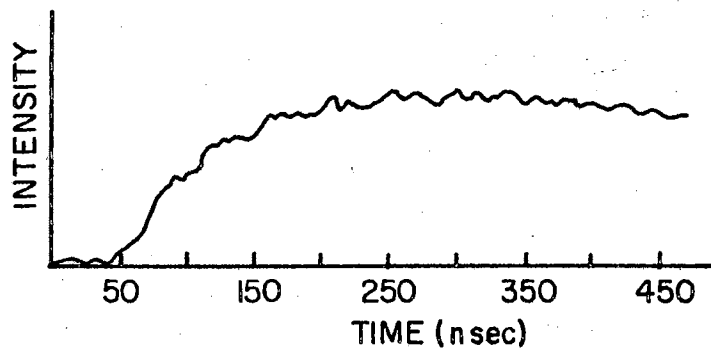
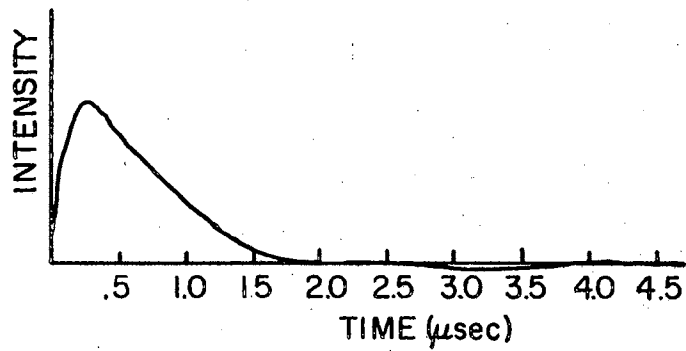


FIG. 95 LIGHT INTENSITY IN U.V. VERSUS PLASMA FORMATION TIME

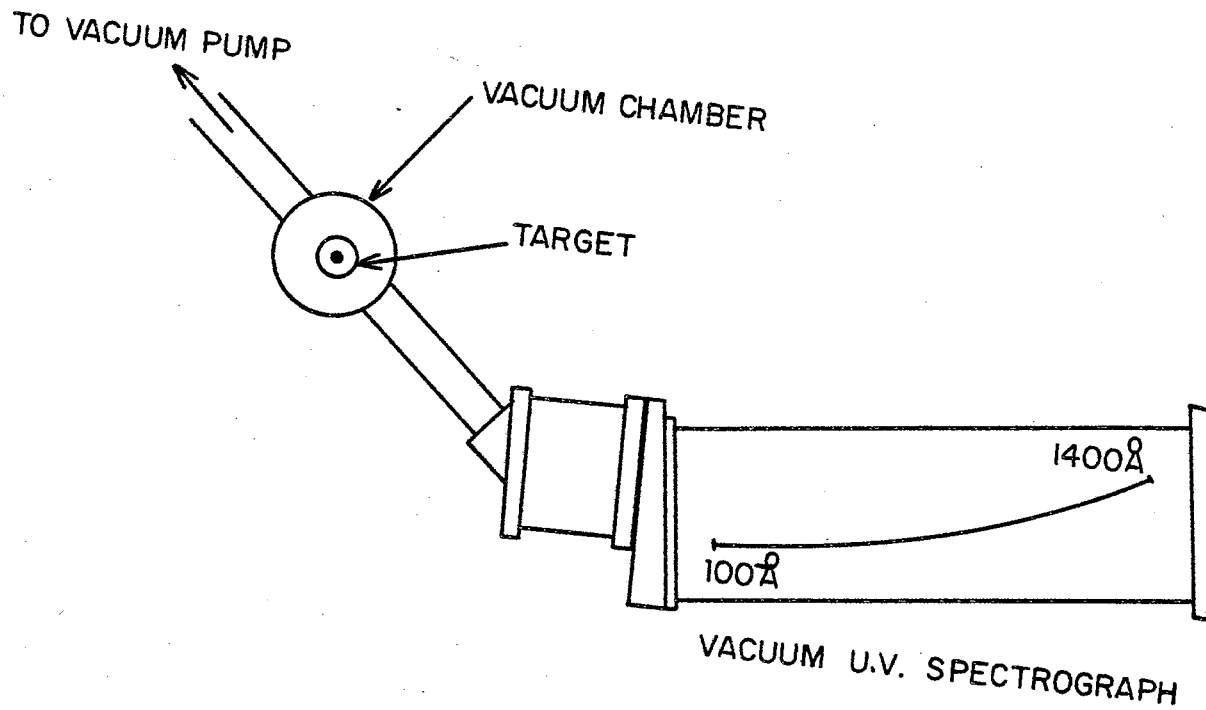


FIG. 96 VACUUM ULTRAVIOLET SPECTROGRAPH EXPERIMENT

laser induced plasma before the film was developed. After developing the film it was found that there were no lines visible on the film. The experiment was then repeated with the same results. It was then theorized that the reason for failure was that the light emitted from the laser produced plasma had to travel too great a distance to reach the film. A solution to this problem might be to move the entrance slit of the spectrograph closer to the plasma and to use a faster film, i.e., Kodak Pathe SC.7 which is reported to be approximately ten times faster than the Kodak for ultra-violet film used in the experiment. Another solution would be to use small detectors in place of film. With the recent development of small u.v. detectors such as those built by Bendix Corporation, this approach seems quite applicable. The use of a detector would also enable the investigator to look at the intensity of a single line as a function of time.

The measurements with the probes do not provide significant new evidence. At the same time, they provide much information that tends to confirm the hypothesis that is proposed to explain the concept that has been developed from the available evidence. Additional measurements with different equipment are necessary and desirable.

## CHAPTER VII

### SUMMARY AND CONCLUSION

This final chapter is written in an attempt to summarize the important points of the experimental work completed by the author, and to suggest some possible improvements which could be made to the experimental equipment and to the method of data collection.

#### General Summary

The first important aspect of the experimental work was the modification of the twin ruby laser to produce a reliable experimental instrument. Reliability was achieved after the optical pumping, triggering and aligning methods were evaluated and modified. Introduction of the passive Q-switch element enabled the twin ruby laser to produce giant pulses having an energy of 15 joules and a duration of 30 nsec. Along with the modification of the laser came the design and construction of the energy and waveform measuring instrumentation. Energy measurements of the attenuated, Q-switched laser pulse were done with a calibrated "rat's nest" calorimeter. The waveform was recorded with a filtered photomultiplier and an oscilloscope.

In general there were five experiments performed on the aluminum plasma produced by impacting the Q-switched output of the twin ruby laser onto an aluminum target in vacuum. The first experiment was to investigate mass removal and target deformation as a result of a Q-

switched laser pulse interacting with a solid aluminum target. This experiment gave an approximate figure to the amount of energy given to the expanding plasma by the laser pulse. It was also noticed that the deformation left on the target surface was elliptical in shape. The next experiment was to investigate the aluminum plasma with electrical probes. The experimental results indicate that shortly after laser beam impact, a cloud of electrons are emitted from the impact area followed closely by a cloud of ions. The expansion velocity of the plasma front was calculated to be about  $1.6 \times 10^7$  cm/sec. Data from the probe experiment also indicated that the expanding plasma was not symmetrical. The third experiment undertaken was an attempt to obtain the vacuum ultraviolet spectra of the aluminum plasma. This experiment failed to produce the desired spectra. The fourth experiment was to measure the relative ultraviolet light emission from the plasma as a function of time. The experimental data indicated that maximum emission occurred approximately 250 nsec after laser beam impact and decayed to zero in very close to 2.5  $\mu$ sec. The last experiment, which was carried out in conjunction with the light emission experiment, was the plasma analysis using a quadrupole mass filter. The quadrupole mass filter was constructed by H. W. Willis to analyze the relative ionic species present in the laser induced plasma.

#### Suggestions for Future Improvements

This section can be divided into two parts. The first part which will be discussed is improvements which could be made to the existing equipment. In the second part, improvements in data collection will be discussed.



One of the improvements which should be made in the equipment is to design a pulse forming network for the capacitive discharge into the flashtube. This type of discharge circuit produces much more efficient energy conversion and much less acoustical shock to the flashtube. Another improvement needed to speed up data taking is the design and construction of a huskier power supply for charging the capacitor banks. Also, more energy could be obtained if the laser were operated in a true generator-amplifier mode as shown in Figure 97. And if the time and money existed, use of a pockel's cell for Q-switching. Another possible improvement is to use a photodiode or phototransistor to monitor the laser pulse waveform so that there is no uncertainty due to photomultiplier broadening of the output pulse as measured on the oscilloscope. This is especially important when using a pockel's cell for Q-switching because because of the relatively short pulse duration, i.e., 10 nsec.

As far as the experimental data taking is concerned, a possible improvement of the ultra-violet spectra of the plasma could be realized by using the Kodak Pathe SC.7 film. Also an extremely valuable experiment could be performed using ultra-violet detectors in place of film in the vacuum ultra-violet spectragraph. A good choice for the detector would be the Bendix Model 4219x Spiraltron or the Bendix Model 4010 Channeltron. These detectors have a spectral response from  $1500 \text{ \AA}$  to below  $2 \text{ \AA}$  and a gain of up to  $10^8$ . These detectors coupled with the new sampling oscilloscopes made by Tektronix and Hewlett-Packard, which give 2 mv/cm vertical sensitivity and .5 nsec/cm horizontal sweep, would enable the investigator to look at relative line intensities as a function of time. Although there are probably more improvement which could be made, it is felt that the above mentioned improvements will go a long

POCKEL'S CELL Q-SWITCH

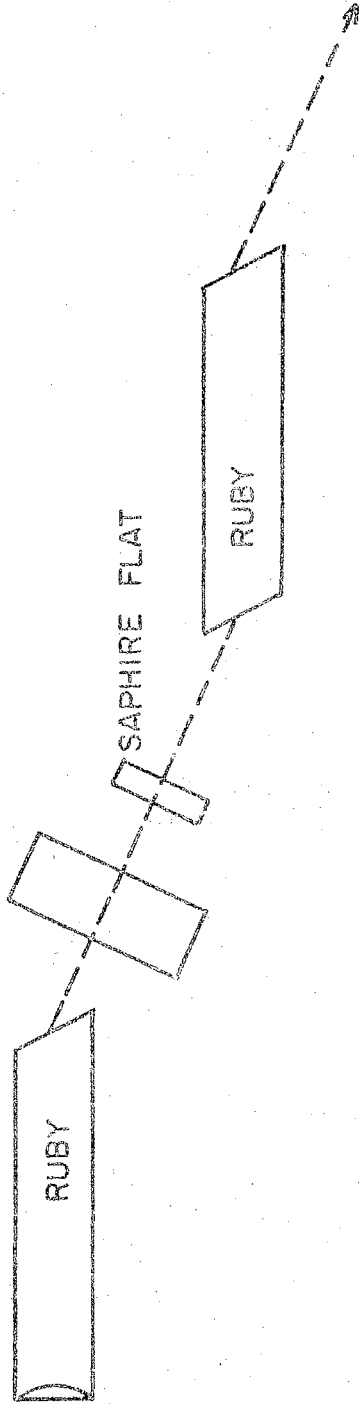


FIG.97 OSCILLATOR AMPLIFIER LASER SYSTEM

way toward producing better experimental results.

It must be kept in mind that we are entering a new era of plasma production, an era in which the laser will most certainly play an important part both in the experimental production of plasma for scientific analysis and possible as an economical method of producing controlled fusion.

#### SELECTED BIBLIOGRAPHY

- (1) Gordon, J. P., Zeiger, H. J., and Townner, C. H. "The Maser. New Type of Amplifier, Frequency Standard and Spectrometer." Physical Review, Vol. 99 (1955), p. 1264.
- (2) Maiman, T. H. "Stimulated Optical Radiation in Ruby." Nature, Vol. 187 (1960), p. 493.
- (3) Singer, J. R. Masers. New York: Wiley, 1959.
- (4) Abella, I. D. and Cummins, H. Z. "Thermal Tuning of Ruby Optical Maser." Journal of Applied Physics, Vol. 32 (1961), p. 1177.
- (5) Damon, E. K. "Theory and Technique of Giant Pulse Lasers." Microwaves, Vol. 7 (1964).
- (6) Mashkwich, U. S. Laser Kinetics. New York: American Elsevier, 1967.
- (7) Birnbaum, G. Optical Masers. New York: Academic Press, 1964.
- (8) Ehler, A. W. "Plasma Formed by a Laser Pulse on a Tungsten Target." Journal of Applied Physics, Vol. 37 (1966), pp. 4962-4966.
- (9) Ready, J. F. "Effects Due to Absorption of Laser Radiation." Journal of Applied Physics, Vol. 36, No. 2, (1965), pp. 462-468.
- (10) Gregg, D. W., and Thomas, S. J. "Plasma Temperatures Generated by Focused Laser Giant Pulses." Journal of Applied Physics, Vol. 38, No. 4, (1967), pp. 1729-1730.
- (11) Honig, R. E., and Woolston, J. R. "Laser Induced Emission of Electrons, Ions, and Neutral Atoms From Solid Surfaces." Applied Physics Letters, Vol. 2, No. 7, (1963), pp. 138-139.
- (12) Ehler, A. W. "Plasma Produced by a Laser Pulse Focused on a Metal Surface." (Hughes Research Laboratories, Research Report No. 336, May, 1965).
- (13) Ready, J. F. "Development of Plume of Material Vaporized by Giant Pulse Laser." Applied Physics Letters, Vol. 3, No. 1, (1963), pp. 11-13.

- (14) Basov, N. G., Boiko, V. A., Dementev, V. A., Krokhin, O. N., and Sklizkov, G. V. "Heating and Decay of Plasma Produced by a Giant Laser Pulse Focused on a Solid Target." Soviet Physics JETP, Vol. 24, No. 4, (1967), pp. 659-666.
- (15) Opower, H., and Burlefinger, E. "Temperature Determination of Plasmas Produced by Giant Laser Pulses." Physics Letters, Vol. 16, No. 1, (1965), pp. 37-38.
- (16) Namba, S., Kim, P. H., Itoh, T., and Arai, T. "Ion Emission From Metal Surface Irradiated by Giant Pulse Laser Beam." Laser Paris, (1967), pp. 113-116.
- (17) Hironv, M., and Iwamoto, I. "Density and Temperature of Laser-Produced Plasma in a Space Chamber." Japan Journal of Applied Physics, Vol. 6, (1967), p. 1006.
- (18) Linlor, W. I. "Ion Energies Produced by Laser Giant Pulse." Applied Physics Letters, Vol. 3, No. 11, (1963), pp. 210-211.
- (19) Ehler, A. W., and Weissler, G. L. "Vacuum Ultraviolet Radiation From Plasmas Formed by a Laser on Metal Surfaces." Applied Physics Letters, Vol. 8, No. 4, (1966), pp. 89-91.
- (20) Fawcett, B. C., Gabriel, A. H., Irons, F. E., Peacock, N. J., and Saunders, P. A. H. "Extreme Ultraviolet Spectra From Laser-Produced Plasmas." Proceedings of the Physical Society, Vol. 88, (1966), pp. 1051-1053.
- (21) Mott, N. F., and Jones, H. The Theory of the Properties of Metals and Alloys, Chapter III, New York: Dover, 1958.
- (22) Sproul, R. L. Modern Physics, A Text Book for Engineers, New York: Wiley, 1956.
- (23) Oliphant, M. L. E. "Action of Metastable Atoms of Helium on a Metal Surface." Royal Society Proceedings, Vol. 124 (1929), pp. 228-242.
- (24) Dorrestein, R. A. "Expulsion of Electrons From a Metal Surface by Ions and Metastable Atoms." Physics Review, Vol. 33 (1942), pp. 385-387.
- (25) Massey, H. S. W. "Theory of the Extraction of Electrons From Metals by Positive Ions and Metastable Atoms." Cambridge Phil. Society Proceedings, Vol. 26 (1930), pp. 386-401.
- (26) Cobas, A. and Lamb, W. E., Jr. "On the Extraction of Electrons From a Metal Surface by Ions and Metastables." Physics Review, Vol. 65 (1944), pp. 327-337.
- (27) Peery, L. J. "Design and Construction of a Twin Ruby Laser." (unpub. M.S. thesis, Oklahoma State University, 1967).

- (28) Levine, A. K. Lasers, Vol. 1, New York: Marcel Dekker, 1962.
- (29) Jenkins, F. A., and White, H. E. Fundamentals of Optics, New York: McGraw-Hill, 1957.
- (30) Baker, R. M. "Measuring Laser Output With Rat's Nest Calorimeter." Electronics, Vol. 36 (1963), pp. 36-38.
- (31) Schmidt, A. J., and Greenhow, R. C. "An Absolute Method for Measuring the Energy Output of a Laser." Journal of Scientific Instruments, Vol. 44, (1967), pp. 468-469.
- (32) Goldsmith, A., Waterman, T., and Hirschhorn, T. G. Handbook of Thermophysical Properties of Solid Materials, Vol. 1, New York: Macmillan, 1961.
- (33) Langmuir, I., and Mott-Smith, H. M. "Positive Ion Currents in the Positive Column of the Mercury Arc." General Electric Review, Vol. 26 (1923), p. 731.
- (34) Loeb, L. B. Fundamental Processes of Electrical Discharges in Gases, New York: Wiley, 1939.
- (35) Langmuir, I., and Blodgett, K. B. "Currents Limited by Space Charge Between Coaxial Cylinders." Physical Review, Vol. 22 (1923), p. 347.
- (36) Druyvesteyn, M. J. "Der Niedewoltbogen." Z. Physik, Vol. 64 (1930), p. 781.
- (37) Medicus, G. "Critical Survey of the Methods for Finding the Energy Spectrum of the Carriers in Plasmas by Means of Probers." (United States Air Force Office of Aerospace Research Report, Project No. 4152, 1969).
- (38) Peery, L. J. "A Model and Calculations for Laser Induced Plasmas." (unpub. Ph.D. thesis, Oklahoma State University, 1970).
- (39) Bruce, R. E. "A Model and Calculations for the Properties of an Exploding Plasma Sphere." (unpub. Ph.D. thesis, Oklahoma State University, 1966).
- (40) Brown, V. D. "Use of a Pulsed Photomultiplier to Measure the Light Intensity Verses Time for a Spark Discharge Between Aluminum Electrodes." (unpub. Ed.D. thesis, Oklahoma State University, 1968).
- (41) Willis, H. W. "Quadrupole Mass Filter Design and Construction for Plasma Ion Analysis." (unpub. M.S. thesis, Oklahoma State University, 1969).
- (42) Todd, F. C. (Private Communication, 1970).

- (43) Cobine, J. D. Gaseous Conductors, New York: McGraw-Hill, 1941.
- (44) Payne, R. D., and Todd, F. C. "A Spectrograph for the Far Ultraviolet." Proceedings of the Oklahoma Academy of Science, Vol. 46 (1966).
- (45) Carpenter, T. M. "Calibration of a Far Ultraviolet Spectrograph and a Study of Vacuum Spark Breakdown." (unpub. M.S. thesis, Oklahoma State University, 1970).

VITA

William Grant Robinson

Candidate for the Degree of  
Master of Science

Thesis: MODIFICATION AND DESIGN OF A TWIN RUBY, Q-SWITCHED LASER FOR  
PLASMA PRODUCTION

Major Field: Physics

Biographical:

Personal Data: Born in Oklahoma City, Oklahoma, February 12, 1943,  
the son of William T. and Mary L. Robinson.

Education: Attended grade school in Oklahoma City, Oklahoma;  
graduated from Midland High School, Midland, Texas, in 1961;  
received the Bachelor of Science degree from Central State  
College, Edmond, Oklahoma, with a major in Physics and  
Mathematics, in May, 1966; completed requirements for the  
Master of Science degree in July, 1970.

Professional Experience: Student trainee with Oklahoma Gas and  
Electric Co., in Oklahoma City, Oklahoma; Laboratory Assistant  
in Physics Department, Central State College; Teaching Assist-  
ant in Physics Department, Oklahoma State University; Research  
Assistant for Oklahoma State University Research Foundation;  
Research Assistant in Electrical Engineering Department, Okla-  
homa State University; Electronics Engineer with Air Force  
Logistics Command; Physicist with Air Force Cambridge Research  
Lab., Lunar Laser Observatory; Member of Sigma Pi Sigma.